Growth and diffusion on metal nanoparticles

Nicolò Canestrari

Supervisors: Prof. R. Ferrando, Dr. Diana Nelli

University of Genoa

Ph.D. in Physics and Nanosciences - curriculum Physics
XXXVIII Cycle

Table of contents

Introduction **1**

1 Geometric structures and chemical ordering of nanoparticles and nanoalloys **5**
1.1 Geometric structures 5
1.1.1 Crystalline structures 6
1.1.2 Noncrystalline structures: Icosahedra and Decahedra 8
1.2 Chemical ordering 15

2 Molecular Dynamics and computational tools **19**
2.1 Atomistic potentials 20
2.2 Molecular Dynamics 22
2.3 Minimization and quenching 25
2.4 Pressure analysis 26
2.5 DFT calculations 27
2.6 Global optimization 30

3 General theory for icosahedral shells **35**
3.1 Caspar-Klug method 36
3.2 Packing shells 42
3.3 Size mismatch rules 45

4 Growth simulations **51**
4.1 Nanoalloys 52
4.2 Growth simulations 52
4.2.1 Ag-Ni 52
4.2.2 Ag-Co 57
4.2.3 Ag-Cu 57
4.2.4 Au-Ni 61
4.2.5 Au-Co 61

4.2.6 Au-Fe 63
4.3 Heating simulations 65
4.4 Stability and pressure analysis 71
4.5 Conclusions 72

5 Diffusion and mobility on close-packed nanoparticles 81
5.1 Chiral smooth surface 82
5.2 Adsorption sites 84
5.3 Mass diffusion 86
5.4 Drag method estimates 88
5.5 Cu nanoparticles 94

Conclusions 97

References 101

Introduction

Nanoparticles (NPs) are aggregates of atoms. The number of atoms contained in a nanoparticle can vary from a few tens to a million, corresponding to diameters ranging from 1 to 100 nm [1, 2]. This put nanoparticles in the intermediate zone between microscopic and macroscopic physics, where statistical mechanics must account for huge fluctuations [3]. Bi- or multicomponent nanoparticles are also known as nanoalloys [4].

Metallic nanoparticles can be produced in different experimental settings and environments with different trade-offs, depending on the specific needs. When a low contamination is needed during production, synthesis in the gas phase is preferred. This kind of synthesis guarantees a high level of purity in the production of nanoparticles, where the high quality of the yield usually coexists with a generally low amount of output. Gas-phase synthesis is typically done under vacuum conditions in a few steps. First, in the vaporization stage, a solid metal target is heated or sputtered to produce a metallic vapour [5]. Then, during the nucleation stage, the vapour is cooled down by a inert gas flux (usually helium or argon) so that atoms can aggregate in small nuclei, since re-evaporation is now less favourable. Finally these metallic nuclei can grow by the addition of further atoms or small aggregates. In a later stage, large aggregates may also collide with each other and coalesce to form even larger units. This process can also be studied according to aerosol dynamics, to capture in particular the relevance of the cooling rate [6].

There are several types of sources for gas-phase growth. A well known example is the magnetron sputtering source, for which a schematic representation is given in Fig. I1. Inert gas ions (typically Ar^+) are accelerated and fired against the target material (for example a metal or a mixture of metals), which sputters single atoms and small aggregates. These products are then cooled down by an inert gas flow to start nucleation and growth; when aggregation is in process the nanoparticles are drifted away from the target by a pressure difference. Subsequently, a mass filter may select only certain nanoparticles; this can be done with a precision of usually about 10%. Finally these selected nanoparticles enter the deposition chamber, which is allowed to rotate to achieve a more homogeneous deposition on the substrate.

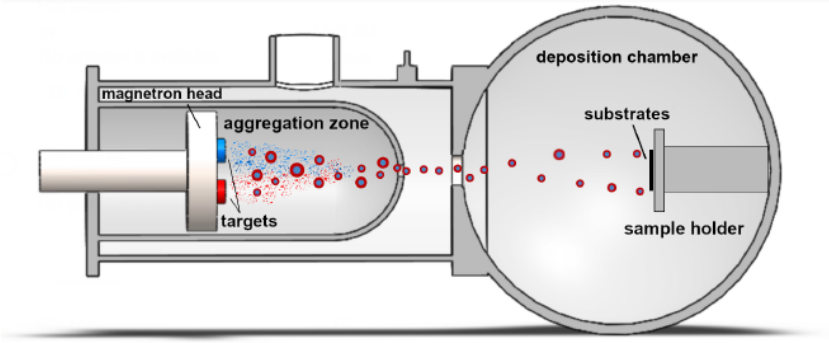

Fig. I1 Schematic representation of bimetallic nanoalloys synthesis by magnetron sputtering. Reprinted with permission from [7]. Copyright 2020 American Chemical Society.

On the other hand, when a more abundant production of nanoparticles is needed, synthesis in the liquid phase is preferred. In this case, metallic nanoparticles are in many cases let to aggregate in an aqueous solution. In liquid-phase synthesis, the price to pay for having a high yield is given by the possible contamination from the surrounding environment, which is at the same time very often necessary to protect the produced nanoparticles from massive agglomeration and coalescence.

Once produced, either in the gas or the liquid phase, the structural properties of nanoparticles must be characterized. Electron microscopy is the most widely used technique for this purpose. In particular, TEM (Transmission Electron Microscopy) and STEM (Scanning TEM) are used most frequently. Recently, also grazing incidence X-ray diffraction has been used to analyze growing nanoparticles on substrates [8]. A series of HAADF-STEM (High-Angle Annular Dark-Field Scanning Transmission Electron Microscope) images of some Ag nanoparticles is given in Fig. I2.

Nanoparticles exhibit physical and chemical properties that considerably differ from those of the bulk metals, with regard for instance to the chemical reactivity or the melting temperature [3]. For this reason, they are gaining increasing importance in a significant number of different scientific areas due to their many applications. These applications include for example catalysis, data storage, plasmonics, nanomedicine, water purification and many others. Consequently, nanoparticles have been extensively studied in recent years. Very often, the determination of the properties of nanoparticles has been possible thanks to a combined experimental-theoretical investigation (see for example Refs. [10–13]). Therefore, the theoretical and computational study of metal nanoparticles is of utter importance. In fact, laying the basis for the understanding of these nanoscale systems is a fundamental step towards the comprehension and interpretation of experimental observations as well as the design of new experiments.

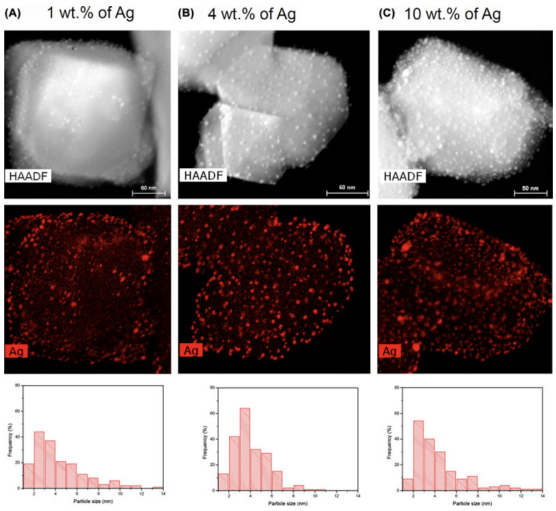

Fig. I2 HAADF-STEM images of Ag nanoparticles. The three images are of different experiments, with a different Ag content of the powder, see Ref. [9]. Scale bar in the figure. Copyright 2016 Royal Microscopical Society.

However, these finite nano-sized systems are very difficult to model by means of analytical techniques only, since the explicit solution of the quantum problem of a system of many atoms is a very difficult - if not impossible - task. As a consequence, considerable effort has been put in the development of numerical techniques aimed at overcoming this obstacle. These techniques - that may take into account either explicitly or implicitly the quantum nature of the system - allow us to study at atomic level both the structure and the growth and temporal evolution of metal nanoparticles, a very powerful feature that is at present quite limited in experimental techniques. It is therefore very much possible that a work of simulation can pave the way for the realization of a new class of nanoparticles not yet considered, and for a better understanding of their properties based on their shape.

This Ph.D. thesis is dedicated specifically to the development of a new design principle for icosahedral nanoparticles and, based on that, to the use of Molecular Dynamics (MD) simulations to study the growth and the properties of those aggregates. Other geometric shapes (octahedra and tetrahedra) are studied as well when it comes to surface diffusion.

In Chapter 1 we describe the geometrical and chemical features of nanoalloys and metal nanoparticles in general, with a special focus on icosahedra. In Chapter 2 we give the description of our computational methods, beginning with the features of MD simulations, which is the main algorithm we used, and the atomistic models we employed. The advantages and disadvantages of this approach are discussed, including the possibility to use this method to simulate a gas phase experiment. The theoretical approach used for the pressure analysis of nanoparticles is also discussed in this chapter.

Chapter 3, 4 and 5 contain the original results of this thesis. In Chapter 3, we develop a new theory for the design of multicomponent icosahedral nanoparticles [14]. This theory is based on concepts and results from different scientific areas: the work of Caspar and Klug on the geometry of viral capsids [15], and that of Mackay, who first described a strategy to assemble atoms into compact icosahedral clusters [16]. In the chapter, the Caspar-Klug and Mackay constructions are described; then, they are combined and generalized into our new design approach. The wide variety of new kinds of nanoparticles that can be built according to our strategy is described in the chapter. In addition, the correspondence between chiral icosahedral shells based on the Caspar-Klug construction and generalized anti-Mackay shells is demonstrated.

The various MD simulations that were performed to validate our design rules are then described in Chapter 4, with their settings and outcomes. Particular attention is devoted to chiral nanoparticles, and to their growth starting from an achiral seed. The transformation from the achiral anti-Mackay/pentakis icosahedral shell to the chiral arrangement is also discussed. Then an analysis of the pressure distribution within the nanoparticles is provided, along with a discussion of the stability of the chemical ordering.

In Chapter 5 the homogeneous surface diffusion is discussed, both on icosahedral nanoparticles - Mackay and chiral - and on tetrahedra and octahedra. These structures, that all have (111) surface facets but different edges, are compared, focusing of nanoparticles with Ag surface [17]. The particular properties of an edgeless surface as that of the chiral icosahedron are highlighted. The results of the growth simulations previously seen in Chapter 4 are discussed and rationalized based of these findings.

The thesis is then completed by the Conclusions, summing up the main results and outlining some possible developments.

Chapter 1

Geometric structures and chemical ordering of nanoparticles and nanoalloys

Nanoparticles can vary in both shape and, in case of a bi-metallic or multi-metallic composition, in *chemical ordering*, meaning the pattern by which elements are arranged. Both the shape and the chemical ordering determine the physical and chemical properties of the NP, and so are to be considered in order to select suitable aggregates for a given application. This can be seen for example in the case of optical properties [18–20], which strongly depends on the NP's shape. It is possible to produce nanoparticles with a desired shape or size, or to select them from the production site, with today technologies. In this chapter we will give an overview of the most common geometrical forms and chemical orderings that are found in metal nanoparticles, and then focus specifically on the various different icosahedral shapes. A more comprehensive discussion of these different structures and patterns can be found in Refs. [3, 4, 21], where the energetic implications of these arrangements are also highlighted.

1.1 Geometric structures

All geometric structures of nanoalloys can be classified as being either *crystalline* or *non-crystalline* structures. The *crystalline* class includes structures that can be thought of as fragments of an infinite crystal lattice (the bulk crystal), which could be face-centered cubic (fcc), body-centered cubic (bcc) or hexagonal close-packed (hcp). As a consequence of that, these nanoparticles have an interatomic distance similar to that observed in the bulk crystal. The *noncrystalline* class includes structures that cannot be derived as fragments of any crystal lattice. The most simple case is that of twinned structures, obtained by merging together two fcc structures with a shared atomic plane; the most interesting case however is that of

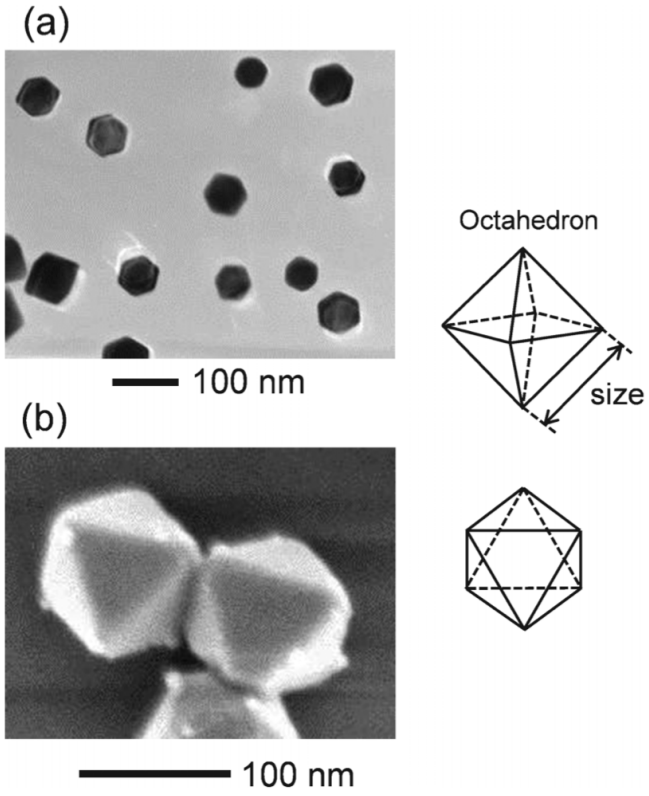

Fig. 1.1 (a) Au octahedral nanoparticles: SEM image. (b) Au octahedral nanoparticles: TEM image. Reproduced from [22] Copyright The Royal Society of Chemistry 2012.

decahedra and icosahedra, where the lack of translational invariance can be associated with the presence of a fivefold symmetry axis.

1.1.1 Crystalline structures

From energetic considerations [3] we see that it would be a good way of cutting the infinite crystal to leave exposed the surfaces with the densest packing of atoms. In the fcc lattice this gives the best possible result: we can have close-packed surfaces (111) with both octahedral and tetrahedral shapes. On the other hand neither the bcc nor the hcp lattices permits such a result and we must accept as the best structure, in term of low surface energy, the rhombic dodecahedron (or the cube) or a bipyramid respectively. We will consider, for the purpose of diffusion on close-packed surfaces, both the tetrahedron and the octahedron. Nanoparticles showing these structures were obtained in several growth experiments. One example in given in Fig. 1.1.

The regular tetrahedron (Th) has four facets that are equilateral triangles, six edges and four vertices. Let n be the number of atoms in each edge; the tetrahedron can be constructed

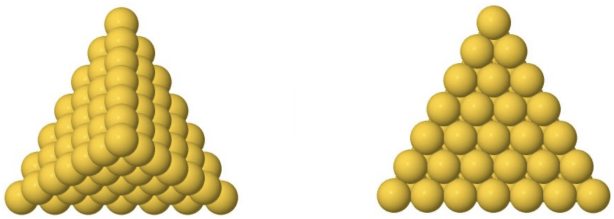

Fig. 1.2 Top and side view of a regular tetrahedron with $n = 7$.

by stacking equilateral triangles of decreasing edge length from the base to the vertex. Then, the total number of atoms N_{Th} in the regular tetrahedron can be computed to be:

$$N_{\mathrm{Th}} = \frac{1}{6} n(n+1)(n+2), \tag{1.1}$$

which gives the series of numbers: $N_{\mathrm{Th}} = 1, 4, 10, 20, 35, 56, \ldots$ for $n = 1, 2, 3, 4, 5, 6, \ldots$ and so on.

The regular octahedron (Oh) has 8 facets that are equilateral triangles, twelve edges and six vertices. It can be thought as two regular pyramids joined together, sharing a common square base. Hence, the number of atoms of a regular octahedron N_{Oh}, having n atoms in each edge is

$$N_{\mathrm{Oh}} = \frac{1}{3}(2n^3 + n), \tag{1.2}$$

which gives the series of numbers: $N_{\mathrm{Oh}} = 1, 6, 19, 44, 55, \ldots$ for $n = 1, 2, 3, 4, 5, \ldots$ and so on. An image of a regular tetrahedron is shown in two views in Fig. 1.2. It is of course also possible to study tetrahedra with the vertices removed. Due to the low coordination number, meaning the number of nearby atoms, this is a situation that can easily occur under normal conditions.

While regular octahedra and tetrahedra are indeed optimal in term of low surface energy, they do have a quite large surface-to-volume ratio, which is an unfavorable feature in term of energy, with a wide surface leading to an additional energetic contribution (surface tension). In the case of an octahedron, if a truncation is made at the vertices of the nanoparticle, it is possible to lower the surface-to-volume ration while accepting to have some (100) facet. From the Wulff construction it is possible to show that there is an optimal way of cutting an octahedron [21] by following the rule:

$$\frac{\gamma_{100}}{\gamma_{111}} = \frac{d_{100}}{d_{111}} \tag{1.3}$$

where the first term account for the surface energies and the second term for the distances from the center. A truncated octahedron is then built by making truncations all over the six vertices. Such truncations create six (100) square facets, which is the energetic cost that is compensated by the lowering of the surface-to-volume ration. The depth of the best truncation is usually the one for which the remaining (111) facets become regular hexagons. Let n_{cut} be the number of layers cutted at each vertex. The number of atoms of the truncated octahedron (TO) is therefore

$$N_{\mathrm{TO}} = \frac{1}{3}(2n^3+n) - 2n_{cut}^3 - 3n_{cut}^2 - n_{cut}. \tag{1.4}$$

Regular truncated octahedron is obtained when $n_{cut} = (n-1)/3$. In this case, the number of atoms is:

$$N_{\mathrm{TO}}^{\mathrm{reg}} = \frac{1}{27}(16n^3 - 3n^2 + 12n + 2), \tag{1.5}$$

which gives the series of numbers: $N_{\mathrm{TO}}^{\mathrm{reg}} = 38, 201, 586, 1289, \ldots$ for $n = 4, 7, 10, 13, \ldots$ and so on.

If we put instead $n_{cut} = (n-1)/2$, what we have is a cuboctahedron (COh) meaning:

$$N_{\mathrm{COh}} = \frac{1}{12}(5n^3 + 7n), \tag{1.6}$$

which gives $N_{COh} = 1, 13, 55, 147, 309, \ldots$ for $n = 1, 3, 5, 7, 9, \ldots$ and so on. In a regular truncated octahedron the close-packed facets are hexagons, while in a cuboctahedron they are triangular. The remaining facets are all (100), and in the cuboctahedron they total to a greater surface than that of the close-packed ones. Some octahedra, regular truncated octahedra and cuboctahedra are shown in Fig. 1.3 from two different views.

1.1.2 Noncrystalline structures: Icosahedra and Decahedra

Noncrystalline structures can be of a great variety with shapes, depending usually on how different fcc subunits are joined together with some common atomic planes between them. The number of these subunits can vary from a minimum of two to much more (see *multiply twinned* nanoparticles 1.4). Usually the common atomic planes are also local mirror planes, giving some symmetry to the structure. The Decahedron (Dh) and Icosahedron (Ih) are non-crystalline structures which consist of respectively five and twenty tetrahedral subunits joined together; one could also form poly-icosahedral nanoparticles with elementary icosahedra of 13 atoms, formed in turn by joining elementary tetrahedra of 4 atoms. These structures have distortions and non-ideal interatomic distances precisely due to the interstices that

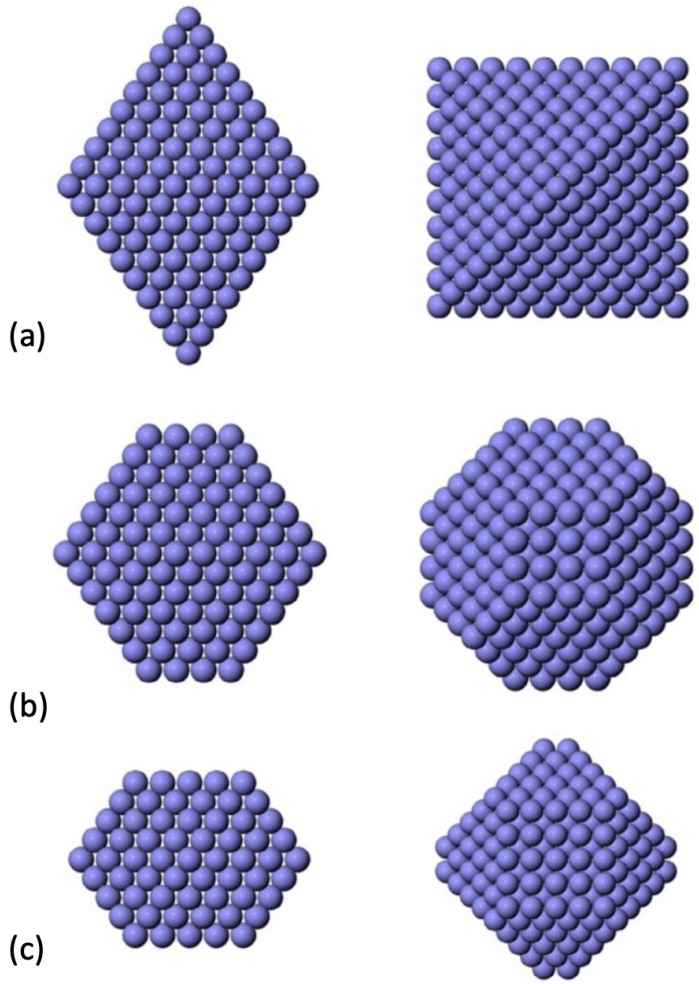

Fig. 1.3 (a) An octahedron of 670 atoms: $n = 10$. (b) A regular truncated octahedron of 586 atoms: $n = 10$ and $n_{cut} = 3$. (c) A cuboctahedron of 309 atoms: $n = 9$ and $n_{cut} = 4$. Reproduced from [3] Copyright Elsevier 2016.

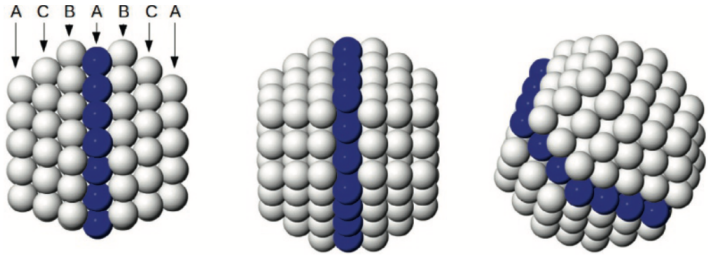

Fig. 1.4 Different views of the same twinned fcc nanoparticle of 201 atoms. Reproduced from [3] Copyright Elsevier 2016.

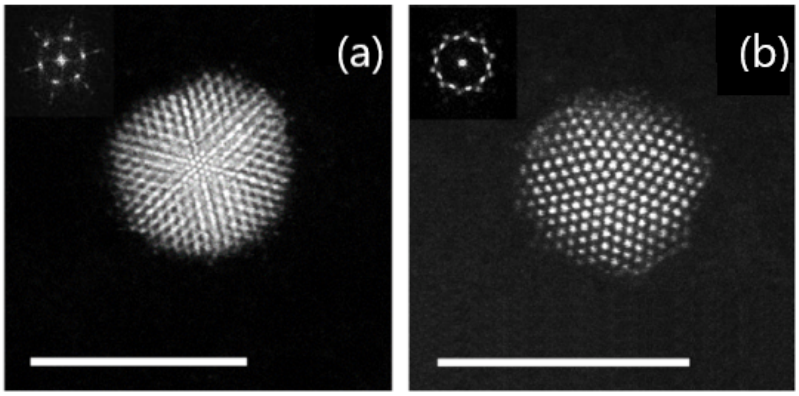

Fig. 1.5 HAADF-STEM images of AuPd noncrystalline nanoparticles. (a) Icosahedron and (b) decahedron. Scale bar 5 nm. Adapted with permission from [26]. Copyright 2021 American Chemical Society.

would remain if one took the tetrahedra and simply join them. Also as a consequence of the noncrystalline nature of this kind of nanoparticle there is a relevant strain, both on the surface of the structure and near the center. Nonetheless these are often found in experiments consistently with them being good from an energetic point of view (see [23–25]).

An example of AuPd nanoparticles observed by High-Angle Annular Dark-Field Scanning Transmission Electron Microscope (HAADF-STEM) is shown in Fig. 1.5.

Decahedra are composed by ten tetrahedra joined together to form two pentagonal pyramids, as one can see in Fig. 1.6 (a), (b), (c). In all the different form of decahedra there is a fivefold symmetry axis which is the edge shared by the five tetrahedral subunits in both pyramids. In the case of regular decahedra (Fig. 1.6 (a)) these two pyramids share their base. These structures share the common trade-off between the advantages of (111) facets, as are all the ten facets of the regular decahedron, and the large surface-to-volume ratio, as in the case of octahedra. In this case also the possible modification are changes at the edges or at the

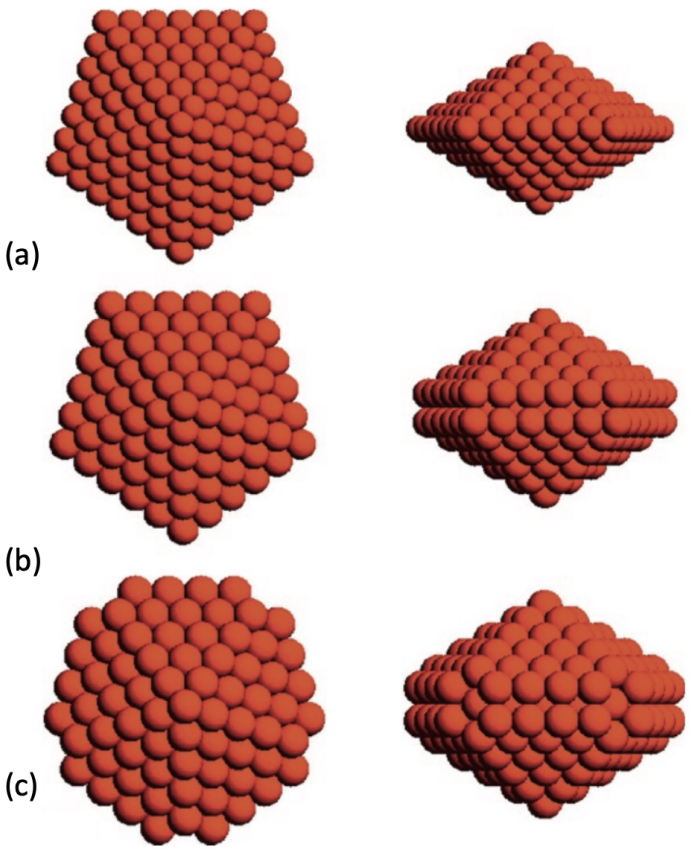

Fig. 1.6 Different types of decahedral structures in two different views. (a) Regular decahedron with $(m,n,p) = (7,1,1)$ containing 287 atoms, (b) Ino decahedron with $(m,n,p) = (6,2,1)$ containing 257 atoms, i.e. by removing 30 atoms of the perimeter of the base from the structure in (a) and (c) Marks decahedron with $(m,n,p) = (4,2,2)$ containing 247 atoms, i.e. by removing 10 atoms more from the structure in (b) to create re-entrances. Reproduced from [3] Copyright Elsevier 2016.

vertices of the structure. If the common base of the two pentagonal pyramids is eliminated then we have the Ino decahedron (see Refs.[27]), which is stabilized by the five resulting (100) facets, in that it is made more spherical (see Fig. 1.6 (b)). Finally, it is possible to make some reconstruction at the vertices, removing atoms from the (100) facets in order to create re-entraces: the resulting structure is the Marks decahedron [28] (see Fig. 1.6 (c)).

A Marks decahedron can be identified by three integers (m,n,p), where m and n are the number of atoms of the (100) facets, perpendicular and parallel to the fivefold axis, respectively; p is the depth of the re-entrance, where $p = 1$ means no re-entrance, i.e. a regular or Ino decahedron. The number of atoms of a Marks decahedron described by

(m,n,p) is:

$$\begin{aligned} N_{\text{Marks}} = & \frac{1}{6}(30p^3 - 135p^2 + 207 - 102) + \\ & + \frac{1}{6}\{5m^3 + (30p-45)m^2 + [60(p^2-3p)+136]m\} + \\ & + \frac{1}{6}\{n[15m^2 + (60p-75)m + 3(10p^2-30p)+66]\} - 1. \end{aligned} \tag{1.7}$$

The number of atoms for any Ino decahedron can be recovered simply putting $p = 1$. In that case:

$$N_{\text{Ino}} = \frac{1}{6}[5m^3 - 15m^2 + 16m + n(15m^2 - 15m + 6)] - 1. \tag{1.8}$$

Finally, the number of atoms of a regular decahedron is obtained when $n = 1$, that is when there are no (100) facets:

$$N_{\text{Dh}} = \frac{1}{6}(5m^3 + m). \tag{1.9}$$

The icosahedron is a platonic solid, just like the tetrahedron and the octahedron, and it has twenty facets, thirty edges and twelve vertices. It is already a quite spherical structure and that gives it an advantage in term of stability. The importance of this structure is highlighted by the numerous finding of it in nature: for instance it is the typical form of viral capsids [15]. The regular icosahedron (or Mackay icosahedron [16]) can be thought of as the result of joining together twenty tetrahedral subunits, one for each facet of the icosahedron, with the facets of the tetrahedron becoming a common plane two by two, and all the twenty vertices becoming one at the center. This leads to twelve vertices laying each pair on a fivefold symmetry axis. All facets are (111). A regular icosahedron is composed of concentric atomic shells. If the number of layers is k, the number of atoms of the relative icosahedral structure is given by

$$N = \frac{1}{3}(10k^3 - 15k^2 + 11k - 3), \tag{1.10}$$

which gives the series of numbers 1, 13, 55, 147, 309, ... for $k = 1,2,3,4,5,...$ and so on. An example of an icosahedral structure is shown in Fig. 1.7.

There are in literature [29, 30] some variations on this structure, mainly concerning bi-metallic systems, and with a recent generalization [14] that will be the object of **??**. The most simple such modification is that of having the atoms in the last layers to occupy the hcp sites on the underlying layer, meaning the number of surface atoms will be diminished by $20(k-2)$: this is known as the anti-Mackay icosahedron and is shown in Fig. 1.8 (b). It is then possible to distort this layer giving to it a chiral orientation as in Fig. 1.8 (c), obtaining a chiral icosahedron. It is also possible, given an anti-Mackay icosahedron, to remove all twelve vertices and obtain a pentadodecahedral cluster as in Fig. 1.9.

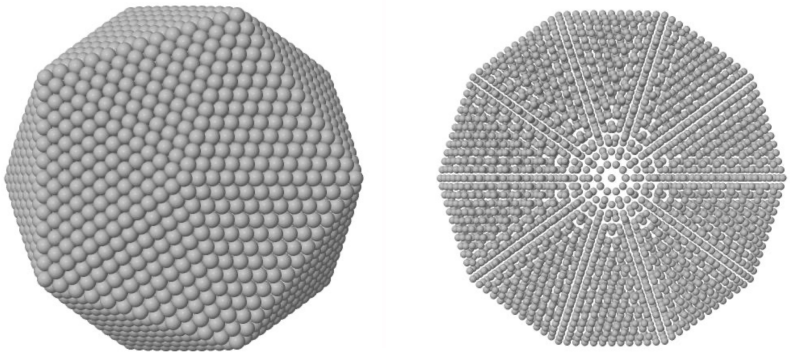

Fig. 1.7 Mackay Icosahedron with $k = 13$ atomic layers and 6525 atoms.

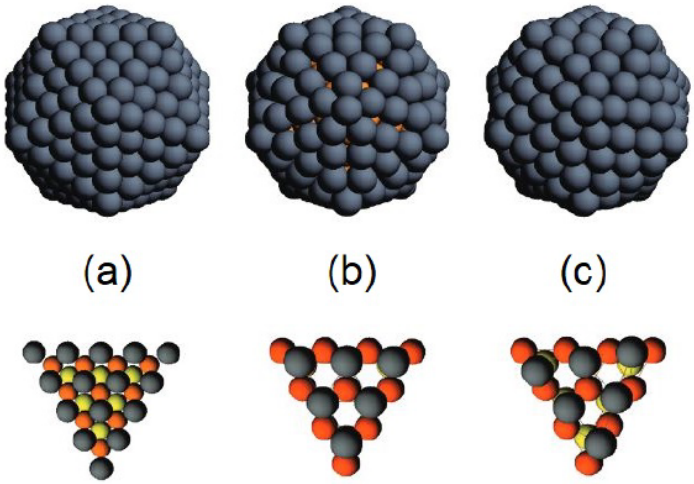

Fig. 1.8 (a) Mackay (b) anti-Mackay and (c) chiral icosahedra. For each structure, the surface (top row) and the stacking of the three outer surface layers (bottom row) are shown. Reprinted with permission from [30]. Copyright 2010 American Chemical Society.

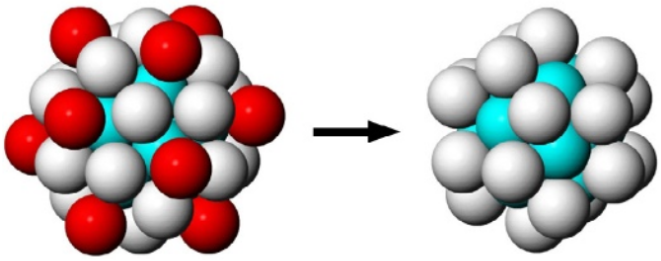

Fig. 1.9 Pentadodecahedral cluster obtained by removing all the vertices (red in figure) from an anti-Mackay icosahedron. The dodecahedron is also a platonic solid and is dual with the icosahedron. Adapted from [3] Copyright Elsevier 2016.

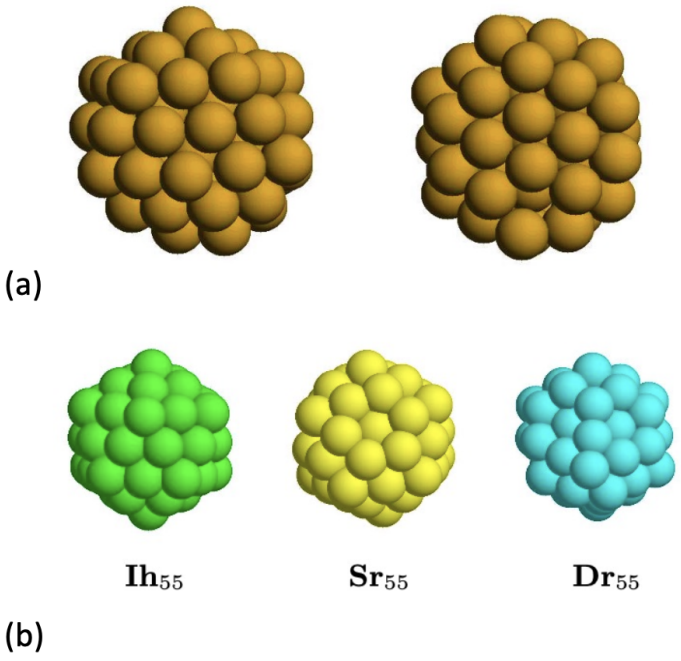

Fig. 1.10 Rosette reconstruction on the surface of icosahedral structures: (a) two isomers from an Au_{55} nanoparticle, (b) three isomers of Pt_{55} with zero, one or two rosettes. Adapted from [21]. Copyright 2005 The American Physical Society.

In anti-Mackay and chiral icosahedra, surface atoms are less-densely packed than in Mackay icosahedron. Therefore, these structures are typically less favorable than the regular ones, with the exeption of specific bi-metallic systems [30] satisfying certain rules [14]. Nevertheless, some surface reconstruction of the Mackay icosahedron that are favorable do exist. A notable example is that of *rosettes* [21, 31]. In this reconstruction pattern, a vertex atom enters the cluster surface and forms a hexagonal ring together with its former five surface neighbours. Multiple rosette reconstructions may be present, as shown in Fig. 1.10. It was found that for some Au and Pt nanoparticles, this kind of reconstruction is energetically favorable [21, 31]: in our work of simulation we often found these in Au nanoparticles. Sometimes multiple rosettes can also imply a reconstruction of atoms on the edges as in Fig. 1.11.

The usual way that the energetic cost of having a certain geometric structure is plotted, is by calculating the excess energy according to:

$$\Delta(N) = \frac{E(N) - N\varepsilon}{N^{2/3}}. \tag{1.11}$$

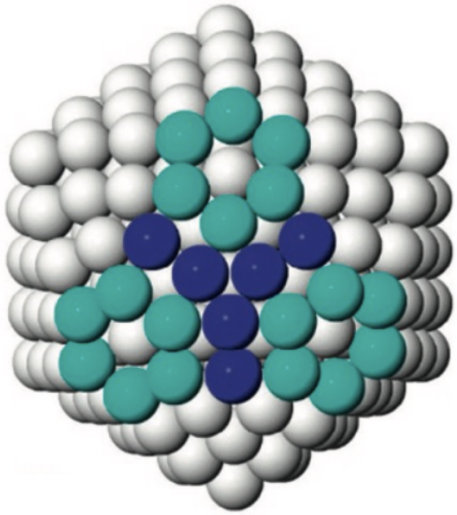

Fig. 1.11 Three rosettes on a Mackay icosahedron in cyan and reconstructed atoms on the edge in dark blue. Adapted from [3] Copyright Elsevier 2016.

where ε is the binding energy in the bulk crystal and E(N) is the binding energy of the structure for a given number of atoms. The denominator $N^{2/3}$ accounts for the rough number of surface atoms. As one an see in Fig. 1.12 this makes the icosahedron a very good shape energetically for a limited number of atoms (meaning up to more than a thousand); however, due to the possibility of having decahedra different than the Ino decahedron, a transition Ih->Dh can occur also at $N = 200,300$ atoms for Ag nanoparticles [3]. Once such a structure is formed it becomes possible, at least in simulations, to grow even more on top of it, meaning that even larger icosahedra such as that in Fig. 1.7 can be obtained.

1.2 Chemical ordering

Whenever a nanoalloy is considered, the atoms of different species will have a pattern by which they are distributed in the structure, meaning a specific chemical ordering. If there is phase separation, or the atoms of different elements do not mix, then that means such pattern is of the *nonmixing* kind, which is the most common class of chemical orderings, while a *mixing* pattern occurs when the tendency to intermix for entropic reasons prevails. Some example of nanoalloys that give rise to *nonmixing* patterns include AgCu, AgNi, AuCo, AgCo and AuPt, while *mixing* patterns are observed in CoPt, FePt, AuCu, AuPd, AgPd and

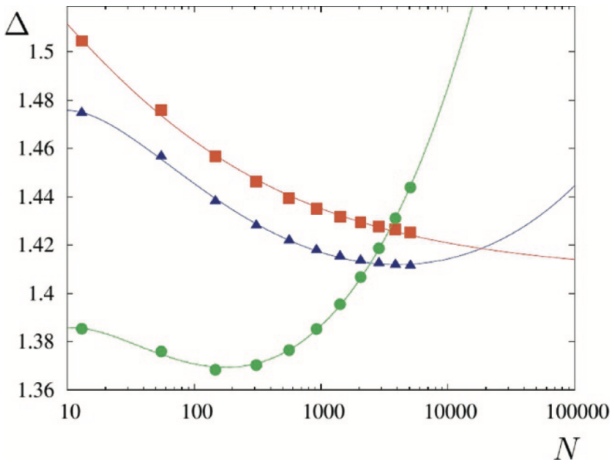

Fig. 1.12 The excess energy is plotted as a function of the nanoparticle size for icosahedra (green circles) cuboctahedra (red squares) and Ino decahedra (blue triangles). Adapted from [3] Copyright Elsevier 2016.

AgAu, among other systems that also mix in the bulk solution. It is clear anyway that greater similarity in atomic radius, cohesion energy and other properties in general will likely lead to a *mixing* arrangement. Sometimes a partial *mixing* pattern is observed, as in the case of AgPd [32], where the tendency to mix coexist with the tendency for Ag to migrate on the surface, due to lower cohesion energy. In mixed patterns, the two or more different chemical species occupy alternate positions. In a random mixing pattern, as shown in Fig. 1.13 (c), atoms form a solid solution. Non-random mixing patterns also occur: some examples, typical of bulk ordered phases, are shown in Fig. 1.13 (a) and (b), for 1:1 and 1:3 compositions, respectively. In these patterns, atoms of different chemical species are arranged in alternate planes. Also different than a random mixing pattern is the A1 phase, where all atomic planes have the same average composition.

In nonmixing patterns, the two or more metals segregate in different parts inside the nanoparticle. This is the most well-suited pattern for non-crystalline nanoparticles, where the inter-atomic distances are already distorted, though there are exceptions such as the frustrated $L1_0$ phase in decahedra [3]. Several examples are displayed in Fig. 1.14. The most common is the *core-shell* arrangement, shown in Fig. 1.14 (a), in which the core of the nanoparticles is entirely made of atoms of type A and the outer shell of the nanoparticles is entirely made of atoms of type B. For NPs displaying such chemical ordering, the notation A@B is often used. For such arrangements, the atomic species that segregate in the shell is naturally going to be that with the lower cohesion energy, while a larger atomic radius is also important, as we have seen particularly in the case of icosahedra [14]. Multi-shell arrangements are also

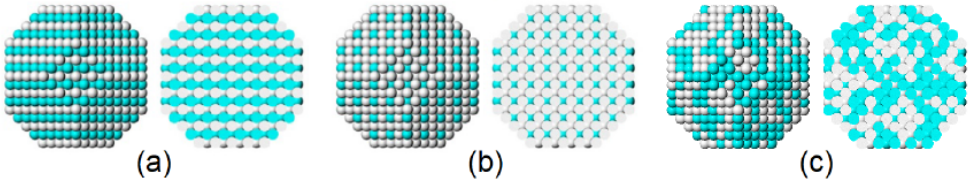

Fig. 1.13 Mixing patterns in crystalline bimetallic nanoparticles. Two different colours (grey and cyan) are used to highlight atoms of the two different species. In all cases both the nanoparticle surface (left) and a cross-section (right) are shown. (a) $L1_0$ phase at 1:1 composition, with alternating (100) atomic planes of the two elements: this implies a distortion of the unit cell in one dimension (tetragonalization). (b) $L1_2$ phase at 3:1 composition; the two alternating (100) atomic planes are made either of the most common atomic species or of the two species combined. (c) Randomly intermixed chemical ordering at 1:1 composition. Adapted from [3]. Copyright Elsevier 2016.

possible, such as the three-shell A@B@A arrangement, shown in Fig. 1.14 (b). Core-shell arrangements can also be asymmetric or incomplete, as in Fig. 1.14 (c). In Janus NPs, Fig. 1.14 (d) the two elements are simply separated in opposite sides; in quasi-Janus arrangements, a similar arrangements occurs, with the only difference that the surface layer is entirely made of one of the two elements, as depicted in Fig. 1.14 (e).

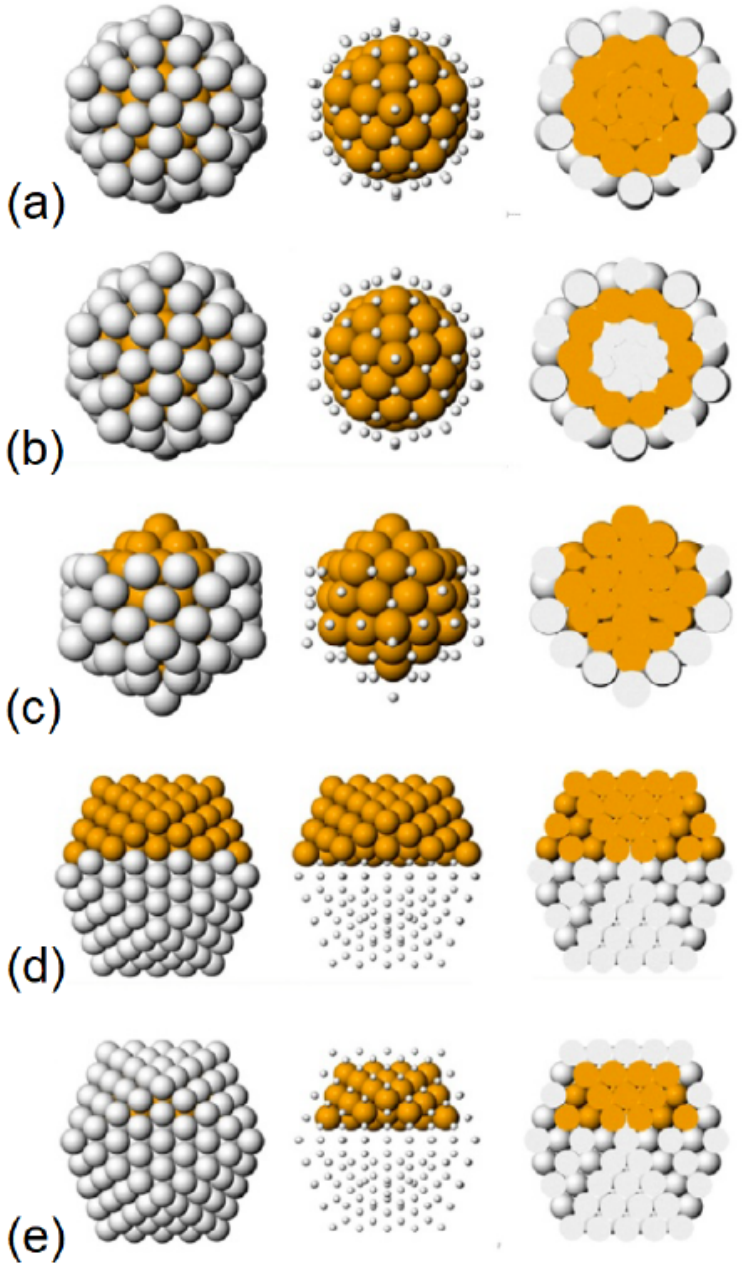

Fig. 1.14 Nonmixing patterns in bimetallic nanoparticles with icosahedral geometric structure. A and B atoms are shown in orange and grey, respectively. In all cases the nanoparticle is shown in three different views. Left column: nanoparticle surface. Middle column: B atoms are shown as small spheres. Right column: cross-section of the nanoparticle. (a) Core-shell A@B; (b) three-shell A@B@A; (c) core-shell A@B with incomplete B shell; (d) Janus; (e) quasi-Janus with B surface layer. Reproduced from [3]. Copyright Elsevier 2016.

Chapter 2

Molecular Dynamics and computational tools

The processes of growth and diffusion on metal NPs are often beyond what is accessible with today experimental setups to study adequately, and in any case it is necessary to have an idea of what to search for with a good theoretical basis. Moreover the very high complexity of the physics involved, even for small clusters of atoms, means that numerical methods have to be employed. Today this is a consolidated reality in the theoretical and experimental communities that research NPs and their chemical and physical properties.

While there are computational methods that allow to study metal NPs *ab initio*, that is by describing directly the interactions between electrons and nuclei, such as Density Functional Theory (DFT), in the present thesis we will only describe atomistic calculations. This means an atomistic potential will be taken to describe the interactions between metal atoms, of one or more species, that also reproduces correctly the known properties of the bulk material [33]. These potentials may also be found making use of DFT calculations in some cases. We will consider mostly Second Moment Approximation to Tight Binding (SMATB) potentials of the Gupta family, that are described in section 2.1.

When a cluster of atoms, a metal NP in particular, is considered, each atom brings with itself three space coordinates and three velocities. Even assuming the velocities as thermalized, this leaves a very complex problem: that of exploring all possible configurations and their energy, as well as their stability. A simple Lennard-Jones cluster of 100 atoms already has more than 10^{40} different local minima [34]. One possible approach is that of Monte Carlo algorithms, that is generating a variety of configurations with various modifications (moves) and then choosing each time the minimum in energy with a random probability given by a chosen temperature [3, 34, 35]. Another approach entirely consists in sampling the phase space in a way that closely resembles physical trajectories that could

happen in reality: this is the basic idea of Molecular Dynamics (MD) simulations [36], which in this thesis will refer to classical MD simulations only, given the use of atomistic potentials. This is described in section 2.2.

We also made use of local minimization programs, including quenching algorithms in particular, that will be explained in section 2.3. Finally, our algorithm for pressure analysis is described in section 2.4: we used it for some stability considerations. We complete the chapter with section 2.5, on DFT calculations which also were used in one of the two publications presented here [14]. Some remarks are also given on global minimization techniques in section 2.6.

2.1 Atomistic potentials

In Gupta potential, the potential energy of a nanoparticle $U(\{\mathbf{R}\})$ is given as a sum of single atomic contribution E_i, each depending on the inter-atomic distances $r_{ij} = |\mathbf{R}_i - \mathbf{R}_j|$:

$$U(\{\mathbf{R}\}) = \sum_{i=1}^{N} E_i, \tag{2.1}$$

where

$$E_i = \sum_{j, r_{ij} \leq r^c_{\alpha\beta}} A_{\alpha\beta} \exp\left[-p_{\alpha\beta}\left(\frac{r_{ij}}{r^0_{\alpha\beta}} - 1\right)\right] - \sqrt{\sum_{j, r_{ij} \leq r^c_{\alpha\beta}} \xi^2_{\alpha\beta} \exp\left[-2q_{\alpha\beta}\left(\frac{r_{ij}}{r^0_{\alpha\beta}} - 1\right)\right]}. \tag{2.2}$$

The repulsive term is given by a Born-Mayer formula applied to the ion-ion interactions in the cluster, while the attractive term is written as a many-body contribution to the energy. A cutoff distance $r^c_{\alpha\beta}$ determines in both cases whether first, second or even third neighbours will be taken into account. In this formula, α and β indicate the chemical species of atoms i and j while $r^0_{\alpha\beta}$ is taken as the equilibrium distance in the bulk crystal or as the average of the two equilibrium distances. The parameters $p_{\alpha\beta}, q_{\alpha\beta}, A_{\alpha\beta}$ and $\xi_{\alpha\beta}$ are fitted on some physical properties of the bulk metals and alloys [37–40]. In order to solve some problems with the discontinuity of energy there is a second cutoff distance $r^e_{\alpha\beta}$. The continuity of the potential energy is imposed through a fifth-order polynomial that links it smoothly to zero from $r^c_{\alpha\beta}$ to $r^e_{\alpha\beta}$. The form of the polynomial is $p(r) = a_{3,\alpha\beta}(r - r^e_{\alpha\beta})^3 + a_{4,\alpha\beta}(r - r^e_{\alpha\beta})^4 + a_{5,\alpha\beta}(r - r^e_{\alpha\beta})^5$, where $a_{3,\alpha\beta}, a_{4,\alpha\beta}$ and $a_{5,\alpha\beta}$ are coefficients needed to match the potential energy function and its first and second derivatives in $r = r^c_{\alpha\beta}$.

Forces acting on each atom can be calculated as the gradient of the Gupta potential energy. By taking into consideration the polynomial link, the derivation gives the following result,

for the force acting on the k-th atom:

$$\mathbf{F}_k = \sum_{i, r_{ik} \leq r^c_{\alpha\beta}} \mathbf{F}^{pot}_{ki} + \sum_{i, r^c_{\alpha\beta} < r_{ik} \leq r^e_{\alpha\beta}} \mathbf{F}^{pol}_{ki}, \tag{2.3}$$

where $\mathbf{F}^{pot}_{ki}$ is the the part of the force acting on the k-th atom due to the i-th atom, coming from the derivation of the Gupta potential, as given in eq. (2.2), and $\mathbf{F}^{pot}_{ki}$ the term derived from the polynomial link. The first term reads:

$$\begin{aligned} \mathbf{F}^{pot}_{ki} = \Bigg(& (D_k + D_i) q_{\alpha\beta} \xi_{\alpha\beta} \exp\left[-q_{\alpha\beta} \left(\frac{r_{ik}}{r^0_{\alpha\beta}} - 1 \right) \right] + \\ & - 2 p_{\alpha\beta} A_{\alpha\beta} \exp\left[-p_{\alpha\beta} \left(\frac{r_{ik}}{r^0_{\alpha\beta}} - 1 \right) \right] \Bigg) \frac{1}{r^0_{\alpha\beta}} \frac{\mathbf{r}_{ik}}{r_{ik}}, \end{aligned} \tag{2.4}$$

where

$$D_i = \frac{1}{\sqrt{\sum_{j, r_{ij} \leq r^c_{\alpha\beta}} \xi^2_{\alpha\beta} \exp\left[-2 q_{\alpha\beta} \left(\frac{r_{ij}}{r^0_{\alpha\beta}} - 1 \right) \right]}}. \tag{2.5}$$

The second one is:

$$\begin{aligned} \mathbf{F}^{pol}_{ki} = - \Bigg[& (D_k + D_i)(a_{3,\alpha\beta} dr^3 + a_{4,\alpha\beta} dr^4 + a_{5,\alpha\beta} dr^5)(3a_{3,\alpha\beta} dr^2 + 4a_{4,\alpha\beta} dr^3 + 5a_{5,\alpha\beta} dr^4) + \\ & - 2(3a_{3,\alpha\beta} dr^2 + 4a_{4,\alpha\beta} dr^3 + 5a_{5,\alpha\beta} dr^4) \Bigg] \frac{\mathbf{r}_{ik}}{r_{ik}}, \end{aligned} \tag{2.6}$$

where $dr = r_{ik} - r^e_{\alpha\beta}$.

In the past years the SMATB potential has been used successfully for transition and noble metals [41, 42]. Its accuracy has been verified by comparing its results with experimental data as well as DFT calculations. The SMATB potentials we employed have been already used in a variety of studies [41–43], including also alkali metals [44], beyond the case of transition and noble metals.

In one of our publications [14], we also employed Lennard-Jones and Morse potentials, which have for each pair of atoms the form:

$$u(r) = \varepsilon [\frac{r_m}{r}^{12} - 2 \frac{r_m}{r}^{6}] \tag{2.7}$$

for the LJ potential, and:

$$u(r) = \varepsilon[e^{-2\alpha(\frac{r}{r_m}-1)} - 2e^{-\alpha(\frac{r}{r_m}-1)}] \tag{2.8}$$

for the Morse potential. It can be shown that for $\alpha = 6$ the two potentials have the same width of well, while for $\alpha < 6$ the Morse potential is wider, meaning it has a smoother increase near the point of minimum energy. In the end for both the Morse and LJ potential one has:

$$U = \frac{1}{2}\sum_{ij} u(r_{ij}) \tag{2.9}$$

for the total energy.

2.2 Molecular Dynamics

The advent of electronic computers has led almost immediately to the development of numerical techniques to solve a variety of physics problems, among which the evolution of a system of few atoms as in Molecular Dynamics [45]. The task of a MD simulations is to solve numerically the Newton's equations, with time being discretized in small time steps: we will take 5 femtoseconds for our simulations. This is much lower than the time for an oscillation of the metal atom around its equilibrium position in the crystal bulk: such vibration happen on a time scale of some picosecond, around three orders of magnitude larger than our time step. This gives us very good numerical accuracy but also limits us to some microseconds as a total time of our simulations. As one can see in Fig. 2.1 the program consists in the iteration of an algorithm that gives the evolution from t to $t + \delta t$.

Initially, it is necessary to assign to each atom its velocity, which is done by following the Maxwell distribution:

$$p(v_x, v_y, v_z)dv_x dv_y dv_z = (\frac{m}{2\pi k_B T})^{3/2} exp[-\frac{m({v_x}^2 + {v_y}^2 + {v_z}^2)}{2k_B T}] \tag{2.10}$$

this however can then create a situation in which the whole cluster is given a net velocity in one direction. This is then remediated by setting as zero the center of mass velocity, by making a subtraction from each atomic velocity, and then rescaling all of them so that the temperature is the one assigned.

So at each step the forces are calculated using the chosen atomistic potential, and then so are the accelerations, dividing by the masses. Finally an algorithm is used to go to the next step and, each tens or hundreds of steps, the output file with all positions is printed. The

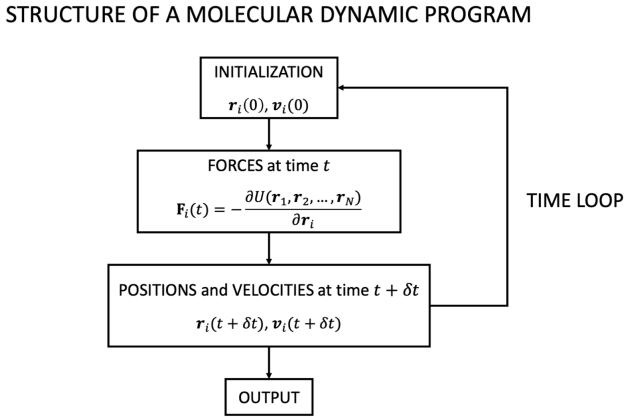

Fig. 2.1 The schematic representation of a MD simulation.

choice of the algorithm is very important for the simulation to work. The most obvious choice, given the initial velocities by a chosen temperature and a potential to calculate inter-atomic forces, would be the Euler algorithm:

$$\mathbf{r}_i(t+\delta t) = \mathbf{r}_i(t) + \mathbf{v}_i(t)\delta t + \frac{1}{2}\mathbf{a}_i(t)\delta t^2 \tag{2.11}$$

$$\mathbf{v}_i(t+\delta t) = \mathbf{v}_i(t) + \mathbf{a}_i(t)\delta t \tag{2.12}$$

However it is immediate to see that this is not a very good choice in that energy is not conserved: one can see that the first of these equations is not invariant for a temporal inversion $\delta t -> -\delta t$, which implies the presence of an energetic drift.

In this thesis the velocity-Verlet algorithm was used [36], which is the most common choice in general for MD simulations. In this scheme, the equations of motion are integrated as follows:

$$\mathbf{r}_i(t+\delta t) = \mathbf{r}_i(t) + \mathbf{v}_i(t)\delta t + \frac{1}{2}\mathbf{a}_i(t)\delta t^2 \tag{2.13}$$

$$\mathbf{v}_i(t+\delta t) = \mathbf{v}_i(t) + \frac{1}{2}\left[\mathbf{a}_i(t) + \mathbf{a}_i(t+\delta t)\right]\delta t \tag{2.14}$$

where $\mathbf{r}_i(t)$, $\mathbf{v}_i(t)$ and $\mathbf{a}_i(t)$ are the position, velocity and acceleration of atom i, respectively, and δt is the time step. This eliminates the problem of the energy drift and it is observed in practice that the energy fluctuations stay on the order of $\Delta E/E < 10^{-5}$ which is considered acceptable. The lack of energy drift is insured by verifying the equivalence with the Verlet algorithm which is:

$$\mathbf{r}_i(t+\delta t) = -\mathbf{r}_i(t-\delta t) + 2\mathbf{r}_i(t) + \mathbf{a}_i(t)\delta t^2 \tag{2.15}$$

which can be done by writing the needed terms of positions and eliminating the velocities. The velocity-Verlet and the Verlet algorithm are accurate in predicting positions to the $O(\delta t^4)$ term.

This check on energy conservation is relevant because of physicality but the microcanonical ensemble (N, V, E) is not a good descriptor for most experiments. Usually the canonical ensemble (N, V, T) is a better starting point, meaning that a mechanism exists that keeps the system at a certain temperature. In the case of growth simulations (where N is going to change as would T when heating/freezing), that role is taken by some inert gas as Helium/Argon that constitutes the atmosphere of the condensation process, as in the condensation chamber in Fig. 2.2. This requires to include in the algorithm a *thermostat*, meaning a further step in which some random atoms are given new velocities according to the Maxwell distribution for a given temperature. This at least is the working principle of the Andersen thermostat [36, 46], which also requires the velocity-Verlet algorithm to be adopted, as opposed to some other algorithms, such as the Verlet one[36], which does not explicitly include velocities. As a collision frequency for our simulations we took the commonly used value $5 \cdot 10^{11}$ s^{-1} [14, 47]. Another possible choice for the thermostat would be the Langevin thermostat, which would however require to modify the equation of motion in order to add a friction term: it has been seen in general that these two choices are equivalent. While we have no way currently to directly simulate the inert atmosphere, the high thermal conductivity within the metal cluster makes it improbable that having only the external layer loose energy to the gas would change the outcome.

In the case of growth simulations the starting cluster, the seed, is assumed to be hit from all directions by new atoms, in a random pattern. Each new atom is added in the course of the simulation with a velocity taken from the Maxwell distribution, in a random position within a certain distance from the seed, always pointing toward the center of the seed. This way what could take place in a gas phase condensation experiment, within an experimental setup such as that in Fig. 2.2, is simulated. The rate at which new atoms are added is of course a relevant parameter just like temperature, and we usually fixated it as $0.1 - 1$ atoms/ns. A lower growth rate could have 'advantages' similar to those of an higher temperature, giving to the cluster more time to reach an equilibrium before a new atom impact it. The choice of having the velocity pointed to the center of the seed also implies the loss of a 'cut' component of it that is however of secondary importance: cohesion energies are of the order of some eV which is equivalent to tens of thousands of Kelvin degrees of temperature.

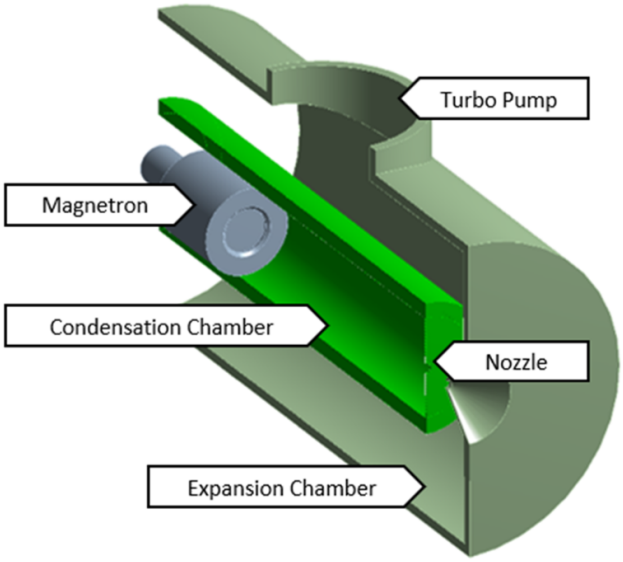

Fig. 2.2 A representation of a magnetron sputtering source with the condensation chamber between the magnetron and the nozzle. Reproduced from Ref. [48]; copyright 2021 Author(s).

2.3 Minimization and quenching

While MD simulations are needed to explore possible configurations and physical trajectories, it is also useful to have the final, or initial, configuration set to a local minimum. To achieve such relaxation a Broyden-Fletcher-Goldfarb-Shanno (BFGS) algorithm can be employed [49, 50], meaning that a series of iterative approximations to the Hessian matrix is adopted to find the descent direction, and follow it to the local minimum. This has the advantage to be a fast method and we will adopt it as our usual choice. It also is possible to adopt a *quenched* molecular dynamics algorithm [51]: in this case the usual procedure of molecular dynamics is adopted, except each time the velocity runs opposite to the calculated force, the program sets it to zero. This is the procedure we will adopt in the context of the *drag method* [51], which requires the minimization to be bounded with regard to certain coordinates, as well as a greater precision in finding the local minimum. In this case an initial temperature must be given for the algorithm to work: we will always use 300K.

2.4 Pressure analysis

We are interested in the calculation of the pressure on each one atom of the cluster, which we can write down as:

$$p_i = -\frac{dE_i}{dV_i} \tag{2.16}$$

based on simple classical mechanics. We then put:

$$p_i = -\frac{dE_i}{d\alpha}\frac{d\alpha}{dV_i} \tag{2.17}$$

where α is a parameter we introduce so that, due to simple dimensional considerations:

$$r_{ij}(\alpha) = \alpha r_{ij}(1) \tag{2.18}$$

$$V_i(\alpha) = \alpha^3 V_i(1) \tag{2.19}$$

for the distances of each pair of atoms and the volume of each atom respectively. For the potential energy then:

$$\frac{dE_{ij}}{d\alpha} = \sum_{i!=j}\frac{dE_i}{dr_{ij}}\frac{dr_{ij}}{d\alpha} \tag{2.20}$$

meaning:

$$\frac{dE_{ij}}{d\alpha} = \sum_{i!=j}\frac{dE_i}{dr_{ij}(1)} r_{ij}(1) \tag{2.21}$$

Then, of course putting $\alpha = 1$ for the result, we finally have:

$$\frac{d\alpha}{dV_i(\alpha)} = \frac{1}{3\alpha^2 V_i(1)} = \frac{1}{3V_i} \tag{2.22}$$

$$p_i = -\frac{1}{3V_i}\sum_{i!=j}\frac{dE_i}{dr_{ij}} r_{ij} \tag{2.23}$$

The results are then processed in order to produce images of NPs as that in Fig. 2.3

Negative pressure corresponds to tensile stress on the atom, averaged over all directions, while positive pressure corresponds to compressive stress. An atom with negative pressure is a candidate for replacement by a larger atom, while the opposite is true for an atom with positive pressure. The negative pressures of surface atoms are a consequence of the correlation between bond order and bond length in metals, which is well reproduced by the SMATB potential. Bond lengths are contracted for low-coordination atoms, so that they can recover their ideal lattice positions when replaced by larger atoms. On the other hand, negative pressures of internal atoms are a reliable indicator of poor structural stability, as

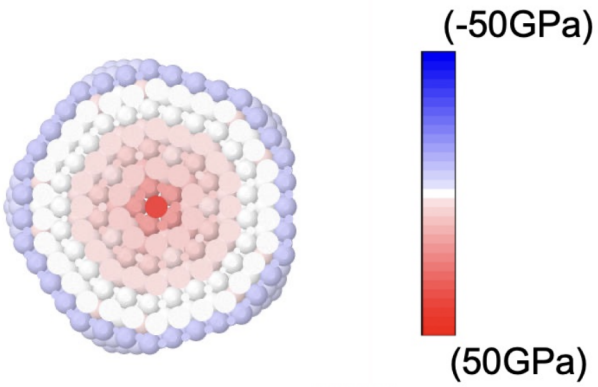

Fig. 2.3 Pressure map of Ag Mackay icosahedron (1415 atoms).

is positive pressure for surface atoms. The stability test we perform consists of exchanging atoms between layers of different atomic species [14].

2.5 DFT calculations

The complete hamiltonian for a nanoparticle with N atoms and a total of m electrons, is, in Hartree atomic units:

$$H = -\frac{1}{2}\sum_i \nabla_i^2 - \frac{1}{2}\sum_I \frac{\nabla_I^2}{M_I} + \frac{1}{2}\sum_{i\neq j}\frac{1}{|\mathbf{r}_i - \mathbf{r}_j|} - \sum_{i,I}\frac{Z_I}{|\mathbf{r}_i - \mathbf{R}_I|} + \frac{1}{2}\sum_{I\neq J}\frac{Z_I Z_J}{|\mathbf{R}_I - \mathbf{R}_J|}, \tag{2.24}$$

where $\{\mathbf{R}\}$ are the positions of nuclei, $U(\{\mathbf{R}\})$ is the potential energy of the nanoparticle, the first two terms represent the kinetic energy operators of electrons and nuclei respectively, the third term represents electron-electron interactions, the fourth electron-nuclei interactions and the last one represents the interactions between nuclei, each with a positive charge Z_I. In order to manage this equation, there are approximations that need to be made; particularly the Born-Oppenheimer approximation [52], meaning we separate the nuclei, which are taken as fixed, and the electrons contributions, gives us:

$$H_{el} = -\frac{1}{2}\sum_i \nabla_i^2 + \frac{1}{2}\sum_{i\neq j}\frac{1}{|\mathbf{r}_i - \mathbf{r}_j|} - \sum_{i,I}\frac{Z_I}{|\mathbf{r}_i - \mathbf{R}_I|} \tag{2.25}$$

as an electronic hamiltonian, with a term for electrons being influenced by a field generated by nuclei, which implies a time-independent Schrödinger equation:

$$H_{el}\psi_k(\{\mathbf{R}\};\{\mathbf{r}\}) = E_k(\{\mathbf{R}\})\psi_k(\{\mathbf{R}\};\{\mathbf{r}\}), \tag{2.26}$$

where $\psi_k(\{\mathbf{R}\};\{\mathbf{r}\})$ are eigenstates of electrons, in which fixed position of nuclei play the role of parameters, being the positions of the electrons $\{\mathbf{r}\}$ the only variable. The complexity of the problem is then reduced to finding the ground state of this equation, which is then taken as the potential energy of the nanoparticle. The DFT strategy for solving this problem is made possible by the theorems by Hohenberg and Kohn [53, 54]. For a state ψ, the electron density is defined as

$$n(\mathbf{r}) = \langle\psi|\sum_{i=1}^{m}\delta(\mathbf{r}-\mathbf{r}_i)|\psi\rangle \tag{2.27}$$

The theorems state that it is possible for any system to define an energy functional of the electron density $E[n]$, that the ground state energy of the system is the global minimum of $E[n]$ and that the ground state density $n_0(\mathbf{r})$ is the one that minimizes $E[n]$, where $n_0(\mathbf{r})$ is the electron density associated with the ground state ψ_0. Therefore, it is possible to reduce the problem to a variational calculation:

$$\frac{\delta}{\delta n}\left\{E[n]-\lambda\left[\int d\mathbf{r}\, n(\mathbf{r})-m\right]\right\} = 0, \tag{2.28}$$

where λ is a Lagrange multiplier due to the normalization of the electron density to the total number of electrons m. We then have:

$$E[n] = \langle\psi|H_{el}|\psi\rangle, \tag{2.29}$$

which can be written as

$$E[n] = F[n] + \int d\mathbf{r}\, n(\mathbf{r})V_{ext}(\mathbf{r}), \tag{2.30}$$

where $V_{ext}(\mathbf{r}) = -\sum_I Z_I/|\mathbf{r}-\mathbf{R}_I|$ is the external field of nuclei and $F[n]$ is a universal functional of the electron density, including kinetic energy and electron-electron interactions:

$$F[n] = T[n] + \int\int d\mathbf{r}d\mathbf{r}'\,\frac{n^{(2)}(\mathbf{r},\mathbf{r}')}{|\mathbf{r}-\mathbf{r}'|}. \tag{2.31}$$

In the last equation, $T[n]$ is the kinetic energy functional, and $n^{(2)}(\mathbf{r},\mathbf{r}')$ is the two-particle density. The analytical form of the latter is not known, but it can be decomposed in two parts: $n^{(2)}(\mathbf{r},\mathbf{r}') = n(\mathbf{r})n(\mathbf{r}') + \Delta n^{(2)}(\mathbf{r},\mathbf{r}')$, in which the first term is the product of densities, which

would correspond to $n^{(2)}(\mathbf{r},\mathbf{r}')$ for a system of uncorrelated particles, and the last term is a correction needed for the correlated electrons. Thus

$$F[n] = T[n] + \int\int d\mathbf{r}d\mathbf{r}' \frac{n(\mathbf{r})n(\mathbf{r}')}{|\mathbf{r}-\mathbf{r}'|} + \Delta E \tag{2.32}$$

A similar decomposition can be done for the kinetic energy. For a system of non interacting particles, a wavefunction can be chosen in the form of a Slater determinant. In this case, the kinetic energy functional can be written simply as

$$T[n] = -\frac{1}{2}\sum_i \int d\mathbf{r}\, \phi_i^*(\mathbf{r})\nabla^2\phi_i(\mathbf{r}), \tag{2.33}$$

where $\phi_i(\mathbf{r})$ are the single-particle orbitals used for building the Slater determinant. For a system of interacting electrons, then:

$$F[n] = -\frac{1}{2}\sum_i \int d\mathbf{r}\, \phi_i^*(\mathbf{r})\nabla^2\phi_i(\mathbf{r}) + \int\int d\mathbf{r}d\mathbf{r}' \frac{n(\mathbf{r})n(\mathbf{r}')}{|\mathbf{r}-\mathbf{r}'|} + \Delta E + \Delta T, \tag{2.34}$$

where ΔT is the correction needed to recover the true kinetic energy of the system. Putting all together, we have

$$E[n] = -\frac{1}{2}\sum_i \int d\mathbf{r}\, \phi_i^*(\mathbf{r})\nabla^2\phi_i(\mathbf{r}) + \int\int d\mathbf{r}d\mathbf{r}' \frac{n(\mathbf{r})n(\mathbf{r}')}{|\mathbf{r}-\mathbf{r}'|} + \int d\mathbf{r} n(\mathbf{r})V_{ext}(\mathbf{r}) + E_{xc}, \tag{2.35}$$

The problem then becomes to treat the term $E_{xc} = \Delta E + \Delta T$, which includes all electron-electron interactions. It is in fact possible to rewrite the system of equations with the use of an effective potential, in the so called Kohn-Sham equations, while a term $\delta E_{xc}[n]/\delta n(\mathbf{r})$ will remain as part of this potential. Then, in the case of LDA (Local Density Approximation) [55], the functional for the exchange correlation term is evaluated with regard to an homogeneous electronic gas by a Monte-Carlo interpolation. There are other possible choices such as LSDA (Local Spin Density Approximation) or GGA (Generalized Gradient Approximation), which are improvements on LDA. In Refs.[14] GGA will be used as described in Refs.[56], implemented with the software QUANTUM ESPRESSO [57]. In any case the Kohn-Sham equations:

$$\left[-\frac{1}{2}\nabla^2 + V_{eff}\right]\phi_i(\mathbf{r}) = \varepsilon_i\phi_i(\mathbf{r}), \tag{2.36}$$

where we defined the effective potential

$$V_{eff}(\mathbf{r}) = V_{ext}(\mathbf{r}) + \int d\mathbf{r}' \frac{n(\mathbf{r}')}{|\mathbf{r}-\mathbf{r}'|} + \frac{\delta E_{xc}}{\delta n(\mathbf{r})}. \tag{2.37}$$

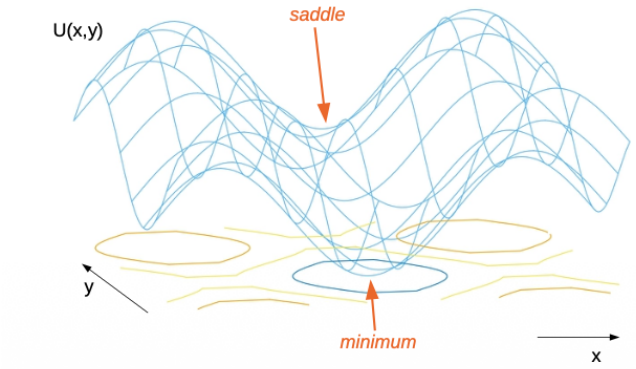

Fig. 2.4 PES as a function of only two variables, x and y, in order to help with visualization. There are a variety of local minima that are connected through saddle points.

will have to be solved. While this is possible for a system of a few atoms, it confines the use of DFT to such small clusters and ground state calculations, leaving the treatment of temporal evolutions to MD simulations or other methods.

2.6 Global optimization

The key premise of global optimization searches is the concept of PES (potential energy surface), meaning that the potential energy of the NP under consideration can be thought as a function of all atomic coordinates. The PES is the 'energy landscape' we are interested to explore in search for the lowest-energy structure, and it will in general be a complex function as in Fig. 2.4, with many minima and saddles. If the lowest-energy structure is searched for, it is not possible to simply go toward an immediate energy decrease, as would be the case for minimization and quenching.

The lowest-energy structure can be searched for, even in clusters of greater size than those studied with DFT, by taking a Gupta potential and exploring the potential energy of a variety of possible configurations. In the limit $T \to 0$, the global minimum of potential energy tends to become the structure of the cluster with probability 1. In general, even at higher temperatures, the global minimum is a stable configuration, often the most stable of all. This means that, particularly for experiments at low temperature, this technique can have predictive value. Together with the use of Gupta potentials, we also eliminate from our model quantum effects as the zero-point energy, which could perhaps have some relevance at very low temperatures. The global minimization approach can then be generalized by taking into account some thermal effects [58].

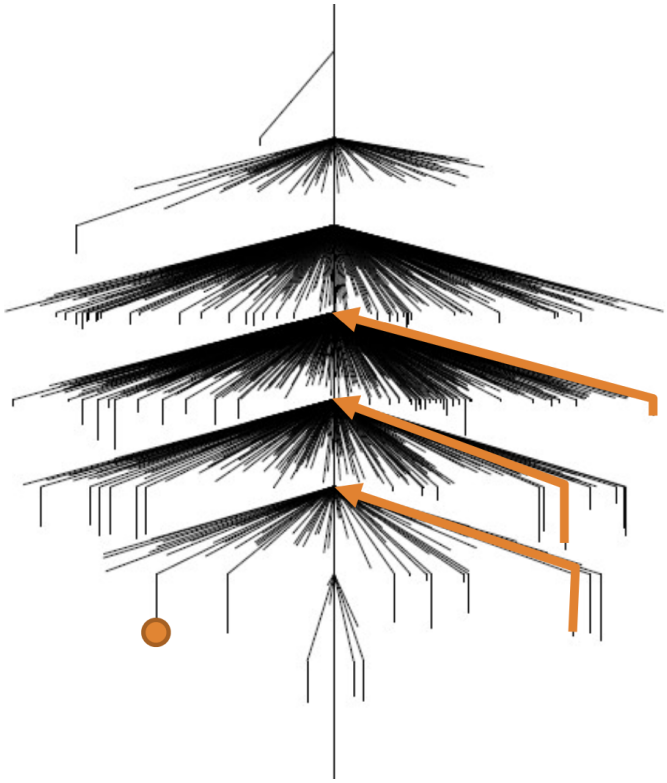

Fig. 2.5 Disconnectivity graph of LJ_{13} is represented, meaning all the possible direction that a search for minimum energy (lower energy is down) could take beginning with some high energy arrangement. While in this case there is a clear global minimum down it all, it really is the case that if a local minimum (orange circle) is reached then it is difficult to go further down with some small modification of the structure.

The difficult part of this exploration consists in finding the lowest-energy structure making subsequent modification on the initial cluster, which can be a disordered cluster with a certain amount of atoms of one or more chemical species as well as the result of some MD simulation or other. It is both important to have an algorithm that explore a huge variety of different shapes, and possibly chemical orderings, and for the algorithm to select away those shapes or chemical orderings that are not promising in that sense. The risk however of dropping away too fast some non-optimal configuration is that the configuration could be a sub-optimal structure in a relevant 'funnel' as that in Fig. 2.5 and 2.6.

There are different strategy to deal with this problem, which in terms of computational theory can be categorized as NP-hard, as the well known 'traveler's problem' [59], meaning nor polynomial (the computational effort scale exponentially with the number of atoms) nor with a solution verifiable with a polynomial algorithm. One such solution is simulated annealing, meaning the simulation of a process of fast cooling, which however is both very

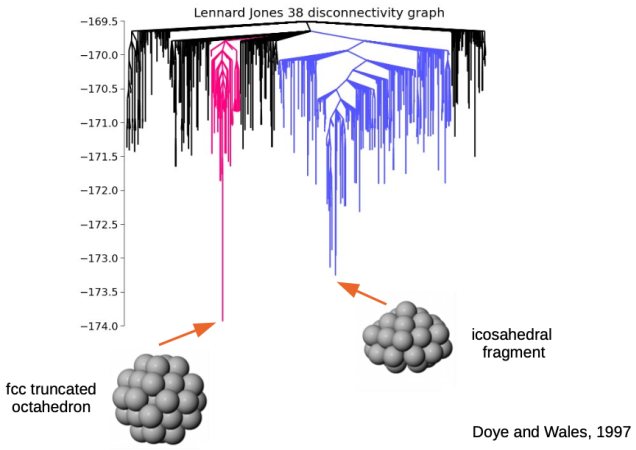

Fig. 2.6 Disconnectivity graph of LJ_{38}. There are two competing minima of a different kind: Ih and TO; while TO is the lowest, the two funnel are still very much separated in the disconnectivity graph.

time-consuming and very often able to explore only one 'funnel' at a time, being therefore not suitable for complex multi-funnel energy landscapes. Another solution is that of genetic algorithms [60], meaning that a number of different clusters are taken to evolve separately to preserve diversity, while new modifications are made on the file in a compressed form. What we used [14], is the basin-hopping algorithm [61, 62], meaning each new configuration has a possibility of being accepted based on the rule [63]:

$$p = \exp(-\Delta U'/k_B T), \tag{2.38}$$

provided that $\Delta U' > 0$, and $p = 1$ otherwise. The rule is always applied to locally minimized structures. This is the Metropolis-Hastings rule: it strucks a good compromise between going down to lower-energy structures and keeping a possibility to climb back a dead end funnel. The temperature in the formula is something that we establish, and it is usually taken as 1000-2000K for variations that alter the shape of the NP, and 100-300K for modifications that alter the chemical ordering [3, 35].

The remaining issue is that of generating variations on a given structure to then select according to the basin-hopping criterion. This we do by making some moves, that is some change of atomic positions. There are different types of moves: those are, in the most common implementations of the basin-hopping algorithm, the *shake*, *Brownian* and *exchange moves*. In a *shake move* each atom is displaced randomly inside a sphere or cube, which for metal NPs is taken as usually the size of half the nearest-neighbour distance: this way it is possible to explore different global configurations while avoiding too much distorted structures that would almost surely have a much higher potential energy. In a *Brownian*

move each atom is given a displacement according to a MD-calculated trajectory, which is generated by assuming for this specific purpose a temperature of 1500-2500K and running the MD algorithm for a few picoseconds: this also helps exploring the possible geometries of the cluster in a more natural way, while the very high temperature helps to have a fast evolution toward a different shape. Finally, in order to vary the chemical ordering, the *exchange move* is adopted, meaning at each iteration two atoms of a different chemical species are swapped, either randomly or with an assigned probability given by the position.

Chapter 3

General theory for icosahedral shells

In this chapter, the theory published in Ref. [14] is presented, which explains how to pack icosahedral shells, built by cutting and folding an hexagonal lattice, following the work of Caspar and Klug [15].

The Caspar-Klug method of cutting and folding, which is presented in section 3.1, dates back to 1962 and has initially been proposed to explain the form of viral capsids, but more generally it can help conceptualize icosahedral surface structures (single layers) whether in bio-structures, colloids or metal NPs, as in our case. In the first section some attention is given to the viral capsids problem that motivated the Caspar-Klug method in the first place. This method cannot however be directly applied to NPs, which are multi-layer aggregates.

In section 3.2, the development of this theory in order to describe the building of a whole NP is exposed, beginning with the main concept of a variety of growth paths where a series of icosahedral shells are put together, one on top of the other, each described by a pair of numbers (h, k). This section also includes the explanation of the **chirality classes**, based on the numbers (h, k), as well as the generalization of these classes to describe anti-Mackay and generalized anti-Mackay shells.

Finally, in section 3.3 the rules, found in Ref. [14] for the selection of bi-metallic and multi-metallic systems suitable for building a given icosahedral aggregate, are exposed and justified. Some example are also given of LJ and Morse calculations used to validate these rules for a variety of atomistic potentials, while growth simulations are left for the next chapter, together with atomic pair exchanges [14] and pressure analysis. These rules are based on the size mismatch between the different atomic species of an alloy, meaning the different atomic radius or bulk lattice constant. We used them to make prediction on some bi-metallic systems to then compare with MD simulations.

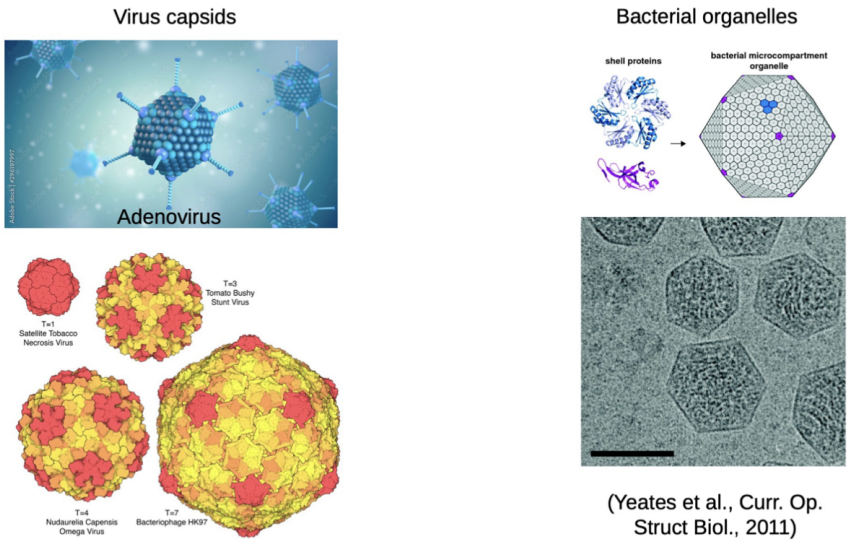

Fig. 3.1 On the left: viral capsids, which are icosahedral protein layers. On the right: the same shape also occurs in bacterial organelles. See Refs. [64, 65]. Copyright 2011 Elsevier.

3.1 Caspar-Klug method

The recurrence of icosahedral shapes in a variety of biological structures as in Fig. 3.1 is a well documented fact [64, 65] as it is for metal NPs and colloids [66].

The case of viral capsids is particularly interesting in that the reproductive cycle of a virus implies instructing a live cell to fabricate the protein capsids. The protein capsids is made of different units which are initially on a plane and then fold (see more generally on **protein folding** Refs. [67, 68]) to form the capsid. This motivated Caspar and Klug in 1962 [15] to think of fabricating an icosahedral shell by cutting and folding an hexagonal plane as that in Fig. 3.2;

This method requires to cut twenty triangular facets as in Fig. 3.3 and to then fold them with two vertices, north and south, being obtained from joining five facets. It is immediate to see that if the twenty facets are cut with one side all along the h axis, then the area of a single facet will turn out to be $A = \frac{\sqrt{3}}{4} * h^2$ meaning that we can introduce a triangulation number $T = h^2$ so that $A = \frac{\sqrt{3}}{4} * T$. Then the number of atoms in the whole surface will be:

$$N = 10 * T + 2 \tag{3.1}$$

with the additional two atoms being the north and south 'pole' of our folded icosahedron.

This however can be made more general by considering the possibility of cutting the edges of our icosahedron not parallel to the h axis but with an angle θ_{CK} as in Fig. 3.4. It is

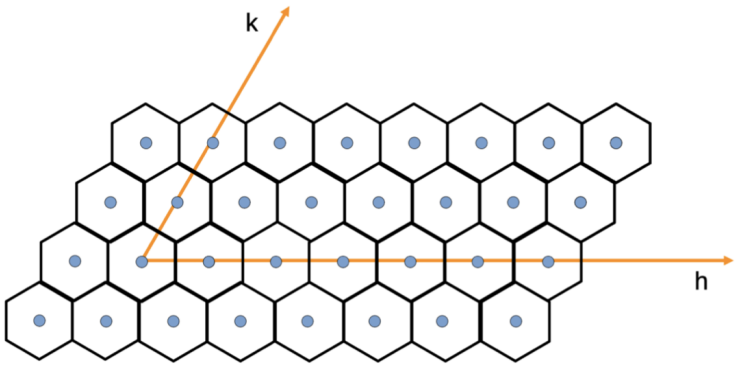

Fig. 3.2 The two axis h and k form a 60° angle. The atoms are in the center of the hexagonal cells. See Ref. [15].

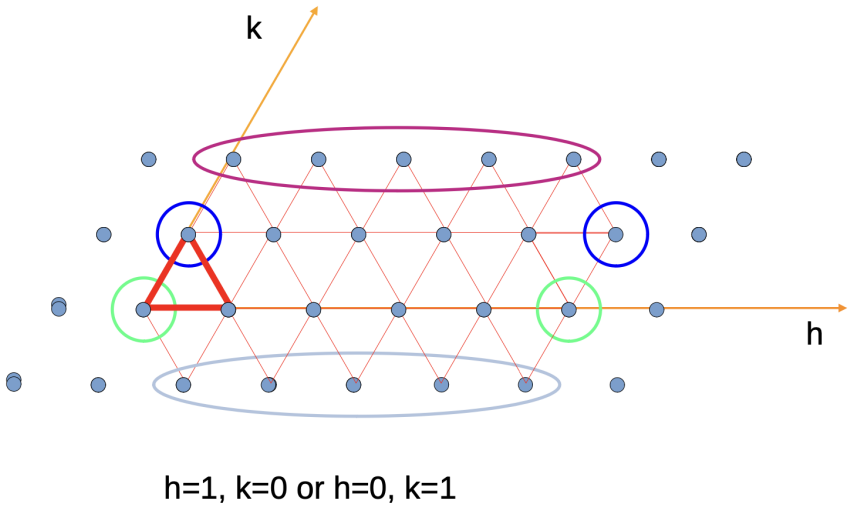

Fig. 3.3 The cutting and folding of an icosahedral layer with $h = 1$ and $k = 0$. An edge of unit length is taken along the h axis. Points within circles of the same color are joined together in the folding process.

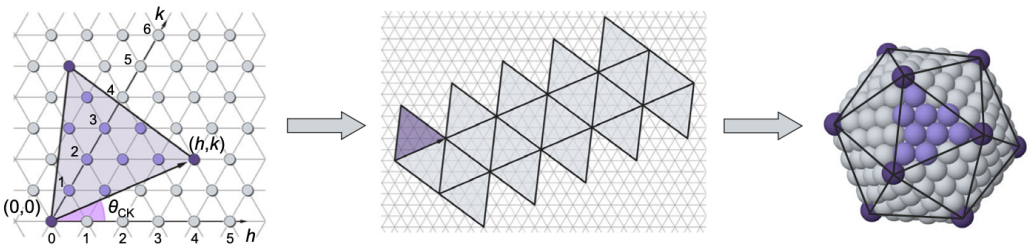

Fig. 3.4 The cutting and folding of an icosahedral layer with given h and k, forming an angle θ_{CK}. One can see that the resulting icosahedral layer has a certain chirality and there is no complete edge between two vertices. Reproduced from [14]. Copyright 2025 Nature publishing group.

possible then to write for the angle:

$$\cos\theta_{CK} = \frac{2h+k}{2\sqrt{T}} \tag{3.2}$$

and

$$\sin\theta_{CK} = \frac{\sqrt{3}k}{2\sqrt{T}} \tag{3.3}$$

where the triangulation number T in general is given by:

$$T = h^2 + k^2 + hk \tag{3.4}$$

It is important here to recall the concept of a chiral icosahedral layer as that in Fig. 3.4. This in general means that there is no mirror symmetry: if a reflection is made, then no rotation can bring the reflected structure (the enantiomer) into correspondence with the initial figure. It is easy to see that unless one has h=k, meaning $\theta_{CK} = 30^\circ$, h=0 or k=0, meaning $\theta_{CK} = 0^\circ$ or $\theta_{CK} = 60^\circ$, then there is chirality. This last case, where either h or equivalently k is null, is the familiar Mackay icosahedron [16], while the former is the so called Bergman icosahedron [69, 70]. In all other case the choice between h>k or h<k is that between the two enantiomers. We usually consider h<k in our work as a convention.

It is interesting to note that chirality has also been observed in viral capsids as in Fig. 3.5 and has already been described according to the Caspar-Klug construction.

What can then also be done, as in Ref. [14], is to classify all possible manifestation of chirality into chirality classes. When h=1 the resulting layer will be 1-chiral (Ch1), when h=2 it will be 2-chiral (Ch2) and so on, as one can see in Fig. 3.6.

Every icosahedral layer of any size and class will therefore be identified by a pair of numbers (h, k). However there also is another possibility: a layer could be of anti-Mackay

Fig. 3.5 Image reconstruction of the special structure associated with 72 pentamers of the genome-free polyoma capsid. Reproduced from [71]. Copyright 1989 Elsevier.

.

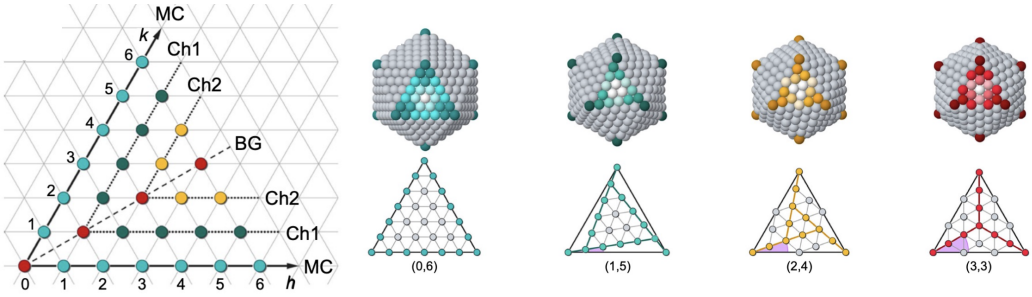

Fig. 3.6 The different chirality classes form Mackay to Ch2 and Bergman; it is possible to see that only in the Mackay icosahedron there are complete edges between two vertices. While the Mackay and Bergman types are a-chiral, every other class comes in two enantiomers. Reproduced from [14]. Copyright 2025 Nature publishing group.

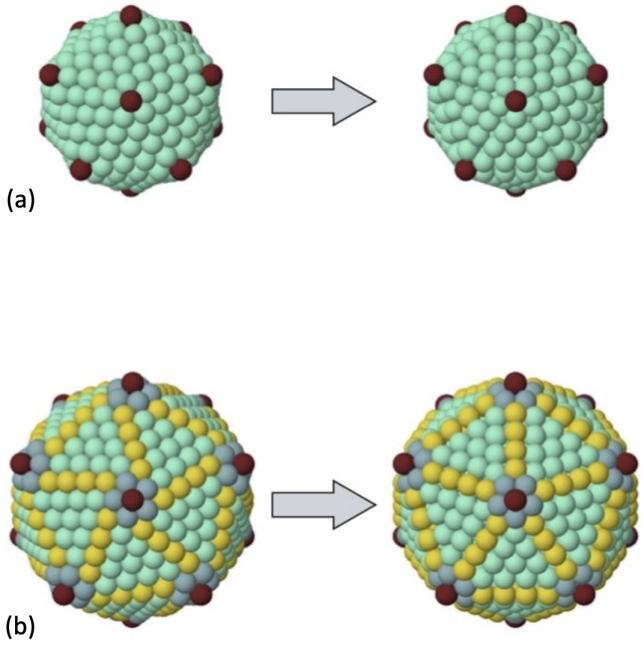

Fig. 3.7 (a) The Ch1 → AM1 transformation. (b) The Ch2 → AM2 transformation. It is easy to see that in both cases a collective distortion leads from the anti-Mackay/pentakis to the chiral icosahedral type. The non close-packed part of the anti-Mackay icosahedral type is eliminated in the process. Adapted from Ref. [14]. Copyright 2025 Nature publishing group.

icosahedral type. As it has been already seen in the case of a Ch1 shell, it is possible to put these anti-Mackay layers in correspondence with chiral ones, so that (h, k)* will have the same number of atoms as (h, k) [14]. This is a generalization of the fact that the common anti-Mackay layer is like a distorted Ch1 one [14], as one can see in Fig. 3.7. In literature these generalized anti-Mackay are also known as pentakis dodecahedral structures [72].

The central issue in this equivalence is to prove that N(h, k)*=N(h, k), meaning the general correspondence of the anti-Mackay and chiral types. To do that one can (see Fig. 3.8) put for the anti-Mackay:

$$N_T = \frac{p^2 + p}{2} \tag{3.5}$$

where N_T is the number of atom in the close-packed equilateral triangle and p the number of atoms on the side of it; then:

$$N_S = 3\frac{pq}{2} \tag{3.6}$$

where N_S is the number of atoms in the square-like part of the surface, disposed parallel to the equilateral triangle side, and q the number of atoms between the vertex of the facet and

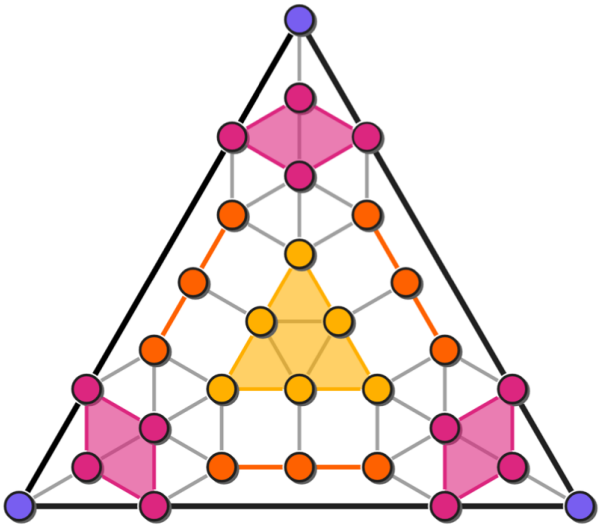

Fig. 3.8 Anti-Mackay facet characterized by two numbers p and q. The N_T atoms are colored in yellow, the N_S in orange and the N_D in pink. Adapted from supplementary notes of Ref. [14]. Copyright 2025 Nature publishing group.

that of the close-packed equilateral triangle. Finally:

$$N_D = 3\frac{q^2+q}{2} \tag{3.7}$$

is the number of all the remaining atoms inside the facet, that is not counting the vertices. If we sum all of these, multiply by 20 and add the 12 vertices, we get:

$$N(p,q) = 10(p^2+3q^2+3pq+p+3q+1)+2 \tag{3.8}$$

which can be written as

$$N(h,k) = 10T(h,k)+2 \tag{3.9}$$

with

$$h = q+1 \tag{3.10}$$

and

$$k = p+q \tag{3.11}$$

proving that we can identify these layers with a pair (h, k)*.

All of this is exclusively about building single layers, but it is possible on that basis to design all the different icosahedral NPs as made by adding layers one on top of the other.

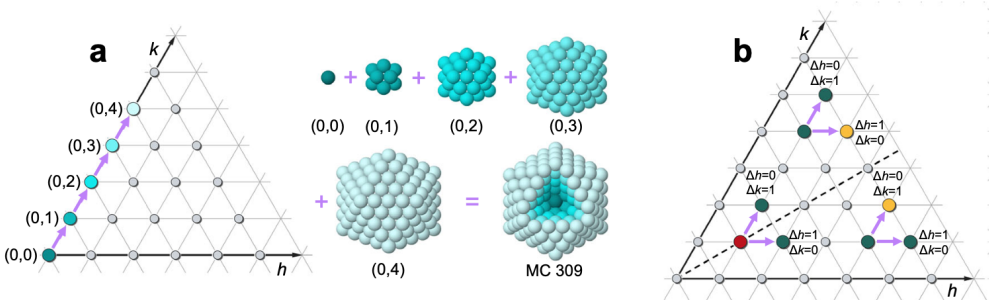

Fig. 3.9 (a) The sequence of layers that form a Mackay regular icosahedron. (b) The general rule for a step from one layer to the other, with two alternatives: the yellow circle means a new layer with a different chirality class, except when starting from a Bergman layer (red circle) which would mean that there's no way to avoid such change and the choice is between two enantiomers. Reproduced from Ref. [14]. Copyright 2025 Nature publishing group.

3.2 Packing shells

If it is possible to identify each layer with a pair (h, k), then a sequence of such pairs will identify an icosahedral aggregate, with (0, 0) being the central atom. It is immediate to see, as in Fig. 3.9, that the Mackay icosahedron is described by a sequence of pairs all with k=0 (because of our convention: we could as well have chosen h=0) [16, 73]. More in general however it is always possible to move from a pair (h, k) either to (h+1, k) or to (h, k+1). If it is assumed that h>k, then incrementing k by one will lead to a further layer with comparatively less atoms, meaning that we expect to need a change to a different atomic species, one with a greater atomic radius, for it to be a stable structure, while the opposite hold if h<k. This will be better explained in 3.3.

One could potentially also consider paths that require to add more than one to either h or k or to add something to both, but it is easy to see that in such a case one would have to add atoms with lower atomic radius, which however would be better placed at the center of the aggregate. Thus the general rule is that from (h, k) one can either move to (h+1, k+1) or to (h, k+1), increasing only one of the two indices of just 1.

This is also true if one has in the beginning h=k, meaning a Bergman layer. Because of that, it is easy to see that there is a particular sequence that requires to have various symmetry breakings, and that is the so called Bergman sequence: each time there is a Bergman layer one has to grow by adding either left or right chiral layers as shown in Fig. 3.9 (b), and in Fig. 3.10.

For each of these sequence, each describing a particular icosahedral aggregate, or NP in our case, it is then possible to calculate the final number of atoms by adding all the atoms of

each layer:

$$N = \sum_{l<i} [10\,T(h(l),k(l)) + 2] - 1 \tag{3.12}$$

where i is the number of layers including the atom at the center, for which however the formula $10T+2$ is not valid in that it would give 2 atoms; so we subtract 1 at the end of the calculation. This can be done particularly in a number of known cases, beginning with recovering the magic numbers, meaning the numbers for a completed structure with i number of layers, for the Mackay icosahedron:

$$N_{MC}(i) = \sum_{k<i-1} [10\,T(k,0) + 2] - 1 \tag{3.13}$$

where i is the number of layers and the -1 is to avoid counting two atoms at the center. This gives

$$N_{MC}(i) = \sum_{k<i-1} (10k^2 + 2) - 1 \tag{3.14}$$

$$N_{MC}(i) = \frac{10}{3}i^3 - 5i^2 + \frac{11}{3}i - 1 \tag{3.15}$$

This gives the familiar sequence 1, 13, 55, 147, 309, 561, 923, ... Now let's suppose that from a certain point one decides to add j new layers of Ch1 type. In this case there will be a chiral shell that has a number of atoms:

$$N_{Ch1}(j) = \sum_{i-1<=k<i+j-2} [10T(k,1) + 2] \tag{3.16}$$

leading to:

$$N_{Ch1}(j) = \sum_{i-1<=k<i+j-2} [10(k^2 + k + 1) + 2] \tag{3.17}$$

$$N_{Ch1}(j) = \sum_{i-1<=k<i+j-2} (10k^2 + 10k + 2) \tag{3.18}$$

$$N_{Ch1}(i,j) = j\left[10i^2 + \frac{10}{3}j^2 + 10ij - 20i - 10j + \frac{56}{3}\right] \tag{3.19}$$

Then it is possible to sum the atoms in the Mackay core with the atoms in the Ch1 shell, which gives:

$$\begin{aligned} N_{MC@Ch1}(i,j) &= N_{MC}(i) + N_{Ch1}(i,j) = \\ &= \frac{10}{3}i^3 - 5i^2 + \frac{11}{3}i - 1 + j\left[10i^2 + \frac{10}{3}j^2 + 10ij - 20i - 10j + \frac{56}{3}\right] \end{aligned} \tag{3.20}$$

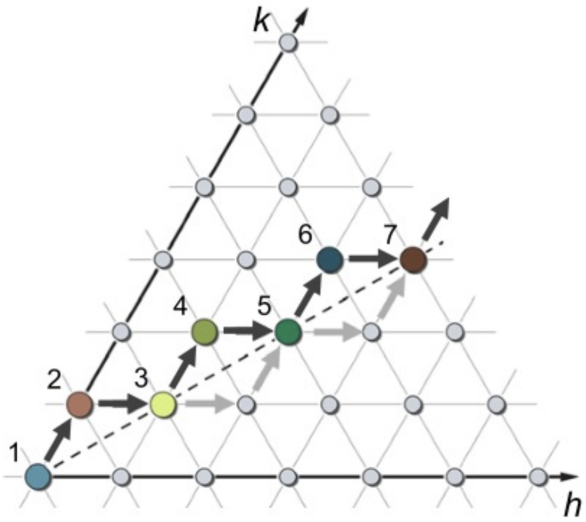

Fig. 3.10 The sequence of Bergman and chiral layers as in this figure requires changing atomic species often. Here this was done at each step, but it would have been possible to avoid it when adding a chiral layer on a Bergman one. Reproduced from Ref. [14]. Copyright 2025 Nature publishing group.

meaning if, for instance, we have a Mackay core of 309 atoms and then only Ch1 layers, the magic numbers are 309, 521, 833, 1265 for one, two, three, four Ch1 layers.

For the BG series instead, meaning a sequence of Bergman and chiral layers like (0, 0), (0, 1), (1, 1), (1, 2), ..., as in Fig. 3.10 we can put:

$$h_{max} = (i-2)/2 \ \text{ for i even or} \tag{3.21}$$

$$h_{max} = (i-1)/2 \ \text{ for i odd} \tag{3.22}$$

and then for i even we have:

$$N = \sum_{h=1}^{h_{max}-1} \sum_{k=h}^{k=h+1} [10(h^2+hk+k^2)+2]-1 \tag{3.23}$$

giving after sum calculation:

$$N = 60 \sum_{h=1}^{h_{max}-1} h^2 + 30 \sum_{h=1}^{h_{max}-1} h + 14 \sum_{h=1}^{h_{max}-1} 1 - 1 \tag{3.24}$$

We then make use of the identities

$$\sum_{0<h<h_{max}} h = \frac{h_{max}(h_{max}+1)}{2} \tag{3.25}$$

$$\sum_{0<h<h_{max}} h^2 = \frac{h_{max}(h_{max}+1)(2h_{max}+1)}{6} \tag{3.26}$$

to finally write, for i even:

$$N = \frac{5}{2}i^3 - \frac{15}{4}i^2 + \frac{9}{2}i - 1 \tag{3.27}$$

Similarly for i odd we obtain:

$$N = \frac{5}{2}i^3 - \frac{15}{4}i^2 + \frac{9}{2}i - \frac{9}{4} \tag{3.28}$$

We then turn to the issue of packing generalized AM (anti-Mackay) layers. This means considering paths as those in Fig. 3.11: in this case due to the way adsorption sites are distributed in the AM facet (see Fig. 3.8), one can only reasonably add on top of it another AM facet with a close-packed triangle of less size, up to reaching the point where the close-packed triangle is that of one atom as for the Bergman icosahedral layer. It is then also possible to add new layer of a chiral type as in Fig. 3.12.

3.3 Size mismatch rules

We have seen that adopting a chiral layer usually require atoms of greater size to compensate for the lower number of them. to quantify this and more in general some size mismatch rules for all possible icosahedral aggregates we turn now to the special case of Mackay icosahedra. It is, for the k-th layer:

$$T = k^2 \tag{3.29}$$

where we put h=0, then for the radius:

$$r = d_{CK} \sin\left(\frac{2\pi}{5}\right) k \tag{3.30}$$

where d_{CK} is the distance in the CK plane. If we have two such layers, one on top of the other, then the inter-shell distance is given by:

$$\Delta r = r(k+1) - r(k) = \tag{3.31}$$

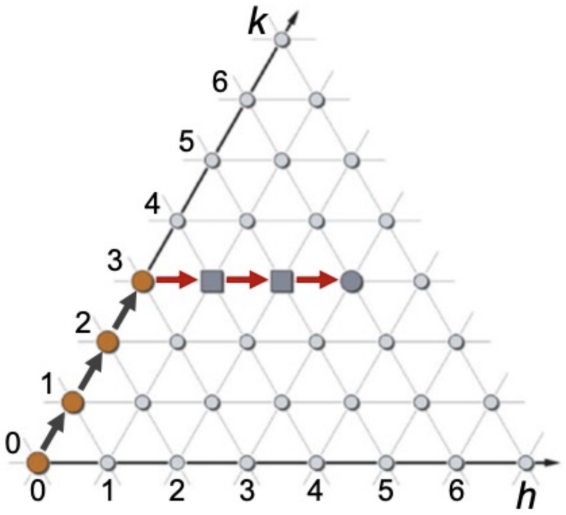

Fig. 3.11 The sequence of AM layers consists in adding AM1 then AM2 and so on up to a Bergman layer. It is possible to do that in growth simulations, based on size mismatch considerations, changing the atomic species only in the first case, and provided that this particular core-shell arrangement cannot support chiralization. Here we considered Cu_{147}@Ag. Reproduced from Ref. [14]. Copyright 2025 Nature publishing group.

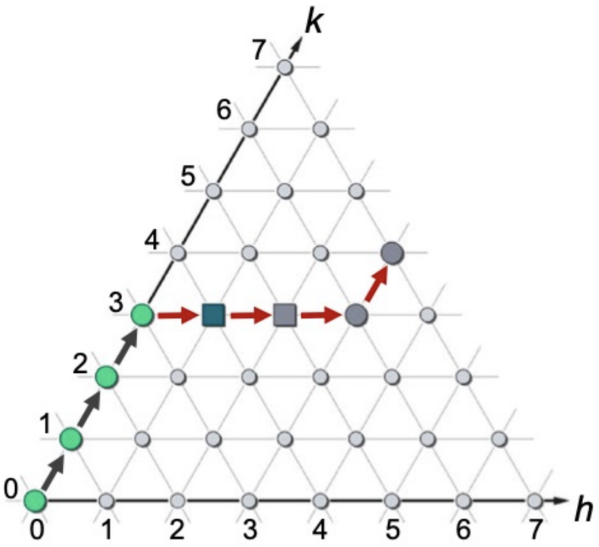

Fig. 3.12 It is also possible to change atomic species more than once: here the tri-metallic system is Ni@Pd@Ag. After the Bergman layer has been completed it becomes possible to add a chiral layer on top of it, which here was done without changing the atomic species. Reproduced from Ref. [14]. Copyright 2025 Nature publishing group.

$$= (k+1)d_{CK}\sin\left(\frac{2\pi}{5}\right) - kd_{CK}\sin\left(\frac{2\pi}{5}\right) = \tag{3.32}$$

$$= d_{CK}\sin\left(\frac{2\pi}{5}\right) \tag{3.33}$$

which is about $0.9511 d_{CK}$, meaning smaller than the intra-shell distance, between atoms of the same layer, by about 5%. This means that clearly both Δr and d_{CK} will not be the ideal distance in the bulk crystal that, unsurprisingly, this being a non-crystalline structure, cannot be the distance between all nearest-neighbours. We then have:

$$d_{CK} = (1+\xi)d \tag{3.34}$$

$$\Delta r = (1-\xi)d \tag{3.35}$$

where d is the ideal distance and:

$$\xi = \frac{1-\sin\left(\frac{2\pi}{5}\right)}{1+\sin\left(\frac{2\pi}{5}\right)} \tag{3.36}$$

which is about 0.0251.

This is the result assuming that the k-th Mackay layer is simply there, but we see that ξ is much smaller than 1, and we will see that this is indeed the right coefficient to then calculate which is the optimal size mismatch for adding a new Mackay layer. We define:

$$\alpha = \frac{d_{SHELL}}{d_{CORE}} \tag{3.37}$$

where d_{SHELL} and the d_{CORE} are the ideal inter-shell distances between the atoms in the core and in the shell respectively. Then the size mismatch is simply

$$sm = \alpha - 1 \tag{3.38}$$

for which we calculate:

$$\Delta r = (k+1)\sin\left(\frac{2\pi}{5}\right)d_{SHELL} - k\sin\left(\frac{2\pi}{5}\right)(1+\xi)d_{CORE} \tag{3.39}$$

which must be equal to $\frac{d_{SHELL}+d_{CORE}}{2}$ as the ideal core-shell distance. This gives us the condition:

$$(k+1)\sin\left(\frac{2\pi}{5}\right)\alpha - k\sin\left(\frac{2\pi}{5}\right)(1+\xi) = \frac{1+\alpha}{2} \tag{3.40}$$

$$\alpha = \frac{2(1+\xi)\sin\left(\frac{2\pi}{5}\right)k+1}{2\sin\left(\frac{2\pi}{5}\right)(k+1)-1} \tag{3.41}$$

from which we see that even adding a new Mackay layer would usually benefit from some size mismatch.

The evaluation of the optimal size mismatch can be extended beyond the Mackay case to the general case of adding any type of icosahedral shell on top of a core. The derivation of the general case in reported in the Supplementary Information of Ref. [14]. Here we report only the final result. The size mismatch for adding a shell on top of a core of i layers is:

$$sm_{i,i+1} = \frac{2(1+\xi)\sin\left(\frac{2\pi}{5}\right)\sqrt{T_i}+1}{2\sin\left(\frac{2\pi}{5}\right)\sqrt{T_{i+1}}-1} - 1 \tag{3.42}$$

In this formula, $\xi \ll 1$ is a coefficient that can be iteratively calculated from the sequence of shells that for the core. If we start from the central atom, $\xi_1 = 0$, and then can be calculated by iterating the following formula up to the i-th layer:

$$\xi_{j+1} = \frac{1-\sin\left(\frac{2\pi}{5}\right)[\sqrt{T_{j+1}} - (1+\xi_j)\sqrt{T_j}]}{1+\sin\left(\frac{2\pi}{5}\right)\sqrt{T_{j+1}}}. \tag{3.43}$$

This formula considers the adjustment of both inter-shell and intra-shell distances at any passage. If the core up to the i-th layer is a Mackay core, we simply recover the already found value for ξ; then we can calculate the optimal sm for both adding a new Mackay layer and a Ch1 one, as in Fig. 3.13. It is then possible to consider the energetic consequence of using atoms with a different size mismatch as in Fig. 3.14.

It is also possible to apply this calculation to other icosahedral aggregates and respective paths, as in Fig. 3.15 where we compare the size mismatch required to add Ch1 layers one on top of the other, with that required to add a Ch2 layer. The result confirms the usual rule that to change chirality it is required to add bigger atoms. In Fig. 3.16 we also have the calculations done for the Bergman series and the generalized anti-Mackay construction.

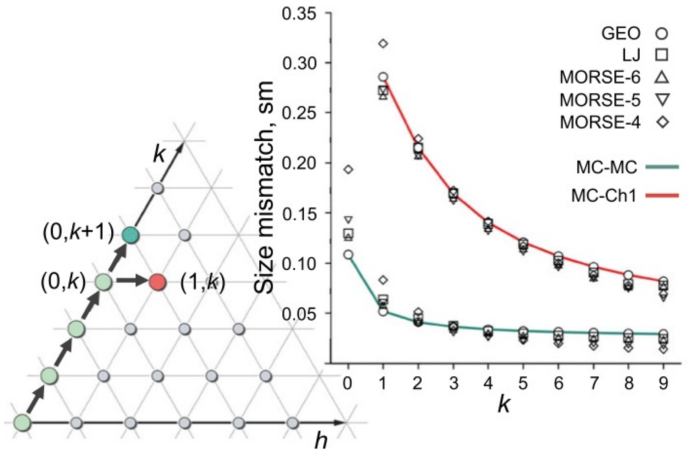

Fig. 3.13 Optimal size mismatch, calculated in various ways. GEO means that our formula based on theoretical considerations is used. LJ and MORSE mean that a potential either of the Lennard-Jones or of the Morse kind, with a different width of the potential well, is adopted: then the size of the newly added atoms is varied to find the value that gives the minimum potential energy. It is clear that our formula is in good agreement with the other results. Reproduced from Ref. [14]. Copyright 2025 Nature publishing group.

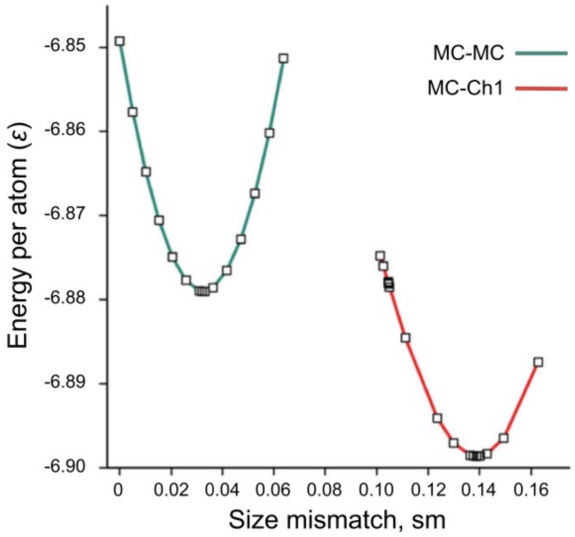

Fig. 3.14 Adding a sixth layer on a five-layer Mackay core (309 atoms including the central one) is different depending on wether the new layer is also Mackay (MC) or Ch1. In the first case the optimal size mismatch is very low (about 0.03) while in the second case the optimal size mismatch is about 0.14. In general, the potential energy increases very rapidly once the added atoms deviate from the optimal size. Here the energies are calculated by a LJ model, where the size of the atoms are encoded in the formula for the Lennard-Jones potential, where ε corresponds to the well depth of the pair interactions. Reproduced from Ref. [14]. Copyright 2025 Nature publishing group.

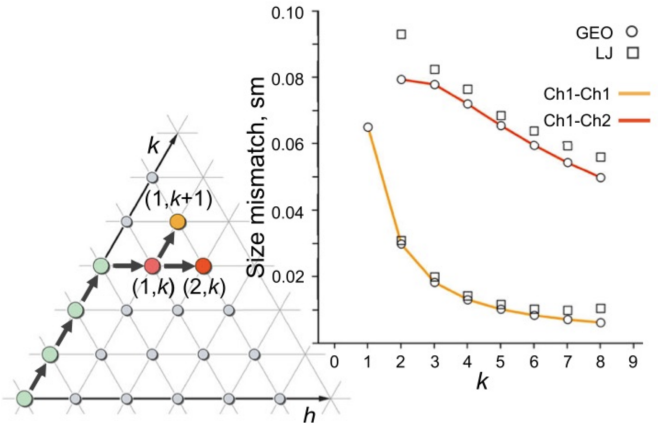

Fig. 3.15 It is easy to see that adding a Ch1 layer on another does not require a meaningful size mismatch, as opposed to adding a Ch2 layer. This can be seen also with LJ calculations, which here tend to give an even higher value for the size mismatch required. Reproduced from Ref. [14]. Copyright 2025 Nature publishing group.

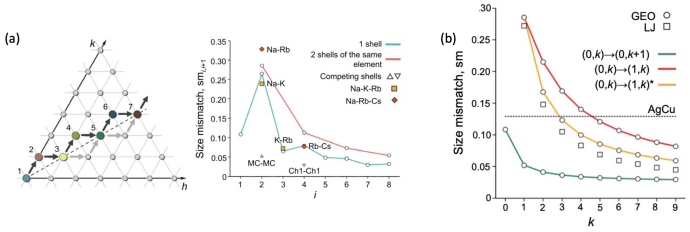

Fig. 3.16 (a) The Bergman series is recalled and the optimal size mismatch is calculated with our formula for both the choice of changing at each layer (blue line) and of changing every two layers (red line). The value for the systems Na-K-Rb and Na-Rb-Cs turned out to be compatible and the possibility to use them for building the designed icosahedral aggregates was verified in [14] with DFT calculations. (b) One can see that adding an anti-Mackay layer requires less size mismatch than adding a Ch1 one. In the case of the system Ag-Cu we verified this possibility with growth simulations, and the way it forces a sequence of growth of generalized anti-Mackay layers. Reproduced from Ref. [14]. Copyright 2025 Nature publishing group.

Chapter 4

Growth simulations

Based on the theory developed in Chapter 3 we now expose the results of growth simulations for different nanoalloys, meaning in particular bi-metallic systems with a transition metal (Ag or Au) in the shell and a core of a smaller size metal with more cohesive energy (we considered Ni, Co, Cu, Fe). This gives us a total of six core-shell systems: Ni@Ag, Co@Ag, Cu@Ag, Ni@Au, Co@Au and Fe@Au. Some of these results are not published in Ref. [14], where however other results are published which include growth simulations with alkali metals. For all these systems we specify the size mismatch and other characteristics in section 4.1 and then describe the performed MD simulations in section 4.2. We will mostly focus on the formation of Ch1 shells with multiple layers, but also show the generalized anti-Mackay sequence in the Cu@Ag system, and partly in the Co@Au and Fe@Au ones. For all the structures the layer-by-layer structure is shown. The images of the clusters always correspond to locally minimized structures, so that the effect of istantaneous vibrations is eliminated.

In section 4.3 the stability of some of these structures, with a Mackay core and a chiral shell, is also tested by making some heating simulations up to the melting temperature of the NPs. It is highlighted how this leaves the chiral configuration of these NPs intact up to the point where the shell melts.

In section 4.4 finally, the pressure characterization of the chiral NPs is made and compared with that of an entirely Mackay icosahedron realized with the same bi-metallic systems: it is shown how the chiral shells are much more stable. This is also shown by making exchanges of atoms between the shell and the core and registering the change in potential energy to see whether this could be a mechanism of transition to a different kind of structure.

NANOALLOY	sm	$E_{coh}(CORE)$	$E_{coh}(SHELL)$
Ni@Ag	0.161	4.44 (eV)	2.95 (eV)
Co@Ag	0.156	4.45	2.95
Cu@Ag	0.129	3.50	2.95
Ni@Au	0.156	4.44	3.81
Co@Au	0.152	4.45	3.81
Fe@Au	0.161	4.28	3.81

Table 4.1 Data for the size mismatches (sm) and the cohesive energies, both for the metal in the core ($E_{coh}(CORE)$) and for the metal in the shell ($E_{coh}(SHELL)$), according to the SMATB potentials employed.

4.1 Nanoalloys

Here in Table 4.1 all our six bi-metallic system are described in terms of size mismatch and cohesive energies, where these are important in that the element in the core is supposed to have a greater cohesive energy than that that goes in the shell. Eliminating this requirement would mean to rely on an entropic drive alone to the formation of a good structure, as would be the case of confined colloidal aggregates [66], but in our case inter-atomic forces are dominant instead of entropy. Working with noble metals as Ag and Au to form the shell, has the advantage that these do not tend very much to mix with the atoms in the core.

In Fig. 4.1 one can see that all our nanoalloys except Ag-Cu should permit the formation of Ch1 layers already with a Mackay core of 147-309 atoms, while in the case of Ag-Cu we will see that beginning with such a small Cu core is going to let us grow a generalized AM shell.

4.2 Growth simulations

4.2.1 Ag-Ni

For the Ag-Ni system, we performed the simulations reported in Table 4.2, with different initial cores and temperatures and deposition rates. For this system, which was the best in term of getting good chiral shells, the usual preference has been to work at 450 K of temperature and with a growth rate of 0.1 atom/ns. We also explored a wider range of temperatures and the growth rate turns out to be typically interchangeable with that of 1 atom/ns, also compatible with possible experimental setups.

In Fig. 4.2 and Fig. 4.3 are represented the two main results for the Ag-Ni system, meaning the possibility to grow Ch1 shells of an indefinite number of layers (here we went up to 4 layers on top of the core of 147 atoms). These images are given by taking the final

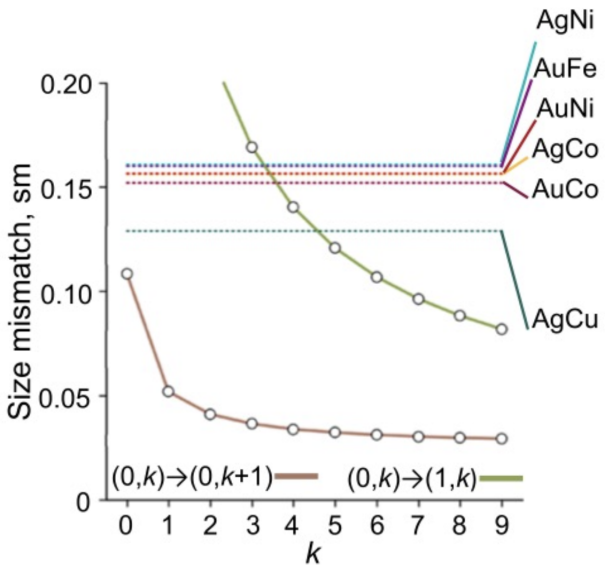

Fig. 4.1 Size mismatch of the different alloys considered. It is easy to see that Ag-Cu stands out for how low it is. As a consequence, this system requires a bigger Cu core in order to grow chiral layers on top of it. Reproduced from Ref. [14]. Copyright 2025 Nature publishing group.

CORE	TEMPERATURE	RATE	CHIRAL RESULT (yes/no)
Ni_{55}	300 K-500 K	0.1 atom/ns	no
$Ni_{55}Ag_{72}$	400 K/500 K	0.1/1 atom/ns	yes
Ni_{147}	400 K-600 K	0.1-1 atom/ns	yes
Ni_{309}	400 K-600 K	0.1-1 atom/ns	yes
Ni_{227}	450 K	0.1 atom/ns	yes
Ni_{289}	450 K	0.1 atom/ns	yes
Ni_{329}	450 K	0.1 atom/ns	yes

Table 4.2 Simulations performed for the Ag-Ni system. It is found as expected that, for Ni cores of 147 and 309 atoms, it was possible to grow chiral shells (Ch1). The simulations with Ni cores in between 147 and 309 atoms had the purpose to test the robustness of this growth pathway in a more realistic scenario.

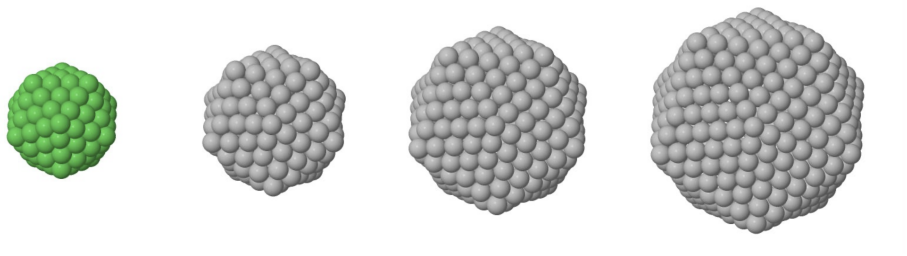

Fig. 4.2 Growth sequence realized by depositing Ag on Ni_{147} at T=450 K and with a rate of deposition of 0.1 atom/ns. Here we show the layers of the final result of our growth. In this case there was no exchange of atoms between the core and the shell; this is a somewhat atypically good result.

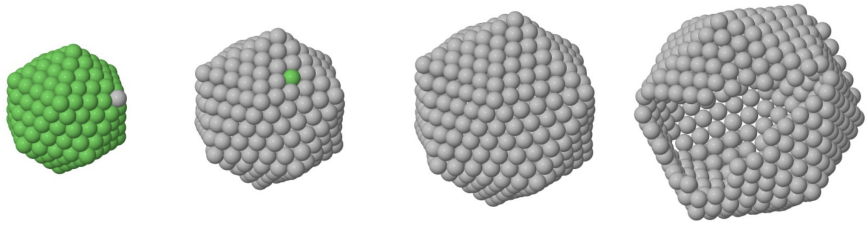

Fig. 4.3 Growth sequence realized by depositing Ag on Ni_{309} at T=450 K and with a rate of deposition of 1 atom/ns. Here we show the layers of the final result of our growth. In this case there was one exchange between the core and the shell.

results of the growth and separating the core and the added layers; had we represented all intermediate results of growth the visual would have been similar anyway, as the first layer already has to chiralize in order for the growth to follow that path.

The simulation with initial core Ni_{227} that is represented in Fig. 4.4 was done to test the possibility to realize a chiral growth even beginning with a non-perfect Mackay core: in this case the core has an incomplete external shell so that its size is in the middle between 147 and 309 atoms. This gives greater robustness to our computational results in that an experiment could never practically be done with a perfect core with a magic number of atoms. Similarly the case goes for the growth done beginning with Ni_{289} or Ni_{329}, and in fact typically our capability of mass-selecting NPs is on the order of 10%. These other two growth simulations are represented in Fig. 4.5 and Fig. 4.6. Of these three simulations only the first gives a shell without the usual magic numbers, in that the first chiral layer is also the last Mackay one; in the other two cases the atomic species that is in the minority gets coopted in the prevailing configuration.

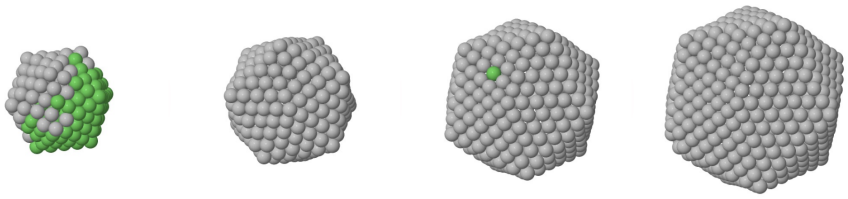

Fig. 4.4 Growth sequence realized by depositing Ag on Ni_{227} at T=450 K and with a rate of deposition of 0.1 atom/ns. Here we show the layers of the final result of our growth. It is interesting to see that in the initial part of the growth the Ag islands deposited on the incomplete Mackay core chiralizes while completing the layer, leaving the Ni atoms in a Mackay disposition. There is also a Ni atom that made its way to an higher part of the shell during the growth.

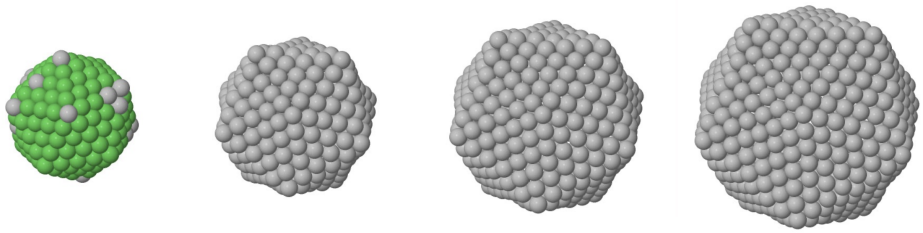

Fig. 4.5 Growth sequence realized by depositing Ag on Ni_{289} at T=450 K and with a rate of deposition of 0.1 atom/ns. Here we show the layers of the final result of our growth. In the initial part of the growth Ag atoms deposited on the incomplete Mackay core join the Ni atoms in a Mackay disposition.

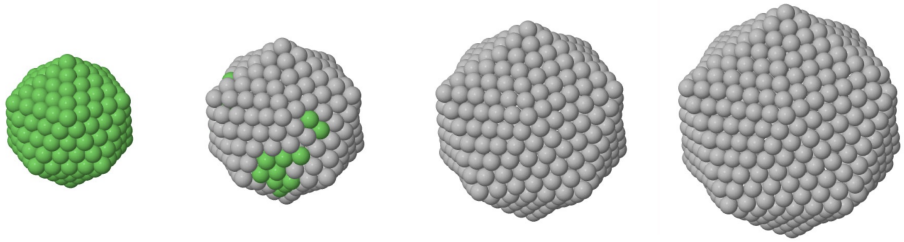

Fig. 4.6 Growth sequence realized by depositing Ag on Ni_{329} at T=450 K and with a rate of deposition of 0.1 atom/ns. Here we show the layers of the final result of our growth. In the first layer the 20 Ni atoms are co-opted in a chiral configuration together with the other newly deposited Ag atoms.

Structure	Temperature	Vacancies/adatoms	Exchanges
MC@Ch1@Ch1	400 K	53	0
MC@Ch1@Ch1	400 K	27	0
MC@Ch1@Ch1	450 K	35	1
MC@Ch1@Ch1	450 K	28	0
MC@Ch1@Ch1	500 K	45	0
MC@Ch1@Ch1	500 K	53	1
MC@Ch1@Ch1	550 K	8	2
MC@Ch1@Ch1	550 K	61	2
MC@Ch1@Ch1	600 K	many	4
MC@Ch1@Ch1	600 K	11	4
MC@Ch1@Ch1@Ch1	400 K	49	0
MC@Ch1@Ch1@Ch1	400 K	39	0
MC@Ch1@Ch1@Ch1	450 K	50	1
MC@Ch1@Ch1@Ch1	450 K	8	0
MC@Ch1@Ch1@Ch1	500 K	19	0
MC@Ch1@Ch1@Ch1	500 K	32	1
MC@Ch1@Ch1@Ch1	550 K	12	2
MC@Ch1@Ch1@Ch1	550 K	11	2
MC@Ch1@Ch1@Ch1	600 K	many	4
MC@Ch1@Ch1@Ch1	600 K	22	4

Table 4.3 Number of defects in growth simulations in which Ag atoms are deposited on a Mackay seed of 309 Ni atoms. Defects are counted when magic sizes are reached, corresponding to the completion of two Ch1 shells (833 atoms) and three Ch1 shells (1265 atoms). Vacancies are atoms missing from the most external Ch1 shell, corresponding to adatoms or small islands on top of it. Exchanges are Ni-Ag swaps occurring between the most external Mackay layer and the most internal Ch1 one. Reproduced from Ref. [14]. Copyright 2025 Nature publishing group.

The Ag-Ni system was probably the best one in order to grow a Ch1 shell, so we made a number of simulations on it in order to quantify the presence of defects in the growth process and to make a comparison with the Ag-Cu system, which was the most difficult to work with in order to get a Ch1 shell when starting on such relatively small cores. Such defects are either 'vacancies/adatoms', meaning the final result of a growth simulation has not the final layer completed, or 'exchanges', meaning the core lost some of its atoms to the shell and vice-versa. The results for Ag-Ni are collected in Table 4.3, and the overall picture is that of a very 'smooth' process of growth.

While this is not included in Table 4.2, we also performed a simulation of growth on a Ni core of 561 atoms and for the first layer obtained a configuration with square vertices that can be seen in Fig. 4.7 (a), but then by continuing the growth the cluster showed a transition to form chiral shells as in Fig. 4.7 (c). This was possible due to the high temperature (600 K)

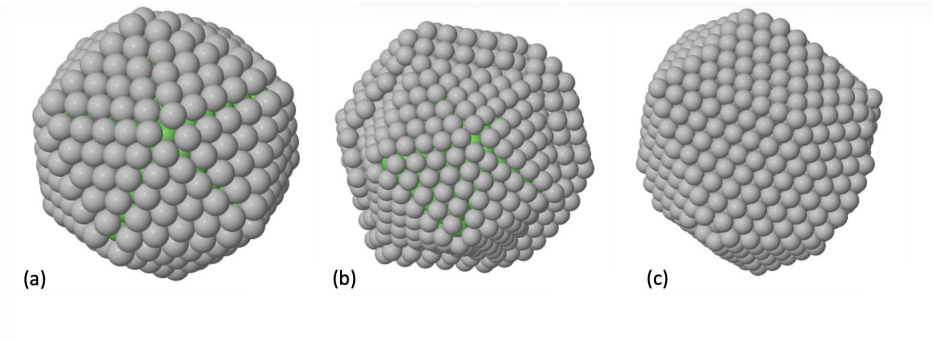

Fig. 4.7 Growth sequence realized by depositing Ag on Ni_{561} at T=600 K and with a rate of deposition of 0.1 atom/ns. Here we show the intermediate result of 846 atoms (a) and the final result at 1305 atoms, back (b) and front (c), of our growth simulations. Under the new Ch1 layers also the first Ag layer has chiralized accordingly.

CORE	TEMPERATURE	RATE	CHIRAL RESULT (yes/no)
Co_{55}	300 K-500 K	0.1 atom/ns	no
Co_{147}	350 K	0.1 atom/ns	yes
Co_{309}	450 K	0.1/1 atom/ns	yes

Table 4.4 Simulations performed for the Ag-Co system.

that, together with the 0.1 atom/ns growth rate, gave to part of the cluster the time to reach at least in part an energetically good configuration.

4.2.2 Ag-Co

Similar simulations were done for the Ag-Co system as shown in Table 4.4. These simulations showed that it was possible to grow a chiral shell beginning with a core of 147 or 309 atoms. In the case of an initial core of 147 atoms it was however only possible to do this when a lower temperature of 350 K was adopted.

Two growth sequence with the formation of a chiral shell are shown in Fig. 4.8 and Fig. 4.9. In both cases there were some exchanges, but the overall result was a clear Ch1 structure.

4.2.3 Ag-Cu

For the Ag-Cu system, which is the one with the lower size mismatch of those we considered, it was only possible to grow a chiral shell with a seed of 561 atoms as reported in Table 4.5.

This result is shown in Fig. 4.10 while the growth according to the generalized anti-Mackay sequence is shown in both Fig. 4.11 and Fig. 4.12 with a different kind of result. If this sequence begins with a Mackay core of 309 atoms it then results in a chiralization

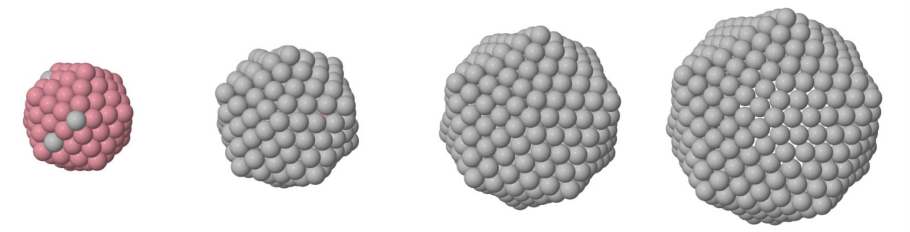

Fig. 4.8 Growth sequence realized by depositing Ag on Co_{147} at T=350 K and with a rate of deposition of 0.1 atom/ns. Here we show the layers of the final result of our growth, which in this case only was prosecuted up to three chiral layers. In this case there were three exchanges between the core and the shell.

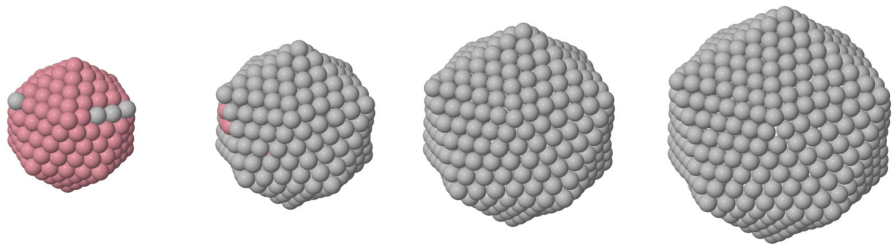

Fig. 4.9 Growth sequence realized by depositing Ag on Co_{309} at T=450 K and with a rate of deposition of 0.1 atom/ns. Here we show the layers of the final result of our growth. In this case there were five exchanges between the core and the shell.

CORE	TEMPERATURE	RATE	CHIRAL RESULT (yes/no)
Cu_{147}	450 K	0.1 atom/ns	no
Cu_{309}	450 K	0.1 atom/ns	yes
Cu_{561}	350 K-550 K	0.1/1 atom/ns	yes

Table 4.5 Simulations performed for the Ag-Cu system.

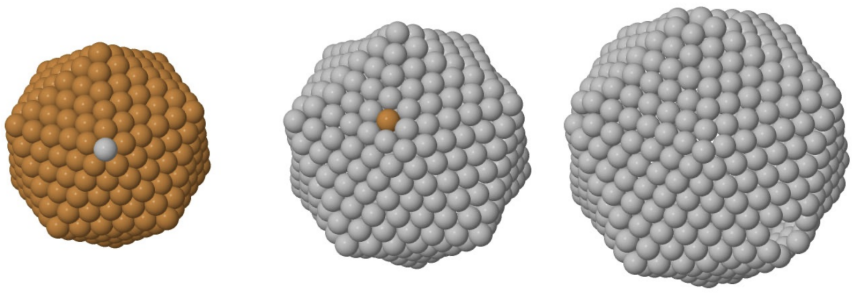

Fig. 4.10 Growth sequence realized by depositing Ag on Cu_{561} at T=400 K and with a rate of deposition of 1 atom/ns. Here we show the layers of the final result of our growth. In this case there was just one exchange between the core and the shell.

prior than reaching the Bergman layer, while this is not possible with an initial seed of 147 atoms: for this reason in Fig. 4.11 the two anti-Mackay layers and the final Bergman layer are shown while in Fig. 4.12 the last image is that of a chiral shell, where of course also all of the underlying Ag layers have undergone chiralization.

With regard to the growth of a chiral shell on a 561 Cu core, in Table 4.6 various simulations are reported with their growth defects. In a comparison with Table 4.3, it is particularly noteworthy the higher number of core-shell exchanges.

It can in general be seen in our simulations, and according to our theory [14], that once a Ch1 shell has taken as the resulting configuration during growth it will continue to grow

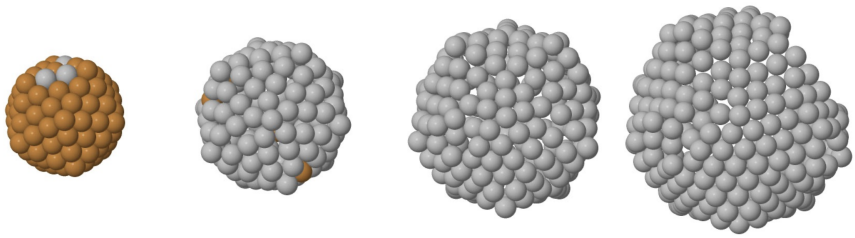

Fig. 4.11 Growth sequence realized by depositing Ag on Cu_{147} at T=350 K and with a rate of deposition of 1 atom/ns. Here we show the layers of the final result of our growth. In this case there were four exchanges between the core and the shell.

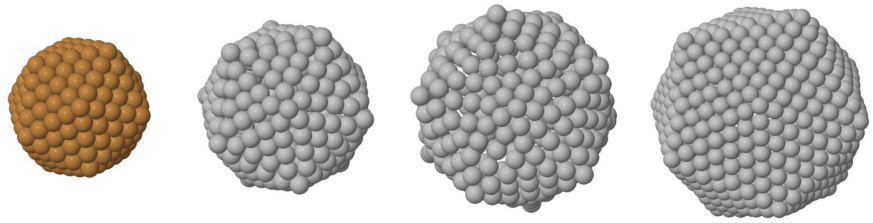

Fig. 4.12 Growth sequence realized by depositing Ag on Cu_{309} at T=350 K and with a rate of deposition of 1 atom/ns. Here we show the layers of the final result of our growth prior than chiralization and then the chiralized final result. In this case there were no exchanges between the core and the shell.

Structure	Temperature	Vacancies/adatoms	Exchanges
MC@Ch1@Ch1	350 K	3	1
MC@Ch1@Ch1	350 K	5	2
MC@Ch1@Ch1	400 K	5	2
MC@Ch1@Ch1	400 K	8	1
MC@Ch1@Ch1	450 K	8	3
MC@Ch1@Ch1	450 K	8	3
MC@Ch1@Ch1	500 K	5	9
MC@Ch1@Ch1	500 K	11	5
MC@Ch1@Ch1	550 K	7	12
MC@Ch1@Ch1	550 K	5	13
MC@Ch1@Ch1@Ch1	350 K	23	1
MC@Ch1@Ch1@Ch1	350 K	39	2
MC@Ch1@Ch1@Ch1	400 K	22	3
MC@Ch1@Ch1@Ch1	400 K	19	1
MC@Ch1@Ch1@Ch1	450 K	38	3
MC@Ch1@Ch1@Ch1	450 K	13	13
MC@Ch1@Ch1@Ch1	500 K	50	9
MC@Ch1@Ch1@Ch1	500 K	40	5
MC@Ch1@Ch1@Ch1	550 K	29	12
MC@Ch1@Ch1@Ch1	550 K	40	12

Table 4.6 Number of defects in growth simulations in which Ag atoms are deposited on a Mackay seed of 561 Cu atoms. Defects are counted when magic sizes are reached, corresponding to the completion of one Ch1 shell (873 atoms) and two Ch1 shells (1305 atoms). Vacancies are atoms missing from the most external Ch1 shell, corresponding to adatoms or small islands on top of it. Exchanges are Cu-Ag swaps occurring between the most external Mackay layer and the most internal Ch1 one. Reproduced from Ref. [14]. Copyright 2025 Nature publishing group.

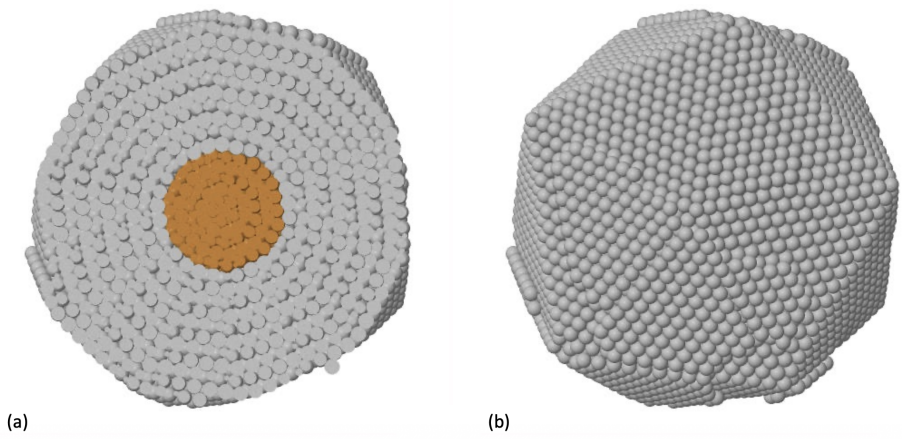

Fig. 4.13 Cluster of 12262 atoms obtained by depositing Ag on Cu_{561} at T=450 K and with a rate of deposition of 0.1 atom/ns initially and then of 1 atom/ns. (a) Interior view; while it cannot be seen here, there are seven exchanges between the core and the shell. (b) Surface view; there are ten Ch1 layers in total.

without change. In the specific case of the Ag-Cu system we continued to the growth on a Cu core of 561 atoms up to a cluster of 12262 atoms, which is shown in Fig. 4.13 with both surface and interior view.

4.2.4 Au-Ni

We now turn to the Au-Ni system, which, despite a quite high size mismatch, similar to that for the Ag-Ni system, nonetheless proved more difficult to grow a chiral shell with. In Table 4.7 the results are reported, and in Fig. 4.14 the successful growth of a Ch1 shell on a core of 561 atoms is shown and so in Fig. 4.15 for a core of 309 atoms, while in Fig. 4.16 a failed attempt made on a core of 309 atoms is shown instead. This last result has some similarity with what has already been seen with MD simulations in Ref. [74, 75], due to the general tendency of Au to have highly strained surfaces: in both cases one can have an unstable anti-Mackay growth with the accumulation of atoms on opposite sides of the NP. The results in Ref. [74, 75] are for the Au-Cu system, which we did not consider here but also shows some instances of chiral development.

4.2.5 Au-Co

In Table 4.8 the simulations for the Au-Co system are reported, and the positive result obtained by growing on a core of 309 atoms is shown in Fig. 4.17. There was a very high

CORE	TEMPERATURE	RATE	CHIRAL RESULT (yes/no)
Ni_{147}	450 K	0.1 atom/ns	no
Ni_{309}	400 K	0.1 atom/ns	yes/no
Ni_{561}	400 K/500 K	0.1/1 atom/ns	yes

Table 4.7 Simulations done for the Au-Ni system.

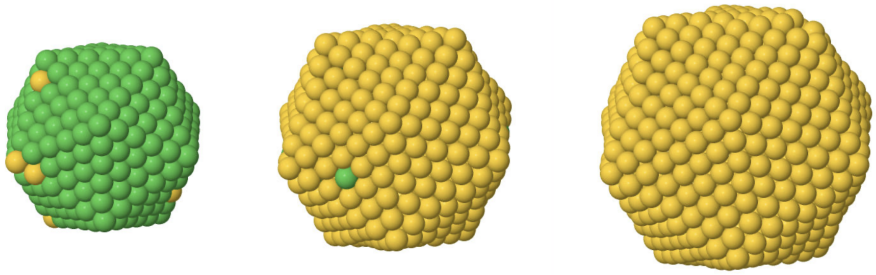

Fig. 4.14 Growth sequence realized by depositing Au on Ni_{561} at T=400 K and with a rate of deposition of 0.1 atom/ns. Here we show the layers of the final result of our growth. In this case there were six exchanges between the core and the shell.

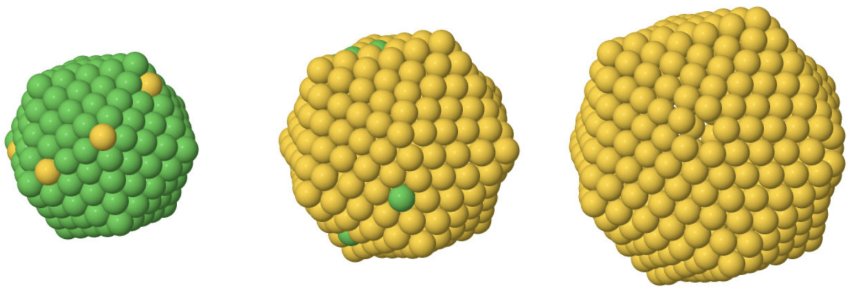

Fig. 4.15 Growth sequence realized by depositing Au on Ni_{309} at T=400 K and with a rate of deposition of 0.1 atom/ns. Here we show the layers of the final result of our growth. In this case there were six exchanges between the core and the shell.

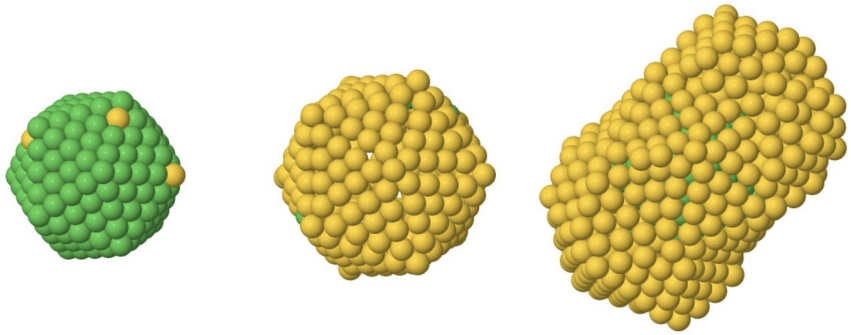

Fig. 4.16 Growth sequence realized by depositing Au on Ni_{309} at T=400 K and with a rate of deposition of 0.1 atom/ns. Here we show the layers of the final result of our growth. In this case there were three exchanges between the core and the shell. It can be seen that while initially there is the formation of an anti-Mackay layer, then the growth doesn't proceed smoothly but leads instead to the formation of two big 'islands'

CORE	TEMPERATURE	RATE	CHIRAL RESULT (yes/no)
Co_{55}	450 K	0.1 atom/ns	no
Co_{147}	450 K	0.1 atom/ns	no
Co_{309}	450 K	0.1 atom/ns	yes

Table 4.8 Simulations performed for the Au-Co system.

number of exchanges, which is part of the reason why working with Au proved more difficult than working with Ag when growing core-shell NPs, another being the tendency of Au to re-construct surfaces [74, 75] and form rosettes as already described in Chapter 1. In Fig. 4.18 we also show the very particular result we obtained of a Mackay bi-metallic icosahedron, which was not expected because of the noticeable size mismatch.

4.2.6 Au-Fe

As reported in Table 4.9, the growth of a Ch1 shell proved possible in the Au-Fe system beginning with a core of at least 309 atoms, and one such growth sequence is shown in Fig. 4.19. In some cases chiral growth was obtained even with a core of 147 atoms as in Fig. 4.20, but a different non-chiral result was also observed which is shown in Fig. 4.21. Differently than what expected, it was not possible to grow a Ch1 shell on a core of 561 atoms, while an anti-Mackay arrangement was obtained instead, as shown in Fig. 4.22. With regard to the growth sequence on a core of 309 atoms, many simulations were done at different temperatures, to collect data on growth defects, reported in Table 4.10 similarly to what was done for the Ag-Ni and Ag-Cu systems; the results for core-shell exchanges are quite similar

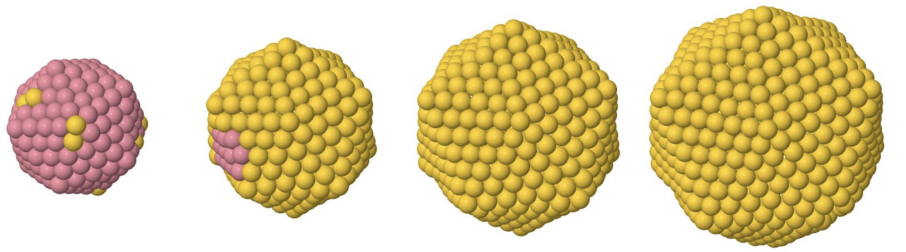

Fig. 4.17 Growth sequence realized by depositing Au on Co_{309} at T=450 K and with a rate of deposition of 0.1 atom/ns. Here we show the layers of the final result of our growth. In this case there were eleven exchanges between the core and the shell.

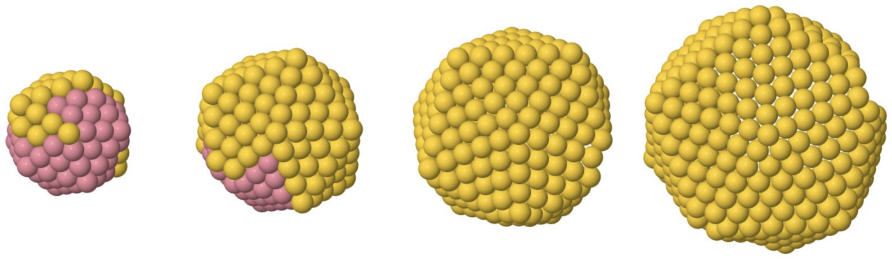

Fig. 4.18 Growth sequence realized by depositing Au on Co_{147} at T=450 K and with a rate of deposition of 0.1 atom/ns. Here we show the layers of the final result of our growth. In this case there were many exchanges between the core and the shell and as a consequence a Mackay icosahedron with two layers of mixed composition was formed.

CORE	TEMPERATURE	RATE	CHIRAL RESULT (yes/no)
Fe_{147}	300 K/500 K	1 atom/ns	yes/no
Fe_{309}	400 K-600 K	1 atom/ns	yes
Fe_{561}	400 K	1 atom/ns	no

Table 4.9 Simulations performed for the Au-Fe system.

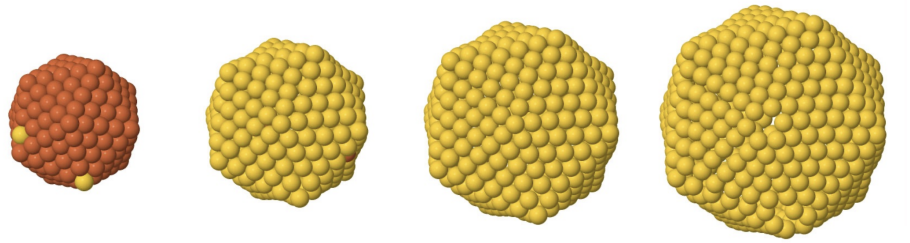

Fig. 4.19 Growth sequence realized by depositing Au on Fe_{309} at T=450 K and with a rate of deposition of 1 atom/ns. Here we show the layers of the final result of our growth. In this case there were four exchanges between the core and the shell. It is possible to see a rosette of six atoms at the center of the last layer, which is often found in Au NPs.

to those for Ag-Cu despite the higher size mismatch, showing again the different properties of Au.

4.3 Heating simulations

In order to test the stability of these core-shell NPs with a Ch1 shell, we decided to simulate an accelerated heating of the structure by giving to the MD simulations of evolution a temperature ramp of 1 K/ns, meaning each nanosecond the temperature increases by a Kelvin degree. Considering that we have for the collision frequency of our thermostat a value of $5 \cdot 10^{11}$ s^{-1} [14, 47], this is enough to have the changed temperature to influence the

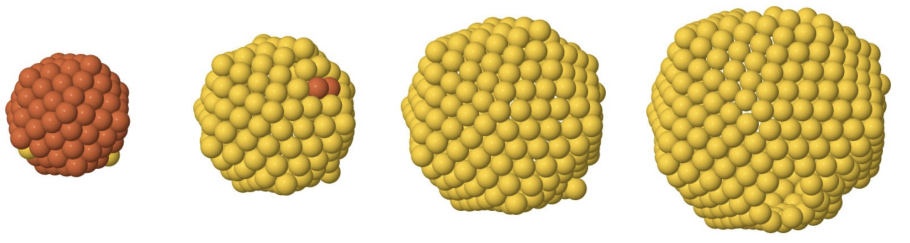

Fig. 4.20 Growth sequence realized by depositing Au on Fe_{147} at T=300 K and with a rate of deposition of 1 atom/ns. Here we show the layers of the final result of our growth. In this case there were two exchanges between the core and the shell.

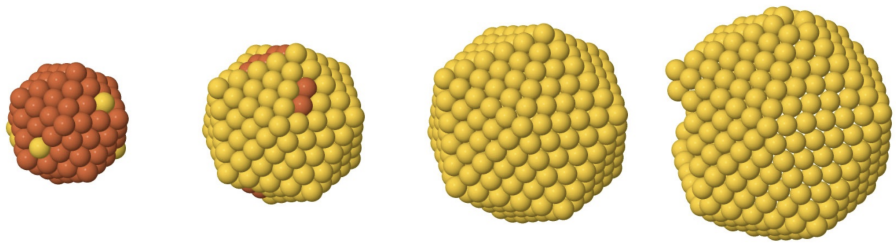

Fig. 4.21 Growth sequence realized by depositing Au on Fe_{147} at T=500 K and with a rate of deposition of 1 atom/ns. Here we show the layers of the final result of our growth. In this case there were nine exchanges between the core and the shell, also due to the high temperature, and a Mackay icosahedron formed. Differently than what seen in Fig 4.18, the exchanges are not so many that the last layer of the core can be said to be of mixed composition.

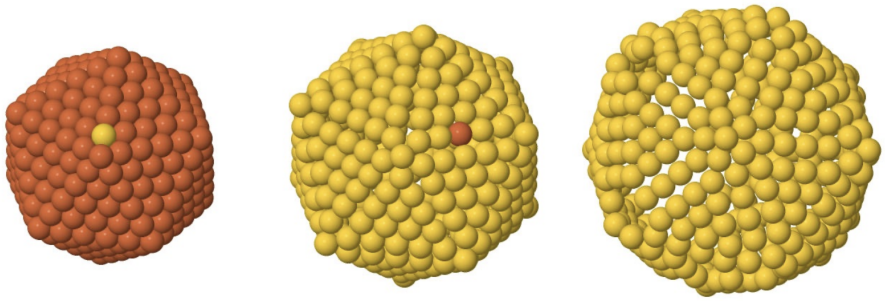

Fig. 4.22 Growth sequence realized by depositing Au on Fe_{561} at T=400 K and with a rate of deposition of 1 atom/ns. Here we show the layers of the final result of our growth. In this case there was just one exchange between the core and the shell. The generalized anti-Mackay sequence is perhaps due to the fact that with a larger core the atoms would have needed more time to arrange in a chiral way.

Structure	Temperature	Vacancies/adatoms	Exchanges
MC@Ch1@Ch1@Ch1	400 K	50	3
MC@Ch1@Ch1@Ch1	450 K	37	4
MC@Ch1@Ch1@Ch1	500 K	35	4
MC@Ch1@Ch1@Ch1	550 K	41	10
MC@Ch1@Ch1@Ch1	600 K	52	8

Table 4.10 Number of defect in simulations of growth on a Fe Mackay core of 309 atoms. All the exchanges are between the last MC and the first Ch1 layers. The results can be compared to both 4.3 and 4.6 highlighting the higher number of both exchanges and vacancies/adatoms

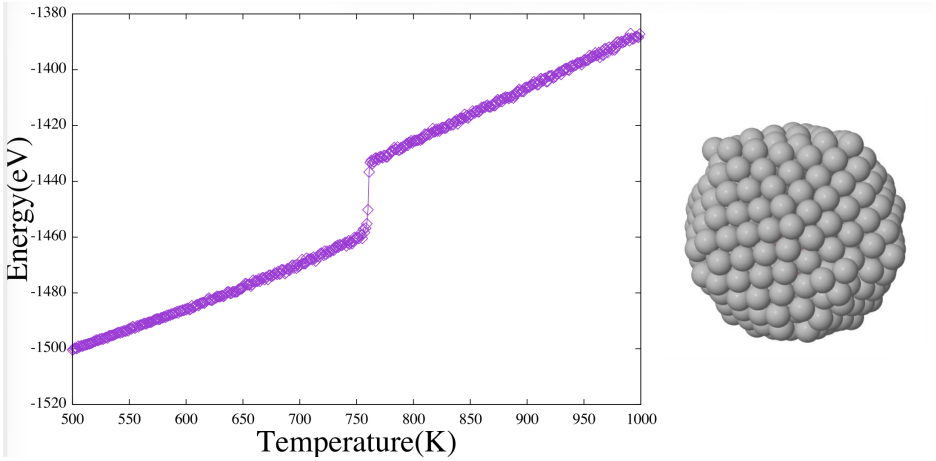

Fig. 4.23 Caloric curve for the heating of $Ag_{344}Co_{147}$. It is possible to see a surface view of the cluster prior to the melting point, showing the Ch1 arrangement intact.

dynamic evolution. We are interested in seeing whether the Ch1 configuration of the shell is to remain unchanged up to the melting point. The melting temperature of metal NPs is indeed a non-scalable property [3] meaning it is not the same as for the bulk metal, as the higher surface-to-volume ratio facilitates the transition to a liquid. Since the NPs we consider here have a radius radius of 1-2 nanometers, we expects a much lower melting temperature than for the bulk metal according to Pawlow's law [21, 76] and also depending on the shape [77].

It is important to consider that the melting temperature of the metal in the core is higher because of the greater cohesive energy, so that in the case of Ag-Ni we were able to find two phase transitions as opposed to one, also because of the low melting temperature of Ag (1235K for the bulk material). Moreover because of the fluctuations, that correlate with the inverse square root of the number of atoms, particularly for small clusters the phase transitions do not occur starkly at one temperature.

We present here the plots of the temperature and the potential energy for the clusters we considered, which have Ag in the shell except for one case, and we show an image of the cluster prior than melting but near the melting temperature, with the Ch1 configuration of the surface intact. In Figs. 4.24, 4.25, 4.26, 4.30 the cluster we considered was one that it was possible for us to grow, while in Figs. 4.23, 4.27, 4.28, 4.29 it was simply built by a program based on the generalized Caspar-Klug method.

It is easy to see that the cluster always remains intact up to the transition to a liquid phase, which highlights the stability of this kind of structure. Though we mostly considered nanoalloys with Ag in the shell, it is worth noting that in Fig. 4.27 the Au-Co NP we considered, which is one we built, was pretty stable as well, meaning the same probably

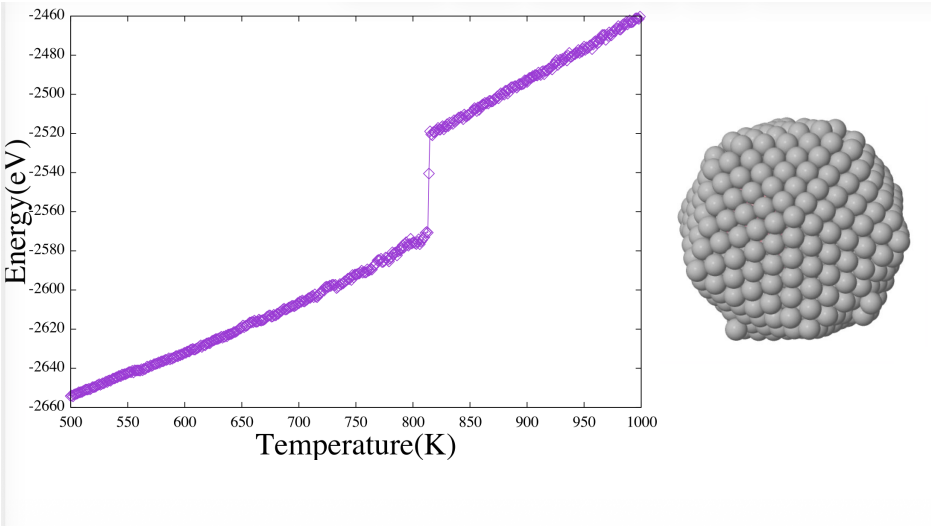

Fig. 4.24 Caloric curve for the heating of $Ag_{524}Co_{309}$. It is possible to see a surface view of the cluster prior to the melting point, showing the Ch1 arrangement intact.

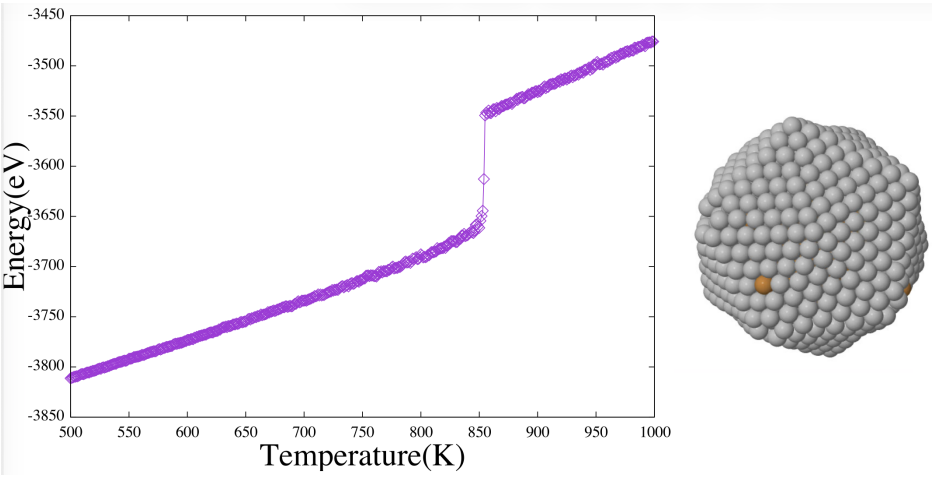

Fig. 4.25 Caloric curve for the heating of $Ag_{744}Cu_{561}$. It is possible to see a surface view of the cluster prior to the melting point, showing the Ch1 arrangement intact.

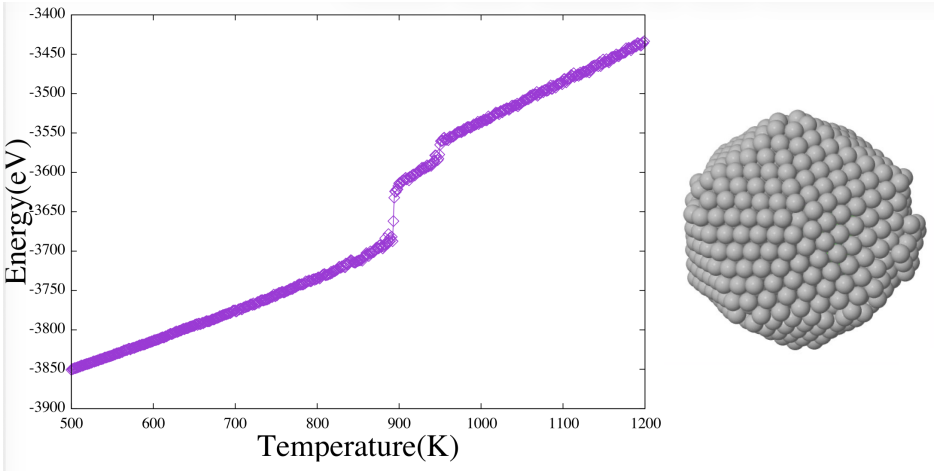

Fig. 4.26 Caloric curve for the heating of $Ag_{956}Ni_{309}$. It is possible to see a surface view of the cluster prior to the melting point, showing the Ch1 arrangement intact. Here there are two different transitions, for the shell (the one that most concerns us) and then for the core.

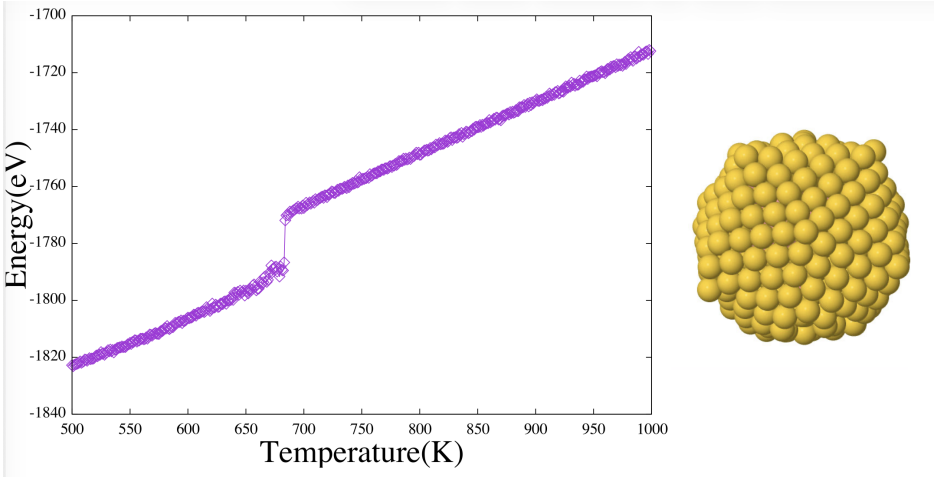

Fig. 4.27 Caloric curve for the heating of $Au_{344}Co_{147}$. It is possible to see a surface view of the cluster prior to the melting point, showing the Ch1 arrangement intact.

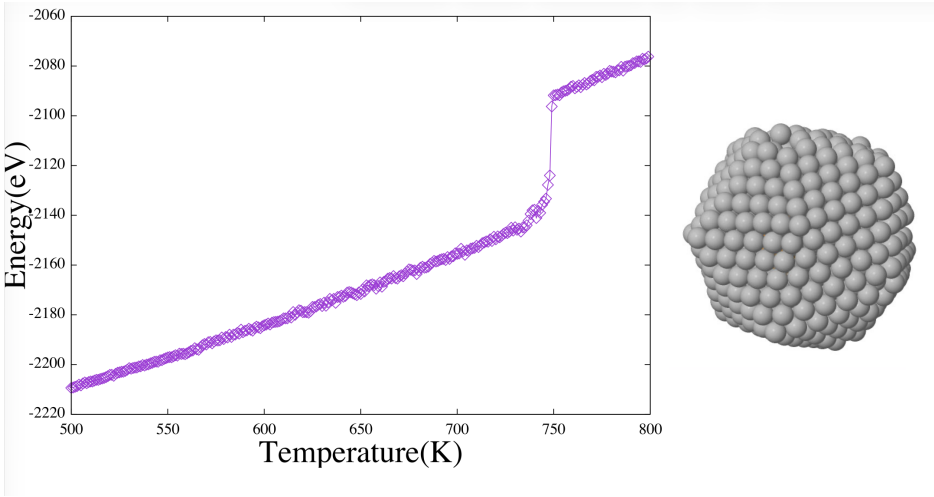

Fig. 4.28 Caloric curve for the heating of $Ag_{656}Cu_{147}$. It is possible to see a surface view of the cluster prior to the melting point, showing the Ch1 arrangement intact.

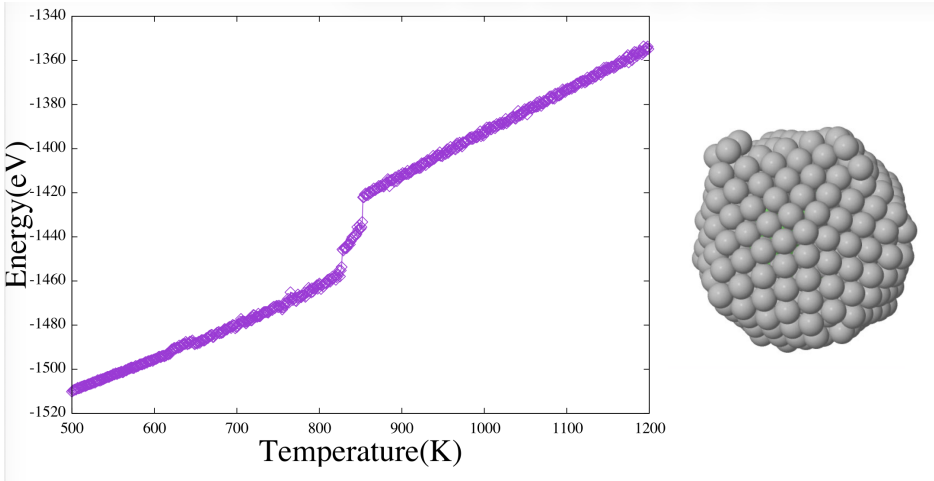

Fig. 4.29 Caloric curve for the heating of $Ag_{344}Ni_{147}$. It is possible to see a surface view of the cluster prior to the melting point, showing the Ch1 arrangement intact. Here there are two different transitions, for the shell (the one that most concerns us) and then for the core.

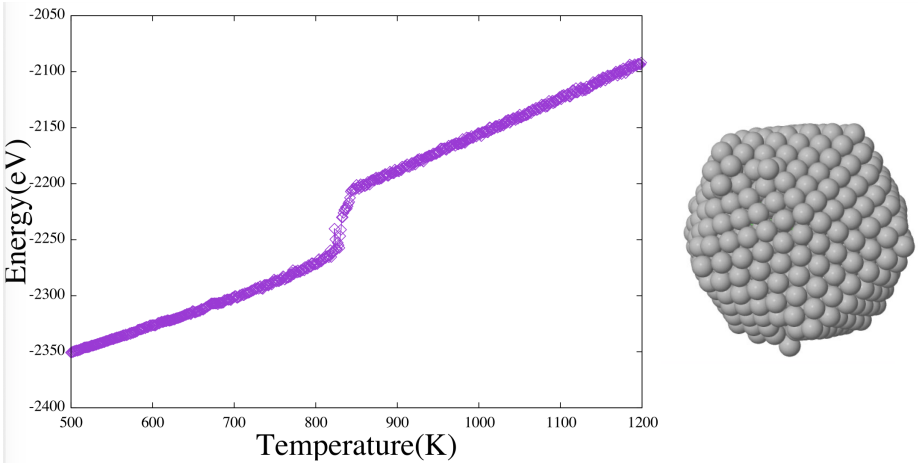

Fig. 4.30 Caloric curve for the heating of $Ag_{656}Ni_{147}$. It is possible to see a surface view of the cluster prior to the melting point, showing the Ch1 arrangement intact. Here there are two different transitions, albeit not very distant, for the shell (the one that most concerns us) and then for the core.

would hold for an even more stable NP, such as one grown according to our selection rules for the size mismatch and the initial core.

4.4 Stability and pressure analysis

Apart from performing heating simulations, our main test of stability of these icosahedral aggregates was that of making atomic exchanges between the core and the shell. We then evaluated the change in potential energy of the structure, as one can see in Fig. 4.31 for the specific case of alkali metals and with the use of DFT calculations. For all the nanoalloys we considered in our growth simulations, except Au-Fe, we made the same test of stability, always taking a perfect icosahedral structure built by us with initially no exchanges between core and shell. These data are reported in Table 4.11, and they confirm the tendency of chiral structures to be much more stable than Mackay ones, for nanoalloys obeying the selection rules we found.

The general rule being that swapping atoms brings an advantage in term of lower potential energy for the Mackay shells, while a disadvantage in case of a chiral shell, there are however some cases in Table 4.11 where there also is an energetic cost in the case of a Mackay shell. Moreover there are differences due to the specific nanoalloy: Ni@Au was the one associated with the lower stability, meaning a lower energetic cost for swapping atoms with a chiral shell, and a larger gain in the case of a Mackay shell; Co@Ag was the most stable instead, followed by Ni@Ag, Co@Au and then Cu@Ag.

As already seen in Chapter 2 negative pressure corresponds to tensile strain meaning that a larger atom would better fit, while the opposites holds for positive pressure. So we made the difference between the pressure total on the most internal shell layer and that on the most external core layer, which is reported in Table 4.12. This indicates a much stronger tendency for the Mackay icosahedron toward the swapping of atoms, since the smaller atoms in the core are lead to take their place in the shell. The data for the various nanoalloys confirm the findings from Table 4.11 as for the greater instability of Ni@Au, which has the greater pressure differentials indeed; aside from that the greater stability of Co@Ag and Cu@Ag also is confirmed. Since however the meaning of these differentials is better understood by mapping and representing the pressure on all the atoms, we show in Figs. 4.32, 4.33, 4.34, 4.35, 4.36 and 4.37 how that is for some of the considered NPs.

In particular, in all these images we considered the nanoalloys Ni@Ag, Co@Ag and Co@Au, with a core of 309 atoms and two layers either of a Mackay or of a Ch1 type on top of it. These pressure analysis shows, as Table 4.12 does, that the all Mackay aggregate suffers from greater instability, while it is true that in general there is some pressure differential that could favor core-shell exchanges also when the shell is chiral. We show in Fig. 4.38 a global optimization search that corroborates the finding of instability of the all Mackay configuration for these NPs.

Another relevant finding is the high strain in the case of a chiral surface which could have catalytic applications [78] and in general, but particularly for chiral NPs, the high pressure on the atom at the center. This could make it a good idea, also in term of possible applications, to study the case of a hollow NP [79].

4.5 Conclusions

The theory developed in Chapter 3 is validated by our MD simulations of growth in a way that could open the road to experimental findings by gas phase condensation with Ag and Au on a suitable metallic core. Other similar results have been presented in Ref. [14] and more could be found by selecting nanoalloys according to our rules.

Both heating simulations and tests of core-shell exchanges confirm the stability of the chiral multi-layer structures we found, and so does the pressure analysis. Apart from the catalytic properties of a strained surface and possible optical applications, a shell of many chiral layers could also have the advantage of better protecting the Mackay core, preventing e.g. oxidation during a chemical reaction, or in a situation where the magnetic properties of the core are needed.

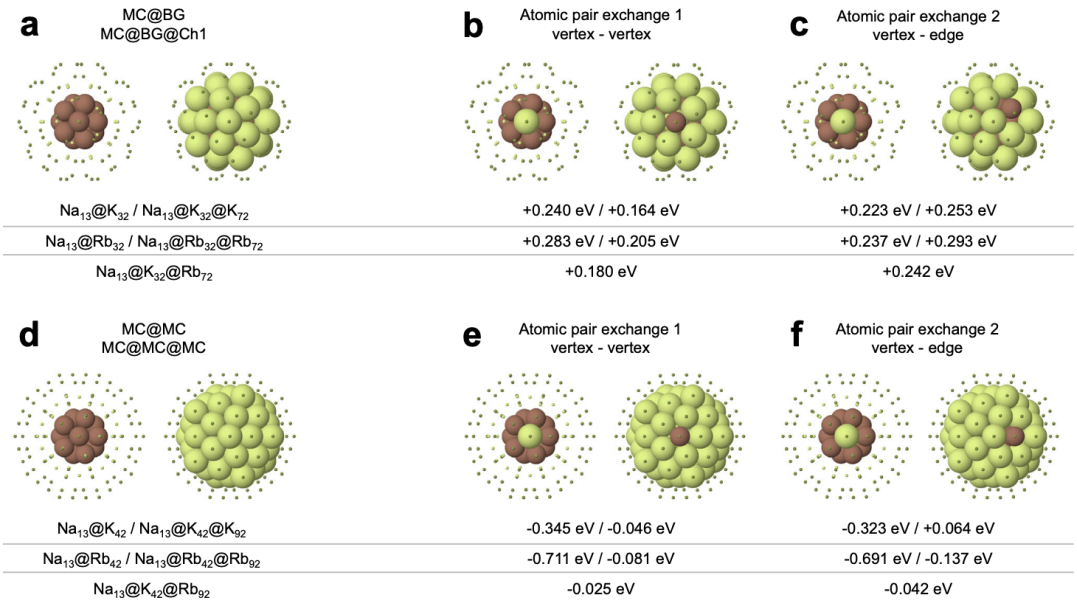

Fig. 4.31 Test of atomic exchanges for the Na@K, Na@Rb and Na@K@Rb nanoalloys. Perfect structures before the atomic pair exchange, either of (a) MC@BG/MC@BG@Ch1 or (d) MC@MC/MC@MC@MC type. Atoms in the second and third shells are colored in brown and yellow, respectively. b, c, e, f configurations after the atomic pair exchanges of two -0.025 eV -0.042 eV different types. Energy differences with respect to the perfect configurations in (a) and (d) are reported below. Positive and negative energy differences indicate unfavourable and favourable exchange processes, respectively. Reproduced from Ref. [14]. Copyright 2025 Nature publishing group.

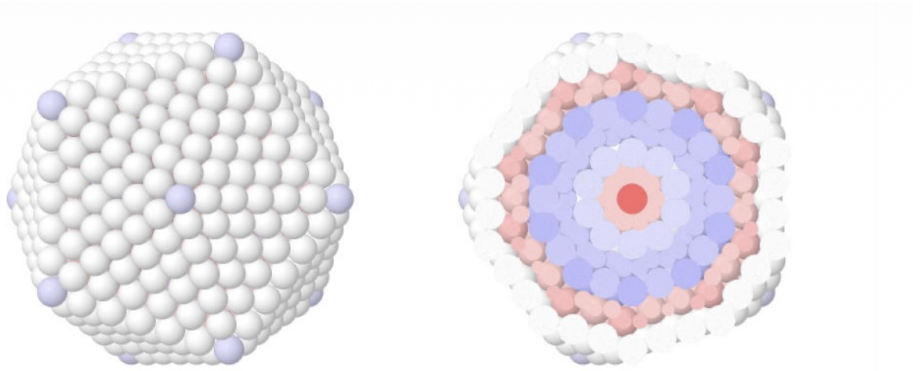

Fig. 4.32 Pressure map of $Ag_{614}Ni_{309}$. Surface and interior view. There is a sharp pressure change between the strained core and the compressed first layer of Ag.

Layers	Chiral/Mackay	$\Delta E(CH)$ (eV)	$\Delta E(MC)$ (eV)
6/4	$Ag_{344}Ni_{147}/Ag_{414}Ni_{147}$	0.59	-0.17
6/4	$Ag_{344}Co_{147}/Ag_{414}Co_{147}$	0.69	-0.01
6/4	$Ag_{344}Cu_{147}/Ag_{414}Cu_{147}$	0.38	-0.09
6/4	$Au_{344}Ni_{147}/Au_{414}Ni_{147}$	0.18	-0.54
6/4	$Au_{344}Co_{147}/Au_{414}Co_{147}$	0.65	0.05
7/4	$Ag_{656}Ni_{147}/Ag_{776}Ni_{147}$	0.73	-0.05
7/4	$Ag_{656}Co_{147}/Ag_{776}Co_{147}$	0.91	0.15
7/4	$Ag_{656}Cu_{147}/Ag_{776}Cu_{147}$	0.46	-0.05
7/4	$Au_{656}Ni_{147}/Au_{776}Ni_{147}$	0.27	-0.45
7/4	$Au_{656}Co_{147}/Au_{776}Co_{147}$	0.64	0.06
7/5	$Ag_{524}Ni_{309}/Ag_{614}Ni_{309}$	0.51	-0.30
7/5	$Ag_{524}Co_{309}/Ag_{614}Co_{309}$	0.51	0.27
7/5	$Ag_{524}Cu_{309}/Ag_{614}Cu_{309}$	0.29	-0.15
7/5	$Au_{524}Ni_{309}/Au_{614}Ni_{309}$	0.02	-0.59
7/5	$Au_{524}Co_{309}/Au_{614}Co_{309}$	0.56	-0.03
8/4	$Ag_{1088}Ni_{147}/Ag_{1268}Ni_{147}$	0.75	-0.07
8/4	$Ag_{1088}Co_{147}/Ag_{1268}Co_{147}$	0.92	0.13
8/4	$Ag_{1088}Cu_{147}/Ag_{1268}Cu_{147}$	0.49	-0.06
8/4	$Au_{1088}Ni_{147}/Au_{1268}Ni_{147}$	0.30	-0.45
8/4	$Au_{1088}Co_{147}/Au_{1268}Co_{147}$	0.69	0.07
8/5	$Ag_{956}Ni_{309}/Ag_{1106}Ni_{309}$	0.62	-0.07
8/5	$Ag_{956}Co_{309}/Ag_{1106}Co_{309}$	0.69	-0.08
8/5	$Ag_{956}Cu_{309}/Ag_{1106}Cu_{309}$	0.41	-0.10
8/5	$Au_{956}Ni_{309}/Au_{1106}Ni_{309}$	0.18	-0.48
8/5	$Au_{956}Co_{309}/Au_{1106}Co_{309}$	0.56	0.04

Table 4.11 The number of layers is that of all the NP and of the core respectively. The energy differences refers to the situation before and after an atom in the most external layer of the core is 'swapped' with one in the most internal layer of the core. As for the case of Fig. 4.31, we exchanged vertices, and positive and negative energy differences indicate unfavourable and favourable exchange processes, respectively. We see very well that in the case of an all Mackay aggregate this tends to be a favourable exchange process, while the opposite holds for a chiral shell on a Mackay core.

Layers	Chiral/Mackay	$\Delta P(CH)$ (GPa)	$\Delta P(MC)$ (GPa)
6/4	$Ag_{344}Ni_{147}/Ag_{414}Ni_{147}$	3.32	16.43
6/4	$Ag_{344}Co_{147}/Ag_{414}Co_{147}$	2.05	14.81
6/4	$Ag_{344}Cu_{147}/Ag_{414}Cu_{147}$	0.69	13.59
6/4	$Au_{344}Ni_{147}/Au_{414}Ni_{147}$	9.93	24.39
6/4	$Au_{344}Co_{147}/Au_{414}Co_{147}$	6.75	20.57
7/4	$Ag_{656}Ni_{147}/Ag_{776}Ni_{147}$	1.59	14.57
7/4	$Ag_{656}Co_{147}/Ag_{776}Co_{147}$	-0.12	13.05
7/4	$Ag_{656}Cu_{147}/Ag_{776}Cu_{147}$	-1.16	11.79
7/4	$Au_{656}Ni_{147}/Au_{776}Ni_{147}$	3.59	19.54
7/4	$Au_{656}Co_{147}/Au_{776}Co_{147}$	0.51	15.69
7/5	$Ag_{524}Ni_{309}/Ag_{614}Ni_{309}$	7.54	16.61
7/5	$Ag_{524}Co_{309}/Ag_{614}Co_{309}$	5.92	15.35
7/5	$Ag_{524}Cu_{309}/Ag_{614}Cu_{309}$	4.01	13.84
7/5	$Au_{524}Ni_{309}/Au_{614}Ni_{309}$	13.79	23.41
7/5	$Au_{524}Co_{309}/Au_{614}Co_{309}$	10.01	20.34
8/4	$Ag_{1088}Ni_{147}/Ag_{1268}Ni_{147}$	2.04	14.91
8/4	$Ag_{1088}Co_{147}/Ag_{1268}Co_{147}$	0.28	13.33
8/4	$Ag_{1088}Cu_{147}/Ag_{1268}Cu_{147}$	-0.75	12.07
8/4	$Au_{1088}Ni_{147}/Au_{1268}Ni_{147}$	5.53	20.29
8/4	$Au_{1088}Co_{147}/Au_{1268}Co_{147}$	1.82	16.71
8/5	$Ag_{956}Ni_{309}/Ag_{1106}Ni_{309}$	5.91	14.81
8/5	$Ag_{956}Co_{309}/Ag_{1106}Co_{309}$	3.96	13.63
8/5	$Ag_{956}Cu_{309}/Ag_{1106}Cu_{309}$	2.13	12.12
8/5	$Au_{956}Ni_{309}/Au_{1106}Ni_{309}$	8.56	18.97
8/5	$Au_{956}Co_{309}/Au_{1106}Co_{309}$	4.95	15.99

Table 4.12 The number of layers is that of all the NP and of the core respectively. It is noteworthy how higher is the pressure differential for the all Mackay configuration, meaning a much higher pressure on the most internal layer of the shell than that on the most external layer of the core. This makes it convenient for the smaller atoms in the core to migrate in the shell and vice-versa. It is also important to observe that a pressure differential also exists, while less pronounced, for chiral shells, without this implying the instability of such structures.

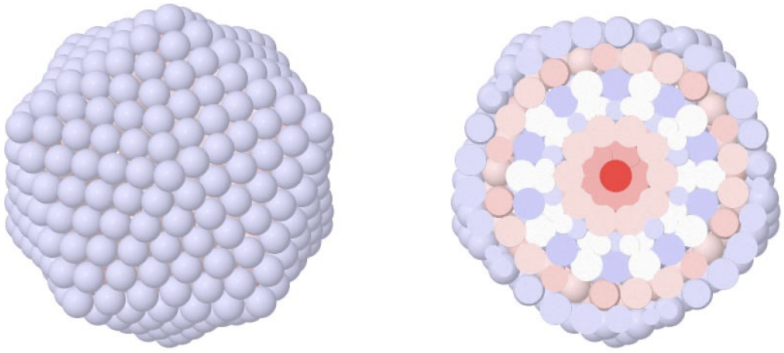

Fig. 4.33 Pressure map of $Ag_{524}Ni_{309}$. Surface and interior view. There is a relatively smooth pressure change between the strained last layer of the core and the compressed first layer of Ag. The atom at the center is very much compressed and the surface of the NP is significantly strained.

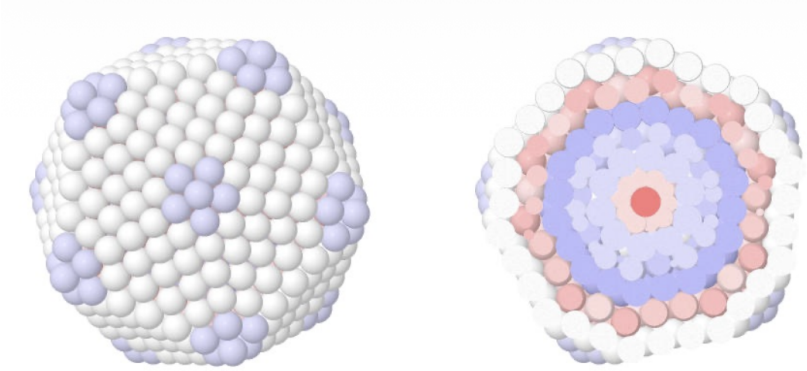

Fig. 4.34 Pressure map of $Ag_{614}Co_{309}$. Surface and interior view. There is a sharp pressure change between the strained core and the compressed first layer of Ag. The surface of the NP is somewhat strained.

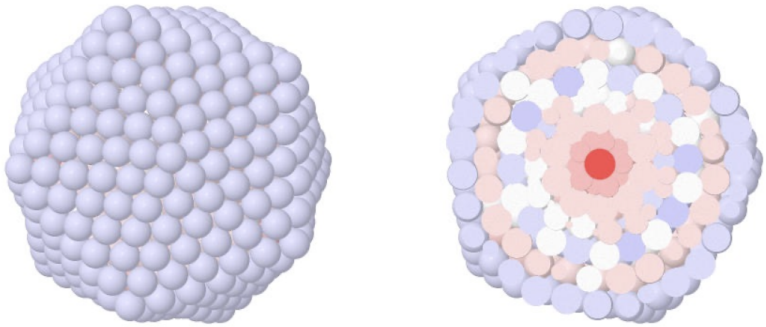

Fig. 4.35 Pressure map of $Ag_{524}Co_{309}$. Surface and interior view. There is a relatively smooth pressure change between the somewhat strained last layer of the core and the compressed first layer of Ag. The atom at the center is very much compressed and the surface of the NP is significantly strained.

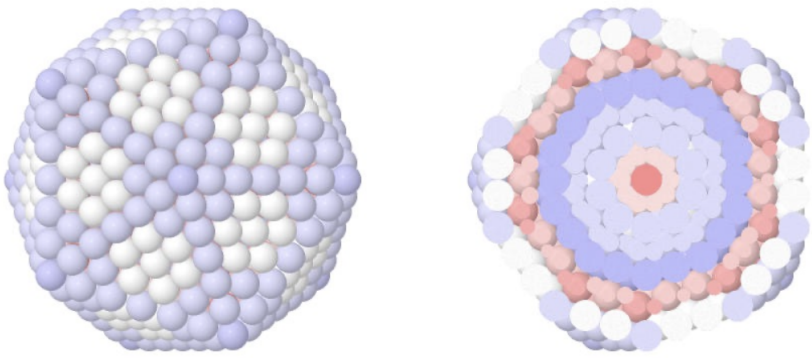

Fig. 4.36 Pressure map of $Au_{614}Co_{309}$. Surface and interior view. There is a sharp pressure change between the strained core and the compressed first layer of Ag. The surface of the NP is strained, as could be expected given the properties of gold [74].

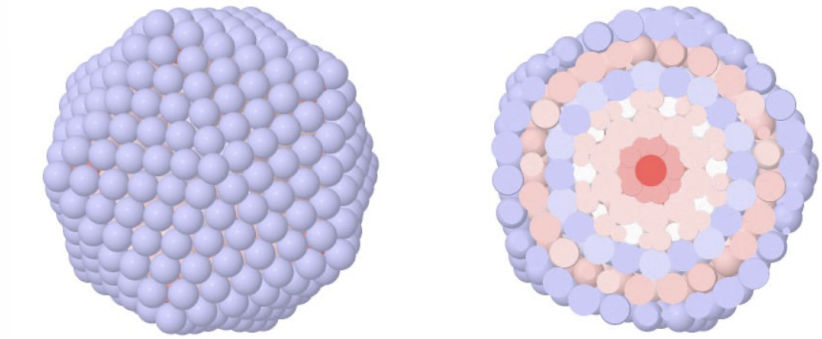

Fig. 4.37 Pressure map of $Au_{524}Co_{309}$. Surface and interior view. There is a somewhat smooth pressure change between the strained last layer of the core and the compressed first layer of Ag. The atom at the center is very much compressed and the surface of the NP is significantly strained.

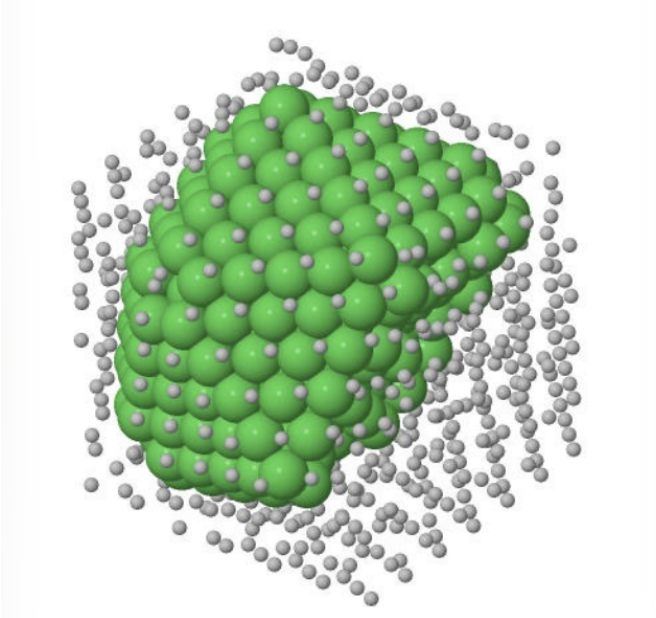

Fig. 4.38 Result of a global optimization search for $Ag_{614}Ni_{309}$. The perfectly symmetric Mackay configuration is rapidly found to be non optimal when compared to one with a de-centered core. For a chiral shell, with all layers completed ($Ag_{524}Ni_{309}$), there is need of much time for the algorithm to find some better result. Even if we add to it 90 atoms on the surface, that would still have a lower potential energy than the all Mackay configuration.

In the next chapter, beginning with the very smooth and regular process of growth we found for the formation of chiral layers, homogeneous diffusion is discussed, and this also will prove to be a major property of these chiral NPs.

Chapter 5

Diffusion and mobility on close-packed nanoparticles

In our work on MD simulations of growth, presented in Chapter 4, we have seen that the process of growth of chiral shells is generally very regular and does not create accumulations as the islands in the case of a Volmer-Weber growth [80]. The key to understand this is the study of mobility of an adatom on the surface of the NP. We limit ourselves to homogeneous diffusion, meaning the adatom is of the same chemical element as the surface. If the deposited atoms are able to move reasonably fast over the entire surface of the NP, not too much bothered by the presence of edges separating adjacent facets, then regular shapes and low-defect surfaces can be obtained. We present in section 5.1 a comparison in this sense between the Mackay and the chiral icosahedron surfaces.

Already in the case of a thin film, meaning few atomic layers deposited in a controlled manner, it is possible to see the difference between a situation when the atoms can freely move and a smooth layer-by-layer growth is obtained, and one where the surface will turn out to be irregular and disordered [81] (see Fig. 5.1). This can be studied in terms of individual adatoms on the metal surface, while it is true that one could also consider other possibilities such as small clusters of atoms or concerted displacement of already formed islands. If one studies (111) surfaces then the migration of atoms on it will be easy, while the Ehrlich-Schwoebel barrier [82], due to the need to descend the terrace, will be the limiting factor, at least in the case of a thin film. If one studies NPs, then the edges between different facets will be a further limiting factor.

We do a generalized study of Ag NPs with close-packed (111) surfaces, meaning icosahedra, both Mackay and chiral (ch1), octahedra and tetrahedra. We map adsorption sites on those surfaces in section 5.2 and then proceed to quantify the energy barriers associated with edge-crossing, for all these different surfaces. We consider two different forms of mobility:

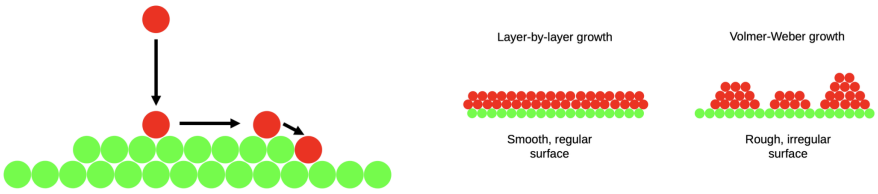

Fig. 5.1 The process of depositing atoms on a thin layer, which can be simulated by Molecular Dynamics as described in Chapter 2, can either result in a regular growth or in the formation of islands (Volmer-Weber growth), depending on whether the newly deposited atoms diffuse fast enough. Diffusion on a (111) facet is usually fast, which means the greater energy barrier is that for descending the terrace (the layer on the top), because when doing so the atom loses coordination. In the case of a NP such terrace is wrapped around the seed of the simulation or the previous growth result, meaning there are edges, as the characteristics of the NP dictates, and the greater energy barrier is the one associated to crossing them.

jumps and exchanges, depending on whether the edge is crossed by the adatom [83, 84] or the adatom takes its place on the edge or nearby [85], sending on to the other facet an atom that was previously in an edge site. All the data for diffusion by exchange, obtained with MD simulations, are presented in section 5.3, while in section 5.4, the results of an estimation of the energy barriers of the different processes by the 'drag method' are discussed. All of this is a presentation of the work published in Ref. [17], while other similar data for Cu NPs are given in section 5.5 to show how all of this depends on the surface characteristics.

5.1 Chiral smooth surface

We observed in Chapter 3 that the growth of Ch1 shells on Mackay seeds typically proceeds in a very smooth fashion as in Fig. 5.2; in the case of growth according to the Mackay icosahedral type, we do see usually a regular process, but with more imperfections and a good result only made possible by collective rearrangements [86]. The smooth growth of chiral icosahedra we assume to be related to high mobility on the surface of this kind of structure: it is possible to see in Fig. 5.3 that there are essentially no true borders on the chiral surface as opposed to what would be the case in a regular Mackay icosahedron. As a consequence of that, the path that an adatom, added during the process of growth, has to take to migrate from one facet to the next is different, as we see in Fig. 5.4.

We considered specifically the cluster $Ag_{524}Ni_{309}$ for the Ch1 shell type (the one represented in Fig. 5.2) and Ag_{923} for the Mackay kind. We run MD simulations of diffusion at different temperatures, as reported in Table 5.1, to count the number of diffusion events, by

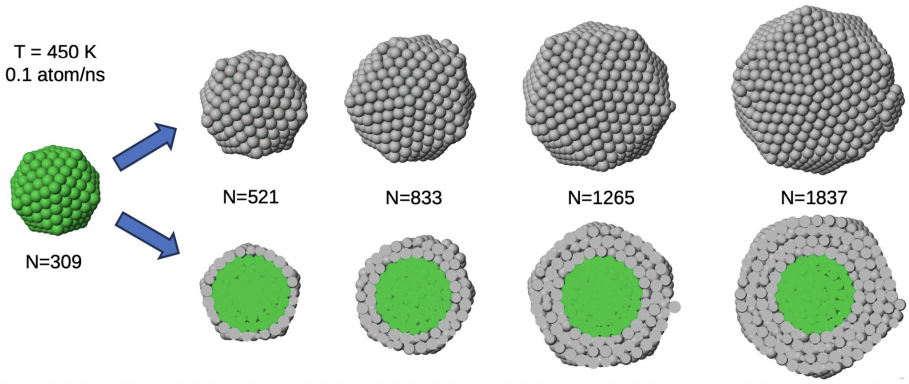

Fig. 5.2 Growth sequence realized by depositing Ag on Ni_{309} at T=450 K and with a rate of deposition of 0.1 atom/ns. It is clear that there are no island of newly added atoms that accumulates on the surface: all the new atoms migrate to the sites where they can complete the layer that is being formed.

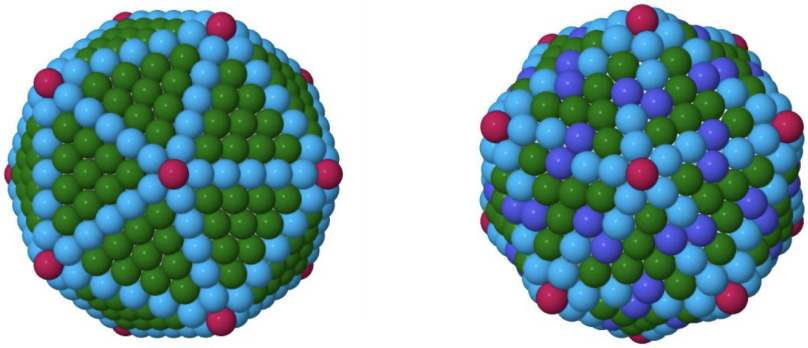

Fig. 5.3 The chiral icosahedral surface differs from the Mackay one due to its broken edges, meaning that atoms are not perfectly lined up from one vertex to the other. The atoms are coloured according to their common neighbor analysis (CNA) signature [87], applied to two of our clusters. CNA is able to distinguish the different local environments of an atom.

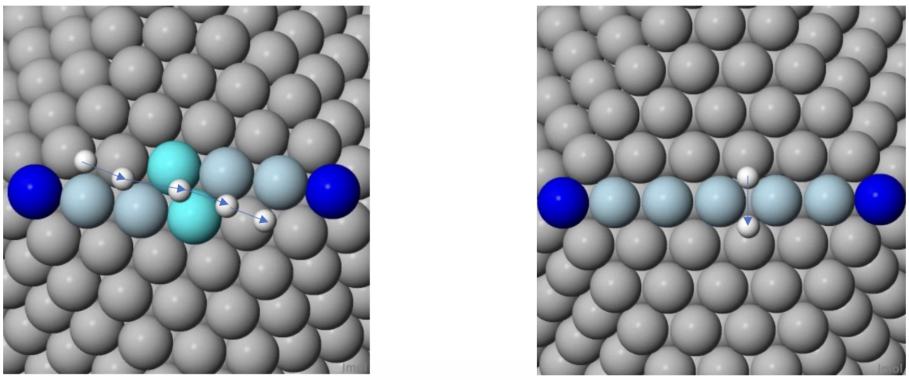

Fig. 5.4 Different way the atoms move from one facet to the other, depending whether the edge is broken, which is the case of the chiral surface, or unbroken, as on a Mackay icosahedron.

which it is meant here jumps (as shown in Fig. 5.4) since there were much less exchanges on the Mackay surface and none on the chiral one. In particular, we initially put a single adatom on the surface and then left it free to diffuse, and counted one diffusion event each time the adatom was able to move from a facet to another, i.e. when it 'climbed' the edge on the Mackay surface to the nearby facet, or passed along the broken edge of the chiral surface (see Fig. 5.4). We did usually two simulations of 100 ns each for a total of 200 ns: the data are reported in Table 5.1. The results confirm that the broken edges on the chiral surface limit much less the movement of the adatom.

We then plotted these results following the Arrhenius law $f = Ae^{-\Delta E/kT}$ to obtain the energy barrier associated to the jump from one facet to the other as shown in Fig. 5.5, and found $\Delta E = 0.28$ eV for the Mackay surface and $\Delta E = 0.16$ eV for the chiral surface which we will then see confirmed, with a different method, in section 5.4. The energy barrier is thereby almost two times greater for the Mackay surface, meaning a significant lower mobility between different facets.

5.2 Adsorption sites

As we decided to expand our study to cover all different (111) surfaces, and sort out the best one for mass mobility, we had to include both the tetrahedron and the octahedron, already discussed in Chapter 1. In addition to $Ag_{524}Ni_{309}$ and Ag_{923}, we considered Ag_{670} as a octahedron and Ag_{560} as a tetrahedron; this means all four NPs are within the size range of 1.5-2.3 nm, our main object of interest being of course the smoothness of the surface. The tetrahedron, octahedron and icosahedron are all platonic solids with triangular facets and the

TEMPERATURE	CHIRAL (ev/200ns)	MACKAY (ev/200ns)
275K	25	-
300K	28	-
325K	48	-
350K	82	6
375K	117	17
400K	153	22
425K	-	43
450K	-	53

Table 5.1 At any temperature two simulations were run, each of 100 ns, with the usual time step and atomic potential. Then the number of events of diffusion, when the adatom moves to a different facet, were counted visually. It is easy to see that the adatom moves much more freely on the Ch1 shell.

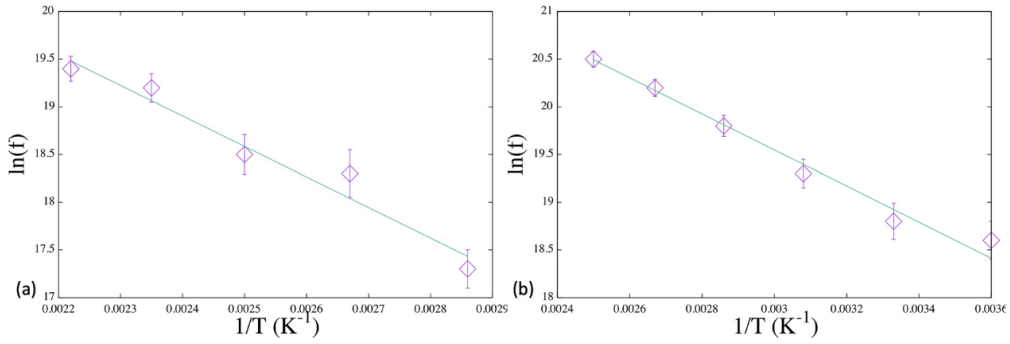

Fig. 5.5 Arrhenius plot of diffusive events (jumps) on a Mackay (a) and Ch1 (b) surface. We have plotted the logarithm of frequency in s^{-1} and the inverse of temperature in K degrees. The energy barriers turn out to be 0.28 ± 0.03 eV and 0.16 ± 0.01 eV respectively, while the prefactors for the plot are 3.6×10^{11} and 9×10^{10} respectively. Reproduced from Ref. [17]. Copyright The Royal Society of Chemistry 2025.

angle between two adjacent facet (dihedral angle) is of 70.5° for the tetrahedron, 109.5° for the octahedron and 138.2° for the icosahedron.

First of all, to make sure that the results of the various Arrhenius plots that will be discussed in section 5.3, and of those already seen in Fig. 5.5, are related to the mechanisms of diffusion relevant near the edge, we have to consider mobility within a single facet. In 3D NPs, the finite size of the (111) facets introduces inequivalences between different adsorption sites. Adsorption site energies vary depending on their position within the facet, particularly whether they are near the center of the facet or near the edges and vertices.

We show in Fig. 5.6 the various stable adsorption sides, meaning hollow sites with fcc and hcp stacking relatively to the underlying layers. All these are three-fold sites, while less coordinated sites, and particularly bridge sites [88], are not stable adsorption sites and therefore they are relevant only during the process of diffusion. We found that the energy variation on the same facet is of maximum 0.02-0.03 eV for the chiral and Mackay icosahedron, and of 0.06 eV and 0.10 eV for the tetrahedron and octahedron respectively. In all cases, it appears that the energy variation favors the sites near the vertices and the edges.

We also calculated the energy barrier for moving within a facet, according to the drag method that will be used in section 5.4, and found energy barriers in the range 0.04-0.06 eV. This is compatible with what found for diffusion on a perfect (111) face of an infinite surface [88].

5.3 Mass diffusion

Doing MD simulations of diffusion, we found that apart from the Mackay and chiral icosahedral surfaces already considered in Fig. 5.5, the adatom jump from one facet to the next was not prevalent as a process of mobility. Here we consider diffusion by exchange; in this case, we can no longer refer to adatom diffusion, but only to mass diffusion, since the atom diffusing on the second facet is not the same as the one diffusing on the first.

We describe this process in Fig. 5.7, in the case of the Mackay icosahedron, which could be a simple or chain process [89], and then in the case of the octahedron and tetrahedron in Fig. 5.8. We do not consider the chiral icosahedron in this case, as exchange processes are never observed in the MD simulations and are difficult to predict due to the absence of well-defined edges.

While for the MD simulations of diffusion on the Mackay and chiral icosahedron, the considered temperature range, already seen in Table 5.1, was of 275-400K and 350-450K respectively, for the octahedron and tetrahedron we have 275-350K and 75-150K. In the case of the Mackay icosahedron, we used the same simulations considered for diffusion

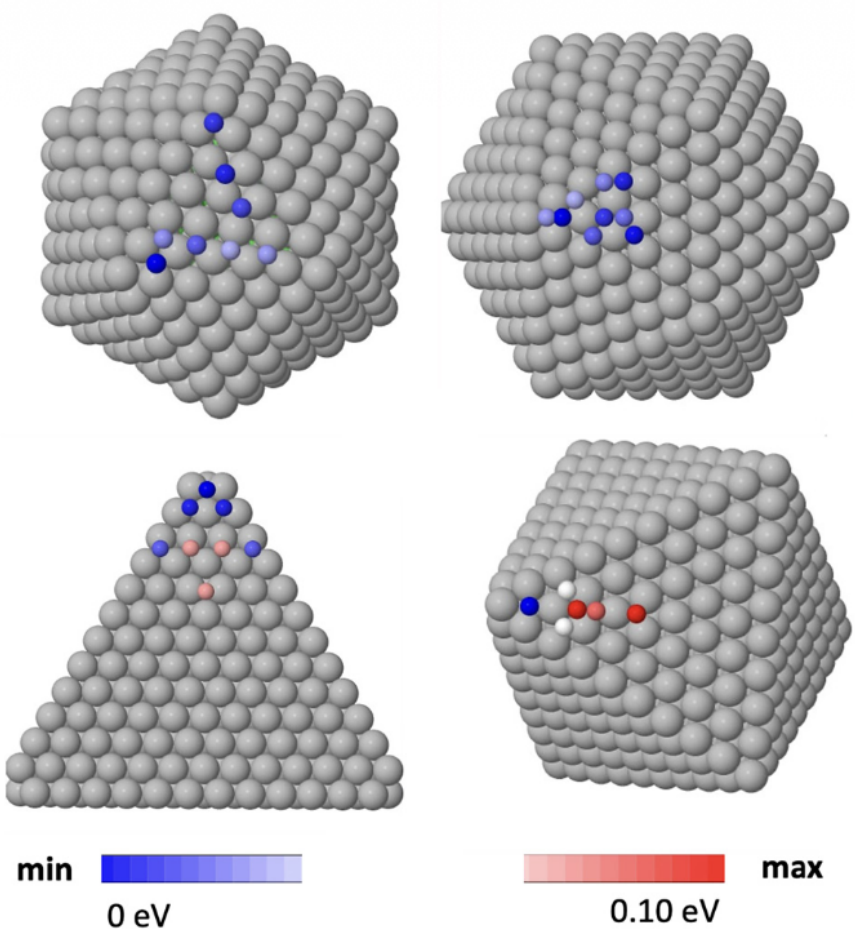

Fig. 5.6 All the various sites of adsorption mapped on the surface of our four NPs under consideration. It is easy to see that on the surface of the Mackay and chiral icosahedron all the sites have very reduced energy differences, while on the octahedron and tetrahedron the sites near the vertices and edges are meaningfully favored. In the case of the tetrahedron the vertices are removed since this will be the way we consider them in our simulations. All sites corresponds to clusters minimized with the use of quenched Molecular Dynamics (qMD). Reproduced from Ref. [17]. Copyright The Royal Society of Chemistry 2025.

by jump, the two being indipendent processes, except we added two more temperatures so that the range ended up being 350-500K. In the case of the tetrahedron, the four vertices, being on three-fold sites just like the adatoms on the facet, had to be removed, otherwise they would tend to become new adatoms; moreover the temperature had to be very low to avoid this happening to other nearby atoms as well. In all these MD simulations, we let one adatom free to diffuse on the surface and count an event of diffusion each time the adatom has become part of the edge and another atom has been sent to move on another facet (mass diffusivity). When it happened, during simulations of diffusion on the octahedron or tetrahedron, that some other atom, as one of the vertices of the octahedron or an atom on the edge of the tetrahedron, lost its place, we interrupted the simulation taking the count of events we had and considering of course only the time from the beginning of the simulation to its interruption to compute the frequency.

The results are presented in Fig. 5.9, in form of Arrhenius plots as those used in Fig. 5.5. We found for diffusion by exchange on the Mackay icosahedron a barrier of 0.49 eV when only the simple process is concerned (see Fig. 5.7), and of 0.53 eV when complex multi-atomic chain processes are concerned. In the case of the octahedron and tetrahedron we found respectively 0.09 eV and 0.06 eV, which are near enough the energetic barrier for moving on the facet that this will also be relevant when making a comparison with drag estimates. We also observed in our MD simulations a tendency for the adatom diffusing on a tetrahedron, or even more on an octahedron, to enter a process of exchange when near the vertices (removed in the case of the tetrahedron), which is also a position when the adatom tends to stay because of the more favorable adsorption energy (see Fig. 5.6).

5.4 Drag method estimates

We also calculate the energy barrier with a separate method to find it, as in Table 5.2, for processes, such as jumps on the octahedral or tetrahedral surface, that occurred much rarely if not at all. Moreover we want an independent proof that the different dihedral angle between the facets, or the different transition path for a chiral or Mackay icosahedron, is the reason for the different adatom and mass diffusivities, given by our dynamical energy barriers (calculated with an Arrhenius plot).

The drag method simply requires the use of qMD as already described in Chapter 2. We simply decide that the relaxation by quenching to the local minimum is not going to apply to one coordinate of our adatom: this needs to be the coordinate that describe the transition process from the beginning to the end, which could either be the arrival of the adatom on the other facet (jump) or its inclusion in the edge (exchange). This fixed coordinate needs to

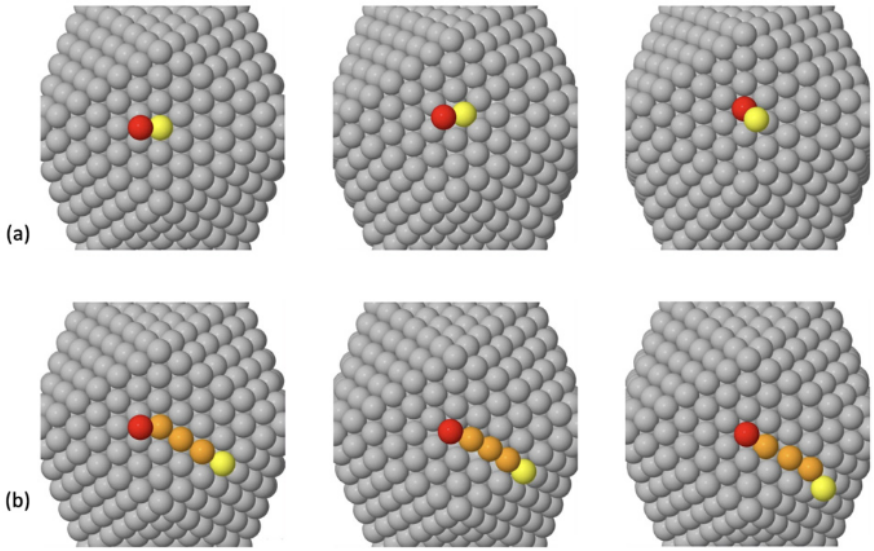

Fig. 5.7 Mass diffusion by exchange on the Mackay icosahedron. (a) Simple process, with two atoms involved: the adatom (in red in the figure) and one atom initially belonging to the edge (in yellow). The adatom takes the place of the edge atom, which becomes an adatom on the adjacent facet. (b) More complex process, involving many atoms: the adatom (in red), an edge atom in the opposite edge of the adjacent facet (in yellow) and a row of atoms between them (in orange). Orange atoms are pushed away by the red atom, and the yellow atom becomes and adatom on the bottom left icosahedral facet. Reproduced from Ref. [17]. Copyright The Royal Society of Chemistry 2025.

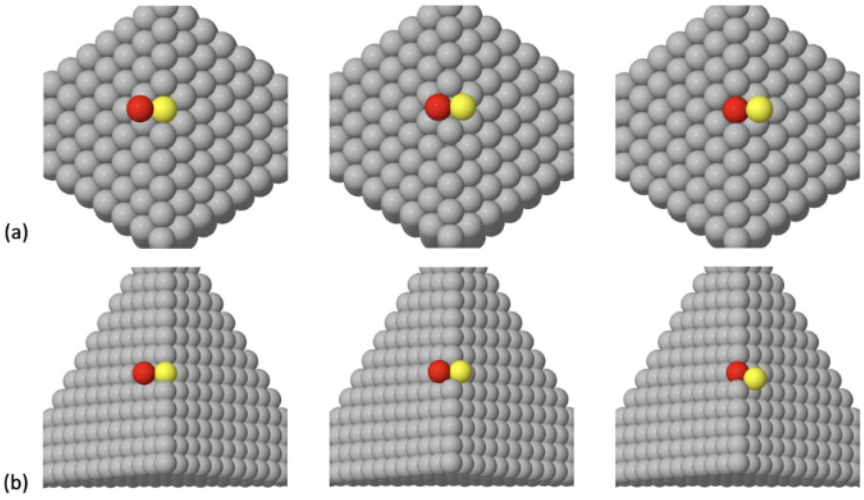

Fig. 5.8 Mass diffusion by exchange on the octahedron and tetrahedron. Adatom on the facet of the (a) octahedron and (b) tetrahedron is colored in red. The adatom takes the place of one of the edge atoms (in yellow), which becomes an adatom on the adjacent facet. Reproduced from Ref. [17]. Copyright The Royal Society of Chemistry 2025.

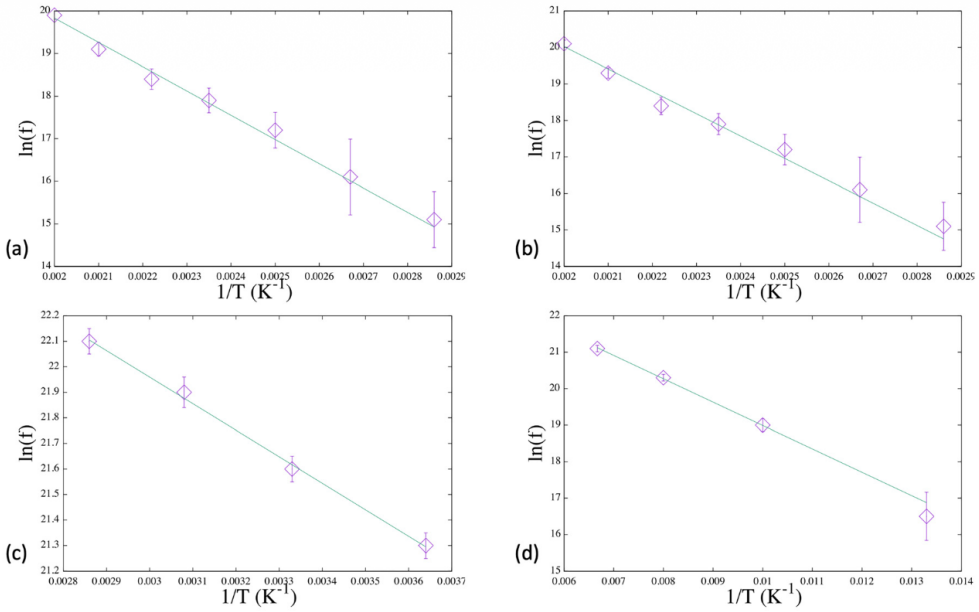

Fig. 5.9 Arrhenius plot for inter-facet diffusion by exchange on the Mackay, octahedron and tetrahedron. We have plotted the logarithm of frequency in s^{-1} and the inverse of temperature in K degrees. (a) Mackay icosahedron, simple exchange process. Energy barrier and prefactor are $\Delta E = 0.40 \pm 0.02$ eV and $A = 3.710^{13} s^{-1}$. (b) Mackay icosahedron, many atom exchange process. Energy barrier and prefactor are $\Delta E = 0.53 \pm 0.03$ eV and $A = 1.010^{14} s^{-1}$. (c) Octahedron. Energy barrier and prefactor are $\Delta E = 0.09 \pm 0.01$ eV and $A = 7.910^{10} s^{-1}$. (d) Tetrahedron. Energy barrier and prefactor are $\Delta E = 0.06 \pm 0.01$ eV and $A = 1.110^{11} s^{-1}$. It is noteworthy, when comparing the two exchange mechanisms for the Mackay icosahedron ((a)and(b)), that the prefactor is higher for the multi-atomic chain process (b); this tendency has been observed for a variety of multi-atomic processes in literature. Reproduced from Ref. [17]. Copyright The Royal Society of Chemistry 2025.

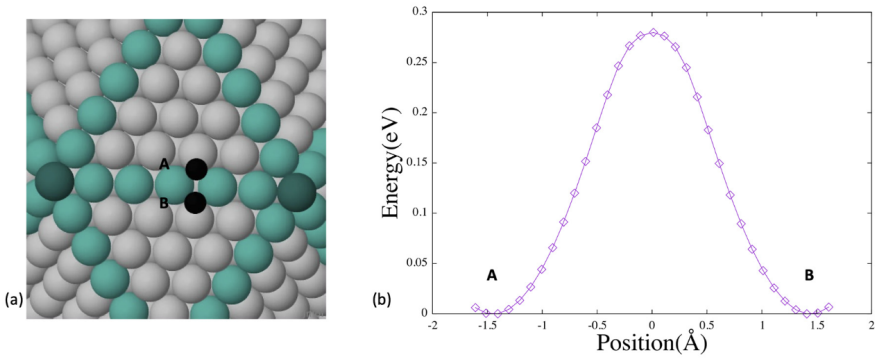

Fig. 5.10 Edge crossing by jump on the Mackay icosahedron. (a) Adsorption sites before and after the crossing of the edge by jump diffusion. (b) Energy profile of the diffusion process, estimated by the drag method. The energy barrier is 0.27 eV. Reproduced from Ref. [17]. Copyright The Royal Society of Chemistry 2025.

be modified very slowly (typically by 0.1 Angstrom), to take the full energetic profile and to identify the relevant saddle point in particular: the difference between the saddle and the minimum gives the energy barrier [90]. In our application of the method, we also kept fixed the atoms at the center of the NP (13, 6 and 4 atoms for the icosahedron, octahedron and tetrahedron respectively) and all the vertices except those nearest to the diffusing atom; we also applied some variants on this protocol and found no difference in the result.

The energy profiles we obtained for the exchange processes are a little bit discontinuous, though we were able to get consistent results that we report in Table 5.2. In Fig. 5.10 we show the energy profile for mobility by jump on the Mackay icosahedron and in Fig. 5.11 we do the same for the chiral icosahedron, where crucially there are more energy barriers, but the relevant one is the higher. The result are 0.27 eV and 0.15 eV that are well within the error associated to the dynamical energy barrier showed in Fig. 5.5. In Fig. 5.12 the other two jump barrier are showed, and the results are compatible with jump not being observed as a relevant diffusion mechanism for the octahedron and the tetrahedron.

Based on the results reported in Table 5.2 we can make some considerations. It is clear that the results for exchange on the icosahedron are mostly confirmed by the Arrhenius plots: in the case of the simple exchange the dynamical energy barrier is of 0.40 ± 0.02 eV as opposed to 0.46 eV calculated with the drag method, which is not a huge difference, while for the chain multi-atomic process we have 0.53 ± 0.03 eV compared to 0.52-0.54 eV, which is to say a full agreement.

The energy barrier for edge crossing on the octahedral surface is slightly higher than that calculated by the drag method (0.13 eV compared to 0.09 eV). This discrepancy between the two methods can be explained by closely examining the inter-facet diffusion process. To

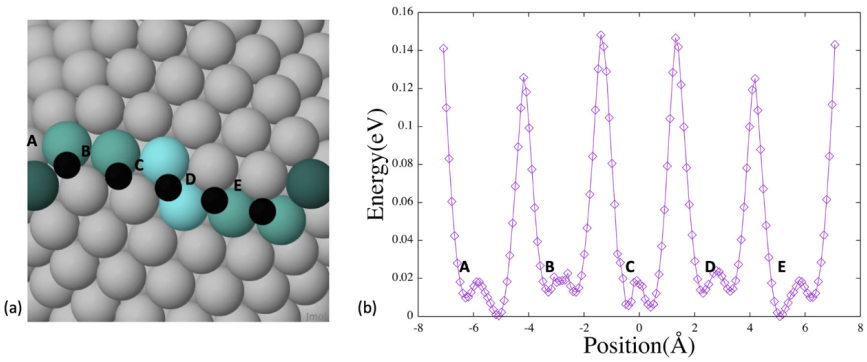

Fig. 5.11 Edge crossing by jump on the chiral icosahedron. (a) Locally stable adsorption sites along the inter-facet diffusion pathway. (b) Energy profile of the diffusion process, estimated by the drag method. The energy barrier for inter-facet diffusion is the highest among the barriers of the subsequent jump diffusion steps, i.e. 0.15 eV. Reproduced from Ref. [17]. Copyright The Royal Society of Chemistry 2025.

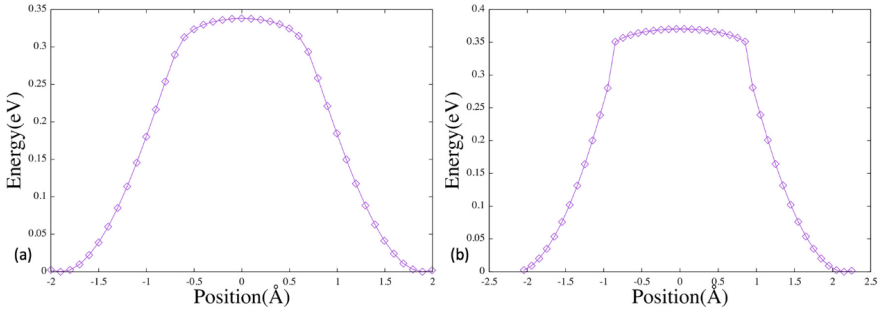

Fig. 5.12 Energy profiles for edge crossing diffusion by jump on the (a) octahedron and (b) tetrahedron, estimated by the drag method. The energy barriers are 0.33 and 0.38 eV, respectively. Reproduced from Ref. [17]. Copyright The Royal Society of Chemistry 2025.

STRUCTURE	PROCESS	BARRIER (ev)
Mackay icosahedron	Jump	0.28
Mackay icosahedron	Exchange (simple)	0.46
Mackay icosahedron	Exchange (chain)	0.52-0.54
Chiral icosahedron	Jump	0.15
Octahedron	Jump	0.33
Octahedron	Exchange (edge center)	0.31
Octahedron	Exchange (near vertices)	0.13
Tetrahedron	Jump	0.38
Tetrahedron	Exchange (edge center)	0.06
Tetrahedron	Exchange (near removed vertices)	0.04

Table 5.2 Summary of our results for inter-facet diffusion barriers on Ag NPs with closed-packed (111) surface. Energy barriers in the Table have been calculated by the drag method, but are in agreement with dynamical barriers estimated by the Arrhenius plot.

move from one facet to another, the adatom must first arrive at the edge via a sequence of intra-facet jump diffusion events; then, it must cross the edge through a single inter-facet diffusion step. In the cases analyzed so far, edge-crossing energy barriers are much higher than those associated with intra-facet diffusion, so the inter-facet diffusion rate is dominated by a single step with the highest energy barrier—namely, edge crossing. The low-barrier diffusion steps preceding the crossing mainly influence the pre-exponential factor in the Arrhenius relation. However, on the octahedral surface, this approximation no longer holds, as the energy barriers for edge crossing by exchange are very close to those for jump diffusion on the (111) surface. Therefore, even though our data are well fitted by a linear interpolation (see Fig. 5.9), the estimated energy barrier represents an effective barrier for the entire diffusion process, which includes both edge-approaching and edge-crossing events. The value lies between the barriers of the two distinct steps (0.06 and 0.13 eV, as estimated by the drag method). The same considerations apply to inter-facet diffusion on the tetrahedral surface. However, in this case, intra-facet jump diffusion and edge crossing by exchange have almost the same energy barriers (0.04–0.06 eV, as estimated by the drag method). The dynamical energy barrier is of 0.06 ± 0.01 eV as well.

If we take a general panoramic of the various energy barriers, we can also say that the two better results, for diffusion by jump and exchange respectively, are the chiral icosahedron and the tetrahedron. This means both the smoother surface and the sharper one are good for mass diffusivity in the case of homogeneous diffusion, albeit with a different mechanism. Since one of the implications of this is for growth (see Fig. 5.2), it is interesting to see that the growth of tetrahedra also has been found to proceed well [91].

STRUCTURE	PROCESS	BARRIER (ev)
Mackay icosahedron	Jump	0.33
Mackay icosahedron	Exchange (edge center)	0.64
Mackay icosahedron	Exchange (near vertices)	0.47
Octahedron	Jump	0.43
Octahedron	Exchange (edge center)	0.34
Octahedron	Exchange (near vertices)	0.19
Tetrahedron	Jump	0.55
Tetrahedron	Exchange (edge center)	0.05
Tetrahedron	Exchange (near removed vertices)	0.05

Table 5.3 Summary of our results for inter-facet diffusion barriers on Cu NPs with closed-packed (111) surface, except for the chiral icosahedron. Energy barriers in the Table have been calculated by the drag method. There is no barrier for the jump on the chiral icosahedron (differently than in Table 5.2), as we did not consider that. The general tendency is for the Cu NPs to have greater energy barriers than Ag NPs, but privileging the same processes.

5.5 Cu nanoparticles

As the difference between the energy barriers associated to the diffusion processes on icosahedra, both Mackay and chiral, octahedra and tetrahedra, are due to different characteristics of the surfaces involved, we consider NPs of Cu atoms to see if they remains similar when changing the metal species both of the surface and of the adatom. We did not consider the chiral icosahedron as that would have required picking a different metal species to fill the core, outside of the nanoalloys we saw in Chapter 4. We first calculate, as we did in Fig. 5.6, the energy differences between adsorption sites and the energy barrier for moving on a single facet. The energy differences are greater: 0.05 eV on an icosahedron and 0.14 eV on both the octahedron and tetrahedron; the energy barrier we found to be similar but somewhat lower on a Cu surface (0.03-0.04 eV), regardless of the shape of the NP. The greater strength of the Cu-Cu interaction (energy cohesion), compared to the Ag-Ag interaction, could explain both the greater energy variation on the facet, and the somewhat lower energy barrier due to the atoms being more strictly linked.

We applied the drag method to then find the energy barriers for the Cu NPs. We found those to be higher than the equivalent for Ag NPs (see Table 5.3), consistently with what expected given the greater energy cohesion and so the greater 'cost' associated to the loss of atomic coordination. In the case of exchanges on the icosahedral edges, we did not find chain processes as those seen on the Ag Mackay icosahedron, but observed a relevant difference in the energy cost that privileges (simple) exchanges happening near the vertices. This is similar to what seen for octahedra and tetrahedra also in the case of Ag NPs; that we also found that for the icosahedron when considering Cu NPs, may be linked to the

greater energy differences on the facet, which also privileges the adsorption site near the vertices. While we did not calculate dynamical energy barriers in this case, we did some MD simulations of diffusion, and saw these barriers to be consistent with the prevalent diffusivity mechanisms observed in simulations; in the case of the Mackay icosahedron in particular, we saw exchanges happening almost always near the vertices.

Conclusions

This Ph.D. thesis is devoted to the development of a new method for the design of nanoparticle structures with icosahedral symmetry, and to their characterization via computational techniques.

Our design strategy, which is presented and discussed in Chapter 3, allows us to build icosahedral aggregates of various kinds, with multishell arrangement, and to select the appropriate chemical species to be used to build promisingly stable structures (see Ref. [14]). Icosahedral nanoparticles are grouped into different chirality classes, going from the regular Mackay icosahedron to the Bergman icosahedron, which are both achiral, and with all the different levels of chirality in between. In Chapter 4 this theory is confirmed for different nanoalloys: Ni@Ag, Co@Ag, Cu@Ag, Ni@Au, Co@Au and Fe@Au. In all of these cases, a noble metal is considered for the shell, and a metal with smaller atomic radius, according to the selection rules described in Chapter 3, and higher cohesive energy, is considered for the core. We have been able, in particular, to grow chiral shells (of the Ch1 type) in all of these cases, performing MD simulations with an appropriate initial seeds and appropriate temperature ranges and growth rates. In general, the growth of Ag shells turned out to be smoother than that of Au shells, due to the tendency of Au to reconstruct surfaces and form rosettes [74]; however, very good growth results were obtained also with Au, and particularly with Fe@Au. Together with the growth of chiral shells on a Mackay core, another important result is the growth of anti-Mackay and generalized anti-Mackay shells, which we observed in particular in the Cu@Ag system. The description of anti-Mackay icosahedral shells according to the same design principle used for chiral shells completes our general theory for icosahedral aggregates [14].

The stability of these NPs, and of structures built according to our design principle in general, was tested by two different procedures. Heating MD simulations were performed to investigate the kinetic stability up to the melting. In addition, the chemical ordering stability was checked by swapping atoms of different species between the core and the shell. For the alloy systems mentioned aboved, the swap turned out to be energetically disfavored when performed between a chiral shell and the Mackay core below. The atom-swapping tests were

also put in relation to the atomic-level pressure profiles of the NPs. Another important feature highlighted by the pressure analysis of the chiral shell is that its inhomogeneously strained, which could be an advantage for catalytic applications.

Overall, the most impressive result is the very well-functioning growth process, which should be possible to observe experimentally if searched for. The MD simulations of growth, particularly with the Ni@Ag system, gave a smooth growth also on an incomplete initial seed, demonstrating the robustness of this growth pathway. In general, the formation of chiral layers one on top of the other appeared to proceed without obstacles.

The study of homogeneous surface diffusion presented in Chapter 5 was initially conceived to understand and rationalize the smoothness of the growth of chiral icosahedral shells, in comparison with the Mackay ones, based on the different characteristics of the surface; then it was generalized to other geometric shapes with (111) surface facets [17].

The investigation of different diffusion mechanisms on close-packed surfaces, which we made with regard to Ag NPs, and then to Cu NPs for confirmation, succeeded in explaining the smooth and efficient process of growth of chiral icosahedra [14], and of tetrahedra [91]. The most important process is the diffusion of the adatom between nearby facets by edge-crossing, for which we calculated the energy barriers for all different shapes. Edge-crossing barriers turned out to be lower for the chiral icosahedron and for the tetrahedron. In particular, We found that, in the first case, edge-crossing takes place by 'jump', while in the second case by 'exchange', so that in the end the highest mass diffusivity is achieved for both the smoothest NP, which is the chiral icosahedron that lacks well-defined edges, and the sharpest NP, which is the tetrahedron. With regard to the chiral icosahedron specifically, the high adatom diffusivity could also be generalizable to hetero-diffusion, meaning atoms of a different chemical element diffusing on the surface and 'jumping' from one facet to the next. This, together with the high strain of chiral surfaces, could be helpful in catalytic applications, which are one of the main possible applications of the multilayer chiral icosahedra we described in this thesis.

The results presented in this thesis are mostly published in Refs. [14, 17], except for some of the growth sequences, the atom-swapping energies and the pressure analysis in Chapter 4, and the study of energy barrier for diffusion on Cu NPs in Chapter 5, which are unpublished. The most obvious development on these results, which are all computational, would clearly be an experimental verification of the feasibility of chiral multilayer icosahedra. These could be searched for in gas phase condensation experiments, where the initial seed would have to be mass selected, which could be done within already existing systems given that the computational results, at least for Ni@Ag, are robust for an incomplete seed. An

experimental finding could then open the door to useful application whether in catalysis or in magnetic NPs with a protected core or in plasmonics.

Apart from experimental developments, there is room for further computational work that addresses the following questions:

1) How stable would be a chiral icosahedron with an hollow cavity inside, instead of, for instance, the most central 13 atoms?

2) Is the diffusion on a Ch2, Ch3, ..., Bergman surface even easier than on a Ch1 surface, as would be expected given the more pronounced lack of edges?

3) How are the results for diffusion going to generalize to different kinds of metals: would an Au surface show different characteristics?

4) How much are the results for adatom diffusion, that which works by 'jumps', going to apply to heterogeneous diffusion?

5) to what extent a spherically confined colloidal system, with entropy-driven dynamics, could reproduce the growth of the icosahedral aggregates according to our rules, which are indeed derived from simple geometrical considerations?

References

[1] J. A. Alonso. *Structure and Properties of Atomic Nanoclusters*. Imperial College Press, 2005.

[2] R. L. Johnston. *Atomic and Molecular Clusters*. Taylor and Francis, 2002.

[3] R. Ferrando. *Structure and Properties of Nanoalloys*. Elsevier, 2016.

[4] R. Ferrando, J. Jellinek, and R. L. Johnston. "Nanoalloys: From Theory to Applications of Alloy Clusters and Nanoparticles". In: *Chem. Rev.* 108 (2008), pp. 845–910.

[5] P. Grammatikopoulos. "Atomistic modeling of the nucleation and growth of pure and hybrid nanoparticles by cluster beam deposition". In: *Current Opinion in Chemical Engineering* 23 (2019). Frontiers of Chemical Engineering: Molecular Modeling, pp. 164–173. ISSN: 2211-3398. DOI: https://doi.org/10.1016/j.coche.2019.04.004. URL: http://www.sciencedirect.com/science/article/pii/S2211339818300741.

[6] S. L. Girshick and C.-P. Chiu. "Homogeneous nucleation of particles from the vapor phase in thermal plasma synthesis". In: *Plasma Chemistry and Plasma Processing* 9 (1989), pp. 355–369.

[7] D. Nelli, A. Krishnadas, R. Ferrando, and C. Minnai. "One-Step Growth of Core–Shell (PtPd)@Pt and (PtPd)@Pd Nanoparticles in the Gas Phase". In: *The Journal of Physical Chemistry C* 124 (2020), pp. 14338–14349.

[8] P. Andreazza, V. Pierron-Bohnes, F. Tournus, C. Andreazza-Vignolle, and V. Dupuis. "Structure and order in cobalt /platinum-type nanoalloys: from thin films to supported clusters". In: *Surf. Sci. Rep.* 70 (2015), pp. 188–258.

[9] M. Andrzejczuk, A. Roguska, M. Michalska, L. Lipińska, A. Czerwiński, M. Cantoni, A. Krawczyńska, and M. Lewandowska. "STEM study of Li4Ti5O12 anode material modified with Ag nanoparticles". In: *Journal of microscopy* 264 (2016), pp. 41–47.

[10] D. Schooss, M. N. Blom, J. H. Parks, B. v. Issendorff, H. Haberland, and M. M. Kappes. "The Structures of Ag_{55}^{+} and Ag_{55}^{-}: Trapped Ion Electron Diffraction and Density Functional Theory". In: *Nano Letters* 5 (2005), pp. 1972–1977.

[11] T. Rapps, R. Ahlrichs, E. Waldt, M. M. Kappes, and D. Schooss. "On the Structures of 55-Atom Transition-Metal Clusters and Their Relationship to the Crystalline Bulk". In: *Angewandte Chemie International Edition* 52 (2013), pp. 6102–6105.

[12] D. M. Wells, G. Rossi, R. Ferrando, and R. E. Palmer. "Metastability of the atomic structures of size-selected gold nanoparticles". In: *Nanoscale* 7 (2015), pp. 6498–6504.

[13] G. Benetti, E. Cavaliere, R. Brescia, S. Salassi, R. Ferrando, A. Vantomme, L. Pallecchi, S. Pollini, S. Boncompagni, B. Fortuni, M. J. Van Bael, F. Banfi, and L. Gavioli. "Tailored Ag–Cu–Mg multielemental nanoparticles for wide-spectrum antibacterial coating". In: *Nanoscale* 11 (2019), pp. 1626–1635.

[14] N. Canestrari, D. Nelli, and R. Ferrando. "General theory for packing icosahedral shells into multi-component aggregates". In: *Nature Communications* 16 (2025), p. 1655. DOI: 10.1038/s41467-025-56952-1.

[15] D. L. D. Caspar and A. Klug. "Physical Principles in the Construction of Regular Viruses". In: *Cold Spring Harbor Symposia on Quantitative Biology* 27 (1962), pp. 1–24. DOI: 10.1101/SQB.1962.027.001.005.

[16] A. L. Mackay. "A dense non-crystallographic packing of equal spheres". In: *Acta Crystallogr.* 15 (1962), pp. 916–918.

[17] N. Canestrari, R. Ferrando, and D. Nelli. "In search of the smoothest nanoparticle surface: diffusion and mobility on Ag clusters". In: *Nanoscale* (2025).

[18] R. Narayanan and M. A. El-Sayed. "Catalysis with Transition Metal Nanoparticles in Colloidal Solution: Nanoparticle Shape Dependence and Stability". In: *The Journal of Physical Chemistry B* 109 (2005), pp. 12663–12676.

[19] S. Mostafa, F. Behafarid, J. R. Croy, L. K. Ono, L. Li, J. C. Yang, A. I. Frenkel, and B. R. Cuenya. "Shape-Dependent Catalytic Properties of Pt Nanoparticles". In: *Journal of the American Chemical Society* 132 (2010), pp. 15714–15719.

[20] K. L. Kelly, E. Coronado, L. L. Zhao, and G. C. Schatz. "The Optical Properties of Metal Nanoparticles: The Influence of Size, Shape, and Dielectric Environment". In: *J. Phys. Chem. B* 107 (2003), pp. 668–677.

[21] F. Baletto and R. Ferrando. "Structural properties of nanoclusters: Energetic, thermodynamic, and kinetic effects". In: *Rev. Mod. Phys.* 77 (2005), pp. 371–423.

[22] M. Tsuji, N. Nakamura, M. Ogino, K. Ikedo, and M. Matsunaga. "Crystal structures and growth mechanisms of octahedral and decahedral Au@ Ag core-shell nanocrystals prepared by a two-step reduction method". In: *CrystEngComm* 14 (2012), pp. 7639–7647.

[23] Z. W. Wang and R. E. Palmer. "Determination of the Ground-State Atomic Structures of Size-Selected Au Nanoclusters by Electron-Beam-Induced Transformation". In: *Phys. Rev. Lett.* 108 (2012), p. 245502.

[24] Z. Li, N. Young, M. D. Vece, S. Palomba, R. Palmer, A. Bleloch, B. Curley, R. Johnston, J. Jiang, and J. Yuan. "Three-dimensional atomic-scale structure of size-selected gold nanoclusters". In: *Nature* 451 (2008), pp. 46–48.

[25] J. Penuelas, P. Andreazza, C. Andreazza-Vignolle, H. Tolentino, M. D. Santis, and C. Mottet. "Controlling Structure and Morphology of CoPt Nanoparticles through Dynamical or Static Coalescence Effects". In: *Phys. Rev. Lett.* 100 (2008), p. 115502.

[26] D. Nelli, C. Roncaglia, R. Ferrando, and C. Minnai. "Shape Changes in AuPd Alloy Nanoparticles Controlled by Anisotropic Surface Stress Relaxation". In: *The Journal of Physical Chemistry Letters* 12 (2021), pp. 4609–4615.

[27] S. Ino. "Stability of Multiply-Twinned Particles". In: *J. Phys. Soc. Jpn.* 27 (1969), pp. 941–953.

[28] A. Howie and L. D. Marks. "Elastic strains and the energy balance for multiply twinned particles". In: *Phil. Mag. A* 49 (1984), pp. 95–109.

[29] I. A. Harris, R. S. Kidwell, and J. A. Northby. "Structure of Charged Argon Clusters Formed in a Free Jet Expansion". In: *Phys. Rev. Lett.* 53 (1984), p. 2390.

[30] D. Bochicchio and R. Ferrando. "Size-Dependent Transition to High-Symmetry Chiral Structures in AgCu, AgCo, AgNi, and AuNi Nanoalloys". In: *Nano Lett.* 10 (2010), pp. 4211–4216.

[31] E. Aprà, F. Baletto, R. Ferrando, and A. Fortunelli. "Amorphization Mechanism of Icosahedral Metal Nanoclusters". In: *Phys. Rev. Lett.* 93 (2004), p. 065502.

[32] N. Khan, A. Uhl, S. Shaikhutdinov, and H.-J. Freund. "Alumina supported model Pd-Ag catalysts: A combined STM, XPS, TPD and IRAS study". In: *Surf. Sci.* 600 (2006), p. 1849.

[33] D. Spanjaard and M.-C. Desjonqueres. *Concepts in surface physics*. Springer Verlag, 2002.

[34] G. Rossi and R. Ferrando. "Searching for low-energy structures of nanoparticles: a comparison of different methods and algorithms". In: *J. Phys. Cond. Mat.* 21 (2009), p. 084208.

[35] G. Rossi and R. Ferrando. "Global optimization by excitable walkers". In: *Chem. Phys. Lett.* 423 (2006), pp. 17–22.

[36] M. P. Allen and D. J. Tildesley. *Computer Simulation of Liquids*. Clarendon, 1987.

[37] R. P. Gupta. "Lattice relaxation at a metal surface". In: *Phys. Rev. B* 23 (1981), p. 6265.

[38] V. Rosato, M. Guillopé, and B. Legrand. "Thermodynamical and structural properties of f.c.c. transition metals using a simple tight-binding model". In: *Phil. Mag. A* 59 (1989), p. 321.

[39] F. Cleri and V. Rosato. "Tight-binding potentials for transition metals and alloys". In: *Phys. Rev. B* 48 (1993), p. 22.

[40] M. J. López and J. Jellinek. "On the problem of fitting many-body potentials. I. The minimal maximum error scheme and the paradigm of metal systems". In: *J. Chem. Phys.* 110 (1999), pp. 8899–8911.

[41] F. Baletto, C. Mottet, and R. Ferrando. "Growth of Three-Shell Onionlike Bimetallic Nanoparticles". In: *Phys. Rev. Lett.* 90 (2003), p. 135504.

[42] F. Baletto, C. Mottet, and R. Ferrando. "Growth simulations of silver shells on copper and palladium nanoclusters". In: *Phys. Rev. B* 66 (2002), p. 155420.

[43] G. Rossi, G. Schiappelli, and R. Ferrando. "Formation Pathways and Energetic Stability of Icosahedral $Ag_{shell}Co_{core}$ Nanoclusters". In: *J. Comput. Theor. Nanosci.* 6 (2009), p. 841.

[44] Y. Li, E. Blaisten-Barojas, and D. Papaconstantopoulos. "Structure and dynamics of alkali-metal clusters and fission of highly charged clusters". In: *Physical Review B* 57 (1998), p. 15519.

[45] B. J. Alder and T. E. Wainwright. "Studies in molecular dynamics. I. General method". In: *The Journal of Chemical Physics* 31 (1959), pp. 459–466.

[46] H. C. Andersen. "Molecular dynamics simulations at constant pressure and/or temperature". In: *The Journal of Chemical Physics* 72 (1980), pp. 2384–2393.

[47] F. Baletto, C. Mottet, and R. Ferrando. "Molecular dynamics simulations of surface diffusion and growth on silver and gold clusters". In: *Surf. Sci.* 446 (2000), pp. 31–45.

[48] G. Sanzone, J. Yin, K. Cooke, H. Sun, and P. Lievens. “Impact of the gas dynamics on the cluster flux in a magnetron cluster-source: Influence of the chamber shape and gas-inlet position”. In: *Review of Scientific Instruments* 92 (2021).

[49] R. H. Byrd, P. Lu, J. Nocedal, and C. Zhu. “A Limited Memory Algorithm for Bound Constrained Optimization”. In: *SIAM Journal on Scientific Computing* 16 (1995), pp. 1190–1208.

[50] J. Nocedal and S. J. Wright. *Numerical optimization*. Springer, 2006.

[51] J. J. Burton and A. S. Nowick. *Diffusion in Solids: Recent Developments*. Academic Press, 1975.

[52] M. Born and R. Oppenheimer. “Zur Quantentheorie der Molekeln”. In: *Annalen der Physik* 389 (1927), pp. 457–484.

[53] P. Hohenberg and W. Kohn. “Inhomogeneous Electron Gas”. In: *Phys. Rev.* 136 (1964), B864–B871.

[54] W. Kohn and L. J. Sham. “Self-Consistent Equations Including Exchange and Correlation Effects”. In: *Phys. Rev.* 140 (1965), A1133–A1138.

[55] R. Parr and W. Yang. *Density-Functional Theory of Atoms and Molecules*. Oxford University Press, 1994.

[56] J. P. Perdew, K. Burke, and M. Ernzerhof. “Generalized gradient approximation made simple”. In: *Phys. Rev. Lett.* 77 (1996), pp. 3865–3868.

[57] P. Giannozzi, S. Baroni, N. Bonini, M. Calandra, R. Car, C. Cavazzoni, D. Ceresoli, G. L. Chiarotti, M. Cococcioni, I. Dabo, A. D. Corso, S. de Gironcoli, S. Fabris, G. Fratesi, R. Gebauer, U. Gerstmann, C. Gougoussis, A. Kokalj, M. Lazzeri, L. Martin-Samos, N. Marzari, F. Mauri, R. Mazzarello, S. Paolini, A. Pasquarello, L. Paulatto, C. Sbraccia, S. Scandolo, G. Sclauzero, A. P. Seitsonen, A. Smogunov, P. Umari, and R. M. Wentzcovitch. “QUANTUM ESPRESSO: a modular and open-source software project for quantum simulations of materials”. In: *J. Phys. Condens. Matter* 21 (2009), p. 395502.

[58] R. Ferrando. “Determining the equilibrium structures of nanoalloys by computational methods”. In: *Journal of Nanoparticle Research* 20 (2018), p. 179.

[59] B. Korte. “The Traveling Salesman Problem”. In: *Combinatorial Optimization: Theory and Algorithms*. Springer Berlin Heidelberg, 2008, pp. 527–562. ISBN: 978-3-540-71844-4.

[60] J. M. Dieterich and B. Hartke. “Error-Safe, Portable, and Efficient Evolutionary Algorithms Implementation with High Scalability”. In: *Journal of Chemical Theory and Computation* 12 (2016), pp. 5226–5233.

[61] Z. Li and H. A. Scheraga. “Monte-Carlo-minimization approach to the multiple-minima problem in protein folding”. In: *Proc. Natl. Acad. Sci. U.S.A.* 84 (1987), pp. 6611–6615.

[62] J. P. K. Doye and D. J. Wales. “Thermodynamics of Global Optimization”. In: *Phys. Rev. Lett.* 80 (1998), p. 1357.

[63] D. J. Wales. *Energy Landscapes*. Cambridge University Press, 2003.

[64] Y.-T. Lai, N. P. King, and T. O. Yeates. “Principles for designing ordered protein assemblies”. In: *Trends in cell biology* 22 (2012), pp. 653–661.

[65] T. O. Yeates, M. C. Thompson, and T. A. Bobik. “The protein shells of bacterial microcompartment organelles”. In: *Current opinion in structural biology* 21 (2011), pp. 223–231.

[66] B. De Nijs, S. Dussi, F. Smallenburg, J. D. Meeldijk, D. J. Groenendijk, L. Filion, A. Imhof, A. Van Blaaderen, and M. Dijkstra. “Entropy-driven formation of large icosahedral colloidal clusters by spherical confinement”. In: *Nature materials* 14 (2015), pp. 56–60.

[67] C. M. Dobson. “Protein folding and misfolding”. In: *Nature* 426 (2003), pp. 884–890.

[68] T. E. Creighton. “Protein folding”. In: *Biochemical journal* 270 (1990), p. 1.

[69] A. A. Pankova, T. G. Akhmetshina, V. A. Blatov, and D. M. Proserpio. “A collection of topological types of nanoclusters and its application to icosahedron-based intermetallics”. In: *Inorganic chemistry* 54 (2015), pp. 6616–6630.

[70] G. Bergman, J. L. Waugh, and L. Pauling. “The crystal structure of the metallic phase Mg32 (Al, Zn) 49”. In: *Acta Crystallographica* 10 (1957), pp. 254–259.

[71] D. Salunke, D. Caspar, and R. Garcea. “Polymorphism in the assembly of polyomavirus capsid protein VP1”. In: *Biophysical journal* 56 (1989), pp. 887–900.

[72] J. M. Montejano-Carrizales, J. L. Rodríguez-López, U. Pal, M. Miki-Yoshida, and M. José-Yacamán. “The completion of the platonic atomic polyhedra: The dodecahedron”. In: *Small* 2 (2006), pp. 351–355.

[73] T. P. Martin. “Shells of atoms”. In: *Phys. Rep.* 273 (1996), pp. 199–241.

[74] R. Ferrando et al. “Growth pathways of exotic Cu@ Au core@ shell structures: the key role of misfit strain”. In: *Nanoscale* 15 (2023), pp. 2384–2393.

[75] R. Ferrando et al. “Growth pathways of Cu shells on Au and AuCu seeds: interdiffusion, shape transformations, strained shells and patchy surfaces”. In: *Nanoscale Advances* 5 (2023), pp. 5838–5849.

[76] P. N. Pawlow. “Über die Abhängigkeit des Schmelzpunktes von der Oberflächenenergie eines festen Korpers”. In: *Z. Phys. Chem.* 65 (1909), pp. 1–35.

[77] W. Qi and M. Wang. “Size and shape dependent melting temperature of metallic nanoparticles”. In: *Materials chemistry and physics* 88 (2004), pp. 280–284.

[78] B. T. Sneed, A. P. Young, and C.-K. Tsung. “Building up strain in colloidal metal nanoparticle catalysts”. In: *Nanoscale* 7 (2015), pp. 12248–12265.

[79] J. Lee, S. M. Kim, and I. S. Lee. “Functionalization of hollow nanoparticles for nanoreactor applications”. In: *Nano Today* 9 (2014), pp. 631–667.

[80] J. H. Van Der Merwe. “Theoretical considerations in growing uniform epilayers”. In: *Interface Science* 1 (1993), pp. 77–86.

[81] T. Ala-Nissila, R. Ferrando, and S. C. Ying. “Collective and single particle diffusion on surfaces”. In: *Advances in Physics* 51 (2002), pp. 949–1078.

[82] G. Ehrlich and F. Hudda. “Atomic View of Surface Self-Diffusion: Tungsten on Tungsten”. In: *J. Chem. Phys* 44 (1966), pp. 1039–1049.

[83] E. Elkoraychy, K. Sbiaai, M. Mazroui, Y. Boughaleb, and R. Ferrando. “Numerical study of hetero-adsorption and diffusion on (100) and (110) surfaces of Cu, Ag and Au”. In: *Surface Science* 635 (2015), pp. 64–69.

[84] F. Montalenti and R. Ferrando. “Surface physics, low-dimensional systems, and related topics-Competing mechanisms in adatom diffusion on a channeled surface: Jumps versus metastable walks”. In: *Physical Review-Section B-Condensed Matter* 58 (1998), pp. 3617–3620.

[85] H. Bulou and C. Massobrio. “Mechanisms of exchange diffusion on fcc(111) transition metal surfaces”. In: *Phys. Rev. B* 72 (2005), p. 205427.

[86] D. Nelli, C. Roncaglia, R. Ferrando, Z. Kataya, Y. Garreau, A. Coati, C. Andreazza-Vignolle, and P. Andreazza. “Sudden collective atomic rearrangements trigger the growth of defect-free silver icosahedra”. In: *Nanoscale* 15 (2023), pp. 18891–18900.

[87] C. Roncaglia and R. Ferrando. “Machine Learning Assisted Clustering of Nanoparticle Structures”. In: *Journal of Chemical Information and Modeling* 63 (2023), pp. 459–473.

[88] R. Ferrando and G. Tréglia. “Tight-binding molecular dynamics study of diffusion on Au and Ag (111)”. In: *Surface science* 331 (1995), pp. 920–924.

[89] M. Rocca, T. Rahman, and L. Vattuone. *Springer handbook of surface science*. Springer Nature, 2021.

[90] G. Henkelman and H. Jónsson. “Improved tangent estimate in the nudged elastic band method for finding minimum energy paths and saddle points”. In: *J. Chem. Phys.* 113 (2000), p. 9978.

[91] Y. Xia, D. Nelli, R. Ferrando, J. Yuan, and Z. Y. Li. “Shape control of size-selected naked platinum nanocrystals”. In: *Nature Communications* 12 (2021), p. 3019.